

Effects of the Chemical Environment on the
Optical Properties of Semiconductor
Nanostructures

DISSERTATION

for the attainment of the degree

doctor rerum naturalium

(Dr. rer. nat.)

submitted by

ROMAN KUSTERER

Institut für Physikalische Chemie

Universität Hamburg

Hamburg

2024

Gutachter der Dissertation	Prof. Dr. Alf Mews Prof. Dr. Gabriel Bester
Gutachter:innen der Disputation	Prof. Dr. Alf Mews Prof. Dr. Dorota Koziej PD Dr. Tobias Vossmeier
Datum der Disputation	12.07.2024

Abstract

Semiconductor nanostructures have an enormous potential to revolutionize the technology for electronic and optoelectronic devices. In recent decades, the chemical synthesis of semiconductor nanostructures, which is essential for their use on a large scale, has developed rapidly. As a result, the implementation of nanostructures in applications, such as optoelectronic devices, is now increasingly becoming the focus of research. Part of this research is to understand and control the properties of nanostructures in their entirety to unlock their full potential. Critical to the successful use of nanostructures in devices is a comprehensive understanding of how their properties are affected by their environment.

This thesis examines the influence of the chemical environment on the optical properties, particularly the photoluminescence, of semiconductor nanostructures. This question is not only interesting for applications in sensor technology, but also represents a part of the necessary basic knowledge that is of central importance for the use of nanostructures in general. Two types of nanostructures, nanowires and quantum dots, were analyzed using confocal spectroscopy. Colloidal CdSe nanowires (or quantum wires) were prepared wet-chemically. To explore the influence of the chemical environment on the optical properties, measurements were performed in flow channels and gas-flow setups. In particular, the influence of oxygen on the photoluminescence and the Raman scattering was investigated. Both irreversible and reversible effects were observed and analyzed. Based on the findings, models were constructed to identify and adequately describe the effects. This led to the elucidation of photoinduced processes, such as the activation of photoluminescence and other changes in the emission and Raman spectra. The irreversible photoinduced activation of photoluminescence could be attributed to the formation of oxides and the concomitant elimination of surface defects in the form of unpassivated selenium. The reversible changes in the spectra, observed both in the form of additional blue-shifted emission and shifts in the Raman bands, could be attributed to the action of oxygen as a reversible electron acceptor.

In addition, the influence of oxygen on the photoluminescence properties of quantum dots was investigated. Here, the focus was on the reversible processes and in particular the blinking of the photoluminescence was investigated. A detailed analysis of the experimental data and the comparison with simulated data revealed multiple different effects of oxygen on the photoluminescence of quantum dots. The studies showed that oxygen acts as an electron acceptor, neutralizing particles and thus stabilizing the photoluminescence of quantum dots excited at high excitation powers. On the other hand, the effect of oxygen on the photoluminescence blinking of quantum dots with thin shells suggests that oxygen can also act as a centre for non-radiative recombination.

Kurzfassung

Halbleitende Nanostrukturen haben ein enormes Potential, die heutige Technik für elektronische und optoelektronische Bauteile zu revolutionieren. Die chemische Synthese von halbleitenden Nanostrukturen, welche essentiell für ihre Verwendung im großen Maßstab ist, erfuhr in den letzten Jahrzehnten eine rasante Entwicklung, sodass nun die Implementierung von Nanostrukturen in Anwendungen immer mehr in den Fokus der Forschung rückt. Ein Teil dieser Forschung ist, die Eigenschaften der Nanostrukturen in ihrer Gänze zu verstehen und zu kontrollieren. Maßgeblich für eine erfolgreiche Nutzung von Nanostrukturen ist ein umfassendes Verständnis des Zusammenspiels ihrer Eigenschaften mit ihrer Umgebung.

Das Ziel dieser Arbeit ist es den Einfluss der chemischen Umgebung auf die optischen Eigenschaften, insbesondere der Photolumineszenz halbleitender Nanostrukturen besser zu verstehen. Im Rahmen dieser Arbeit wurden zwei verschiedene Nanostrukturen, Nanodrähte und Quantenpunkte, mittels konfokaler Spektroskopie analysiert. Die kolloidalen CdSe Nanodrähte (oder auch Quantendrähte) wurden nasschemisch hergestellt. Um den Einfluss der chemischen Umgebung auf die optischen Eigenschaften zu erforschen wurden Messungen in Flusskanälen und Gasstromaufbauten durchgeführt. Insbesondere wurde der Einfluss von Sauerstoff auf die Photolumineszenz und die Ramanstreuung untersucht. Es wurden sowohl irreversible, als auch reversible Effekte beobachtet, analysiert und schließlich mit Modellen beschrieben. Dabei wurde die Natur photo-induzierter Prozesse, wie der Aktivierung der Photolumineszenz sowie weiteren Veränderungen der Emissions- und Ramanspektren entschlüsselt. Die irreversible photoinduzierte Aktivierung der Photolumineszenz konnte der Bildung von Oxiden und der damit einhergehenden Eliminierung von Oberflächendefekten in Form von unpassiviertem Selen zugeordnet werden. Die reversiblen Änderungen der Spektren, die sowohl in Form von zusätzlicher blauverschobener Emission, als auch Verschiebungen der Ramanbanden beobachtet wurden, konnten auf das Wirken von Sauerstoff als reversibler Elektronenakzeptor zurückgeführt werden.

Zusätzlich wurde der Einfluss von Sauerstoff auf die Photolumineszenz-Eigenschaften von Quantenpunkten untersucht. Hier stehen die reversiblen Vorgänge im Vordergrund. Durch eine ausführliche Analyse des Blinken der Photolumineszenz und dem Vergleich mit simulierten Daten konnten verschiedene Effekte von Sauerstoff auf die Photolumineszenz von Quantenpunkten identifiziert werden. Die Untersuchungen zeigten einerseits, dass Sauerstoff bei hohen Anregungsleistungen als Elektronenakzeptor Partikel neutralisiert und die Photolumineszenz somit stabilisiert. Der Einfluss von Sauerstoff auf das Blinken der Photolumineszenz bei Partikeln mit dünnen Schalen zeigt hingegen, dass Sauerstoff auch als Zentrum für nicht-strahlende Rekombination fungieren kann.

Contents

Abstract	I
Kurzfassung	III
List of Figures	VI
List of Tables	IX
List of Abbreviations	XI
1 Introduction	1
2 Theoretical Background	5
2.1 Semiconductor Nanostructures	5
2.1.1 Photoluminescence of Semiconductor Nanostructures	6
2.1.2 Modification of the Photoluminescence of Semiconductor Nanostructures	12
2.1.3 Raman scattering of Semiconductor Nanostructures	19
2.2 Semiconductor Nanowires	23
2.2.1 Solution-Liquid-Solid Synthesis	23
2.2.2 Photoluminescence Properties of Semiconductor Nanowires	25
2.3 CdSe/CdS Core-Shell QDs	29
2.3.1 Photoluminescence Blinking in QDs	30
2.3.2 Statistical Blinking Analysis	34
3 Methods	39
3.1 Confocal Microscopy	39
3.1.1 Focal Spot Size	39
3.2 IR spectroscopy	41
3.3 Electron Microscopy	42
3.3.1 Transmission Electron Microscopy	42
3.3.2 Scanning Electron Microscopy	43
3.3.3 Energy Dispersive X-ray Spectroscopy	43

4	Results and Discussion	45
4.1	CdSe Quantum Wires – Chemical Analysis	45
4.1.1	Composure and Surface	45
4.2	Optical Properties of CdSe QWs	54
4.2.1	Quantization in CdSe QWs	55
4.2.2	Photoluminescence of CdSe QWs	58
4.2.3	Photoluminescence Properties in Oxygen	59
4.2.4	Raman Properties of CdSe QWs	74
4.2.5	Effects of Dopants and Ligands on the Photoluminescence of CdSe QWs	78
4.3	CdSe/CdS Core-Shell Particles	83
4.3.1	Photoluminescence Properties of QD Thin Films	83
4.3.2	Photoluminescence Properties of Single Particles	88
4.3.3	Blinking Analysis	92
5	Summary	109
6	Experimental Procedures	111
6.1	Chemicals	111
6.2	Synthesis of CdSe QWs	112
6.3	Confocal Measurements	112
6.3.1	Setup	112
6.3.2	Sample Preparation	114
6.3.3	Classic Confocal Measurement	115
6.3.4	Measurements with Varying Environments	115
6.4	Other Characterization Methods	118
7	Bibliography	121
8	Appendix	133
8.1	Supporting Information	133
8.2	Hazard Information	135
8.3	Publications	138
8.4	Acknowledgments	139
8.5	Eidesstattliche Erklärung	141

List of Figures

2.1	Anisotropic nanostructures	6
2.2	Quantum size effect	7
2.3	Image charges	9
2.4	Charge-carrier recombination kinetics	10
2.5	Multiexcitons and quantum-confined Stark effect	11
2.6	Ligand classification	13
2.7	Interstitial and substitutive doping of CdSe with Ag	15
2.8	Raman scattering	20
2.9	Acoustic and optical phonons and exciton-phonon coupling	21
2.10	Resonant Raman spectra of CdSe and CdS QWs	22
2.11	Solution-liquid-solid synthesis of semiconductor nanowires and Bi-CdSe phase diagram	24
2.12	Wurtzite and zincblende crystal structure	25
2.13	CdSe/CdS bandalignment	30
2.14	PL intensity time-trace of a blinking QD	31
2.15	PL blinking mechanisms	32
2.16	Fluorescence lifetime-intensity distribution	34
2.17	Models for the power-law distribution of on- and off-states in PL blinking .	35
2.18	Autocorrelation	37
3.1	Confocal Microscopy	40
4.1	TEM and EDX data of CdSe QWs	45
4.2	FTIR spectra of CdSe QWs and potential ligands	47
4.3	FTIR spectra of CdSe QWs during purification	50
4.4	TGA-FTIR data of CdSe QWs and potential ligands	52
4.5	COMSOL simulations of uncharged and charged ground-state excitons in CdSe QWs	56
4.6	Emission spectrum and decay curve of CdSe QWs	59
4.7	Gas-flow setup and emission spectra of CdSe QWs in oxygen and nitrogen atmosphere	60

4.8	Evolution of PL intensity of CdSe QWs in oxygen and nitrogen atmospheres at different excitation powers	61
4.9	Transient evolution of PL intensity and emission wavelength at interrupted illumination and PL scans before and after photobrightening in oxygen . . .	63
4.10	PL scans of CdSe QWs with activated spots in oxygen and nitrogen atmosphere	64
4.11	Transient evolution of PL intensity and wavelength of CdSe QWs with changing atmospheres in the photodarkening period	65
4.12	Scheme of the proposed mechanism of oxygen-induced photobrightening and photodarkening of CdSe QWs	66
4.13	Laser reflection and SEM scan of a single CdSe NW and transient evolution of the PL in air	67
4.14	Evolution of the PL intensity and emission wavelength with changing gaseous surroundings during continuous illumination	69
4.15	Evolution of the PL at high excitation powers in oxygen and inert gas and excitation power-dependence of both emission peaks, as well as scheme for the preferred recombination state in oxygen and inert gas	71
4.16	Scheme of the mechanism underlying the reversible effects when switching between oxygen and inert gas	72
4.17	Evolution of the PL intensity and wavelength of CdSe NC thin films in oxygen and nitrogen atmosphere	73
4.18	Evolution of the Raman spectra of CdSe QWs under continuous illumination in air	75
4.19	Evolution of the Raman spectra of CdSe QWs under continuous illumination in changing atmospheres	76
4.20	Scheme of the flow-channel setup, as well as spectra and PL intensity time-trace of CdSe QWs in water and in MV (aq.)	79
4.21	Evolution of the spectra of CdSe QWs in AgNO ₃ (aq.) and in Cd(Ac) ₂ (aq.)	80
4.22	Evolution of the spectra of CdSe QWs in an atmosphere with gaseous <i>n</i> -propylamine.	82
4.23	PL of CdSe/CdS QDs in a thin film with changing gas atmospheres	84
4.24	PL of "big-shell" CdSe/CdS QDs in a thin film with changing gas atmospheres and varying excitation powers	85
4.25	PL of "small-shell" CdSe/CdS QDs in a thin film with changing gas atmospheres and varying excitation powers	86
4.26	PL intensity time-traces, histograms and decay curves of a single CdSe/CdS "big-shell" QD in oxygen and inert gas atmosphere	89

4.27	PL intensity time-traces, histograms and decay curves of a single CdSe/CdS "small-shell" QD in oxygen and inert gas atmosphere	93
4.28	FLIDs of a single "big-shell QD" in oxygen and nitrogen atmosphere at low and at high excitation power	94
4.29	FLIDs of a single "small-shell QD" in oxygen and nitrogen atmosphere at low and at high excitation power	96
4.30	Extract of the PL intensity time-trace of single "small-shell QD" in oxygen at low excitation power	97
4.31	Scheme of the dominant recombination patterns in "big- and small-shell QDs" in oxygen and nitrogen atmosphere	99
4.32	Distributions of the time periods for on- and off-states of a single "small-shell QD" at high and low excitation power in oxygen and in nitrogen atmosphere	101
4.33	Autocorrelation functions of single "small-shell" and "big-shell" CdSe/CdS QDs in oxygen and nitrogen atmosphere	102
4.34	Scheme for MC simulations	104
4.35	Simulated PL intensity time-traces and autocorrelation functions	106
6.1	Sketch of the setup of a confocal laser scanning microscope	113
6.2	Photographs of flow channels and a 3D printed template with a sketch showing the dimensions	116
6.3	Schemes of setups for measurements in different chemical environments	117
8.1	Spectra of CdSe QWs and extent of PL enhancement at different steps of purification	133
8.2	Evolution of spectra of CdSe QWs covered with PEG200	134

List of Tables

2.1	Effect of ligands on the PL of CdSe NCs (Literature)	14
4.1	ICP-MS and EDX data of CdSe QWs	46
4.2	Parameter for COMSOL simulations of CdSe QWs	55
4.3	Properties of CdSe/CdS QD samples	86
4.4	Average lifetimes of a single "big-shell QD" in oxygen and nitrogen at high and low excitation powers	91
4.5	Average lifetimes of a single "small-shell QD" in oxygen and nitrogen at high and at low excitation powers	92
6.1	List of chemicals	111
8.1	Safety and disposal instructions	135
8.1	Safety and disposal instructions	136
8.1	Safety and disposal instructions	137

List of Abbreviations

AFM	atomic force microscopy
APD	avalanche photodiode
ATR	attenuated total reflection
CB	conduction band
CCD	charge-coupled device
DOPA	di- <i>n</i> -octylphosphinic acid
DTG	derivative thermogravimetric
EDX	energy dispersive X-ray
EPC	exciton-phonon coupling
FLID	fluorescence lifetime-intensity distribution
FWHM	full width at half maximum
GHS	globally harmonized system
HDA	hexadecylamine
HDT	hexadecanethiol
HFS	high-frequency shoulder
ICP-MS	inductively coupled plasma mass spectrometry
FTIR	Fourier-transform infrared
LFS	low-frequency shoulder
LO	longitudinal optical
LUMO	lowest unoccupied molecular orbital
MC	Monte Carlo
ML	monolayer
MV	methyl viologen dichloride
NA	numerical aperture
NC	nanocrystal
NP	nanoparticle
NW	nanowire
PDMS	poly-(dimethylsiloxan)
PEG	polyethylene glycol
PL	photoluminescence

QCSE	quantum-confined Stark effect
QD	quantum dot
QW	quantum wire
QY	quantum yield
SEM	scanning electron microscopy
SLS	solution-liquid-solid
SO	surface optical
TCSPC	time-correlated single photon counting
TEM	transmission electron microscopy
TGA	thermogravimetric analysis
TO	transversal optical
TOP	tri- <i>n</i> -octylphosphine
TOPO	tri- <i>n</i> -octylphosphine oxide
TTTR	time-tagged time-resolved
VB	valence band
VLS	vapor-liquid-solid
WZ	wurtzite
XPS	X-ray photoelectron spectroscopy
ZB	zincblende

1 Introduction

In the 1980s, Alexei Ekimov presented the fabrication of small semiconductor crystals, with optical properties determined by the quantum size effect.¹ While those structures were embedded in a glass matrix, Louis Brus made similar observations for particles in solution and laid out important groundwork for the theory describing the experimental findings.^{2,3} A major breakthrough for the synthesis of semiconductor nanostructures, that allowed a reproducible fabrication of these particles in organic solvents, was presented by Moungi Bawendi in 1993.⁴ On October 4th 2023, Ekimov, Brus and Bawendi were rewarded with the Nobel Prize in Chemistry “for the discovery and synthesis of quantum dots”.⁵

The award of the Nobel Prize to the field of nanochemistry demonstrates the significance of this field to scientific and technological progress. The investigations carried out at that time provided the foundation for the development of a completely new branch of research. With the development of chemical methods, with which the physical properties of a material could be influenced and controlled in unprecedented ways, a field of research developed that represents a cross-section between physics and chemistry. Nanoscience deals with the properties of materials with dimensions in the nanometer range. For instance, as exemplified by quantum dots (QDs), the optical properties of a material can be adjusted by varying its size rather than changing the material itself. In fluorescent semiconductors, excited charge carriers, namely electrons and their counterparts, positively charged holes, can recombine and emit their energy in the form of a photon. QDs are semiconductor crystals that are so small that the space available for a charge carrier is confined by the particle. Therefore, particles of different sizes show different colors because the wavelength of the emitted light from a fluorescent particle correlates with the available space. QDs are used today in light-emitting diodes, for example in displays, but also as medium for solar-energy conversion, and for many more applications the development is promising.^{6,7}

In addition to QDs, other colloidal nanostructures have been developed. Elongated structures, such as nanorods⁸ and nanowires⁹ and also flat structures, such as nanosheets¹⁰ can be synthesized wet-chemically and give rise to various possible applications. The synthetic strategies for the production of those structures have only been developed during

the last decades, thus there are still challenges in controlling and understanding the respective nanocrystal (NC) properties.

This work focuses on the optical properties of semiconductor nanostructures, in particular the properties of nanowires (NWs) in the first part, and of QDs in the second part of this thesis. Colloidal NWs exhibit quite special properties due to their extraordinary structural conditions. In contrast to zero-dimensional QDs, NWs can be contacted by electrodes due to their lateral expansion in the micrometer regime. This enables the usage of NWs as building blocks in electronic and optoelectronic devices. Compared to the conventional top-down method of lithographic fabrication of nanoscale devices, the use of wet-chemically synthesized NWs provides a bottom-up approach, thus opening up new possibilities for device fabrication strategies.¹¹ The feature of one-dimensional charge-carrier transport makes NWs promising candidates for applications in field-effect transistors¹² or Li-ion batteries.¹³ While the micrometer-scale length of NWs makes them accessible to electrode contact, they still exhibit nanometer-scale widths and thus the characteristic high surface-to-volume ratio of low-dimensional nanostructures. This makes NWs suitable candidates for active materials in photodetectors¹⁴ and in devices for solar-energy conversion. NWs have been tested as active material in photo-voltaic cells¹⁵ and extensive research has been conducted to develop NW photochemical diodes.¹⁶

In order to use chemically grown NWs in devices of any kind, but especially as photodetectors or catalysts for photochemical reactions, it is crucial to understand the interaction of the material with its surroundings. The investigations presented in this thesis aim to provide a better understanding of the effect of the chemical environment on the material properties. The optical properties of nanostructures are investigated by confocal spectroscopy. To obtain real-time feedback while changing the chemical environment, measurements are performed in dedicated setups that allow the fast exchange of the surrounding medium while examining a single nanostructure. For the investigation of one-dimensional nanostructures, CdSe NWs are synthesized via the well established solution-liquid-solid (SLS) approach. The SLS synthesis yields colloidal structures with defined properties and the progress concerning the synthetic procedures that was achieved over the last decades enables good control over various features of the reaction products.⁹ The research in this work is focused on structures that exhibit small diameters and thus show quantum effects that are especially of importance when investigating the photoluminescence (PL) properties. For those structures, also referred to as quantum wires (QWs), the effects of some chosen chemical substances are examined, but the main part focuses on the impact of oxygen. As a substantial and ubiquitous component of our surroundings, oxygen represents a highly reactive species, that can affect material properties in various ways. By investigating the optical properties with responsive methods, such

as PL and Raman spectroscopy, photoinduced processes are explored and related to the influence of the reactive species surrounding the nanostructure. The insights gained by those investigations provide answers to questions with which research has been concerned for a long time. One of which is the clarification of the mechanism of photobrightening.¹⁷

In addition to the effects of oxygen on QWs, the effects on the PL properties of QDs are investigated. Since QDs resemble a system that was explored more extensively in the past, some studies of the interplay of oxygen with the PL already exist in the literature.¹⁸⁻²⁰ However, in some aspects the findings in the literature seem contradicting and the effect of oxygen on the PL of QDs was not unanimously clarified. For the optical properties of QDs, PL blinking is a process that is famous in research for almost 30 years now and is still in the focus of many investigations today.²¹⁻²³ By analyzing the data of single QDs that exhibit PL blinking in different atmospheres, and by comparing the experimental findings with data obtained by model simulations, new light is shed on the oxygen-particle interaction, as well as on the analysis of PL blinking in general.

In the following chapter, the theoretical background will be introduced. This includes general principles for semiconductor nanostructures, more specific aspects for the systems investigated in this work, as well as the state of the literature on the research subjects addressed in this thesis. After briefly describing the experimental methods, the results are presented. First, the results for CdSe QWs are outlined. After further reviewing the findings for the QDs the most important results of this thesis are summarized. The investigations presented in this thesis aim to improve the fundamental understanding of the optical properties of nanostructures, in order to pave the way for their implementation in applications and to advance scientific and technological progress.

2 Theoretical Background

This chapter provides an overview of the theoretical background to this work. First, some basic principles of semiconductor nanostructures will be introduced briefly. Subsequently, a few physical and chemical principles, which concern the experiments directly, will be discussed in more detail. These include the state of research about the optical properties of semiconductor NWs, some known effects of the chemical surroundings on the PL and Raman properties of semiconductor nanostructures, as well as recent insights in QD blinking.

2.1 Semiconductor Nanostructures

When considering an atom, the electrons exhibit discrete energy states. These states split when two atoms approach each other, leading to bonding and antibonding orbitals in molecules. In a crystal where many atoms are densely packed, the large number of interacting atoms leads to the formation of energy bands. The band formed by the orbitals of the valence electrons is called the valence band (VB), while the energetically higher band is called the conduction band (CB). In metals, the VB and CB always overlap, whereas in insulators and semiconductors, the VB and CB are separated by a band gap. If the band gap is less than 4 eV, the material is classified as a semiconductor, otherwise it is an electrical insulator.²⁴ The existence of a band gap in semiconductors, which allows the excitation of electrons from the occupied VB to the unoccupied CB, gives rise to special electrical and optical properties.

Materials with sizes from 1 nm up to 100 nm in at least one dimension are considered as nanomaterials.²⁵ For semiconductor nanostructures, spatial confinement of the material can determine its electrical properties. This allows for the classification of semiconductor nanostructures in two-dimensional quantum wells, one-dimensional quantum wires, and zero-dimensional quantum dots, as illustrated schematically in Figure 2.1. The degree of spatial confinement is defined according to the type of structure. As the degree of confinement increases, the degree of freedom of the charge carriers decreases. For each case, the resulting function for the density of states is depicted. A more detailed description can be found in ref. [26].

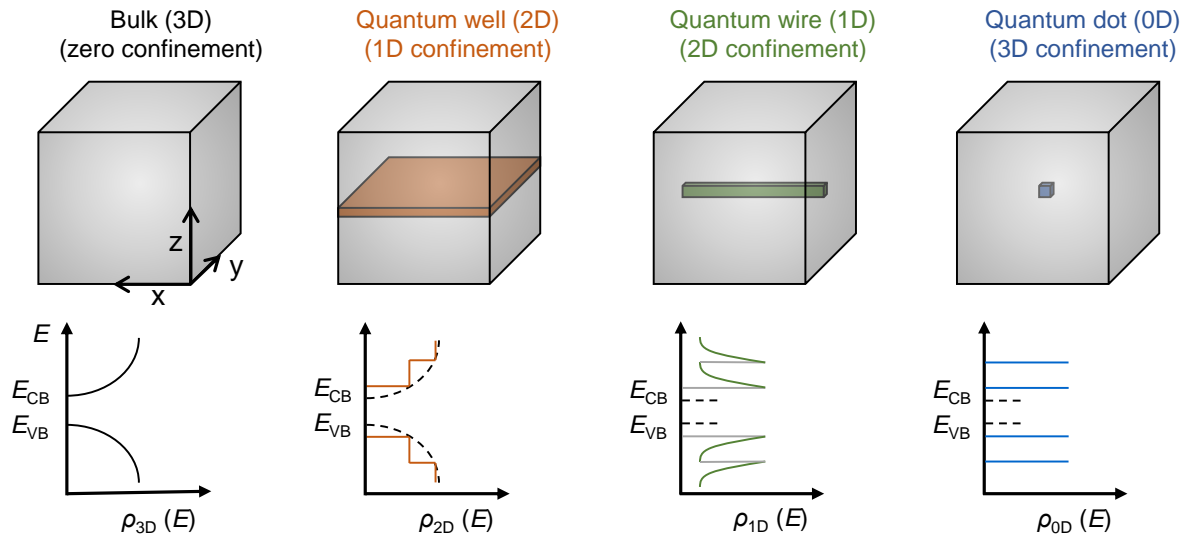


Figure 2.1: Schematic illustration of zero-, one- and two-dimensional nanostructures with their respective functions for the density of states. (Adapted from ref. [26]).

2.1.1 Photoluminescence of Semiconductor Nanostructures

Quantum Confinement

For semiconductor nanostructures, the size-dependence of the effective band gap is one of the most prominent effects, demonstrating the impact of the size in the nanoregime on the material properties. When exciting an electron from the VB to the CB, a positive charge, a hole, remains in the VB. Both charges experience attractive Coulomb forces and can form an exciton (electron-hole pair). The size of the exciton can be described analogously to the size of a hydrogen atom. The Bohr radius a_B for an exciton is

$$a_B = \frac{\hbar^2 \varepsilon}{q^2} \left(\frac{1}{m_e^*} + \frac{1}{m_h^*} \right), \quad (2.1)$$

with ε as dielectric constant of the material, \hbar as reduced Plank constant, q as electronic charge and m_e^* and m_h^* as the effective masses of electron and hole, respectively.²⁷

In the bulk material, the energy of the exciton is given by the material-dependent energy of the band gap $E_{g,\text{bulk}}$ and the Coulomb energy E_C . In the nanoregime, the size of the structure can confine the exciton if they lie in the same size range, leading to size-dependent energies of the excitons. This is schematically shown in Figure 2.2(a), along with the impact on the fluorescence properties of nanostructures, exemplarily shown by means of CdSe/ZnS core-shell QDs of different sizes in Figure 2.2(b). The energy of the effective bandgap E_{eff} of nanostructures with sizes in the confinement regime is therefore given by

$$E_{\text{eff}} = E_{g,\text{bulk}} + E_{\text{quant}} - E_C, \quad (2.2)$$

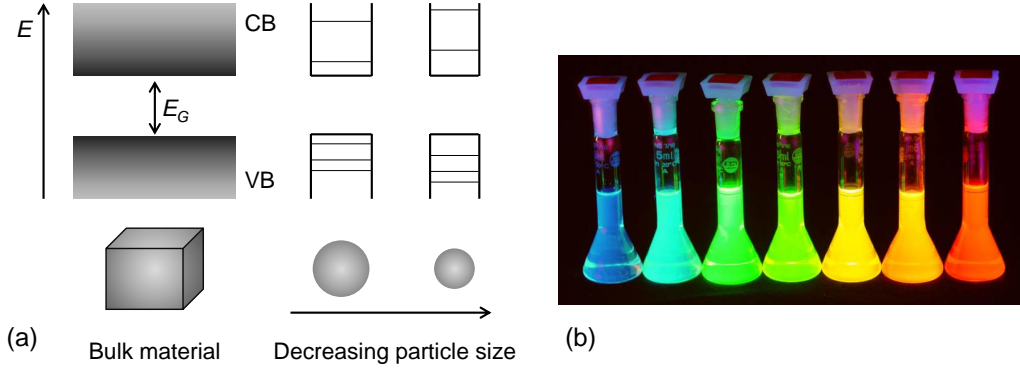


Figure 2.2: Effect of the nanostructure size on the PL properties. (a) Scheme showing the increasing energy of the effective band gap from a bulk semiconductor via nanoparticles to molecules. (b) Photograph of solutions of colloidal CdSe/ZnS core-shell QDs with increasing sizes from left to right, showing PL with emission wavelengths of a large part of the visible spectrum.²⁸

with E_{quant} as quantization energy due to confinement. To calculate the quantization energy in first approximation, the Schrödinger equation is solved for each charge carrier according to the particle-in-a-box model. In its general form, the stationary Schrödinger equation is given by

$$\hat{H}\Psi(\vec{r}) = E\Psi(\vec{r}), \quad (2.3)$$

with the Hamiltonian \hat{H} , the wavefunction Ψ , position vector \vec{r} and the eigenvalue E . The Hamiltonian can be written as

$$\hat{H} = -\frac{\hbar^2}{2m^*}\nabla^2 + \phi(\vec{r}), \quad (2.4)$$

with the Laplacian ∇^2 , the second derivative in three dimensions and $\phi(\vec{r})$ as potential. In the particle-in-a-box model, the potential is defined as zero inside and as infinite outside the box. For a one-dimensional box of the size L , the n th eigenvalue is

$$E_n = \frac{n^2\pi^2\hbar^2}{2m_e^*L^2}. \quad (2.5)$$

When considering an exciton, the Coulomb interaction can be included into the Hamiltonian, which then appears as

$$\hat{H} = -\frac{\hbar^2}{2m_e^*}\nabla^2 - \frac{\hbar^2}{2m_h^*}\nabla^2 - \frac{q^2}{\epsilon|\vec{r}_e - \vec{r}_h|} + \text{polarization terms}, \quad (2.6)$$

with the *polarisation terms*, which must be used to correctly describe the Coulomb interaction, as the charges in a NC are located in the immediate proximity of a crystalline surface. For a spherical particle with the radius R , an analytic approximation of the

effective energy of the lowest energy state was written by Brus as

$$E_{\text{eff}} \cong E_{\text{g,bulk}} + \frac{\hbar^2 \pi^2}{2R^2} \left(\frac{1}{m_{\text{e}}^*} + \frac{1}{m_{\text{h}}^*} \right) - \frac{1.8q^2}{\varepsilon R} + \text{smaller terms.} \quad (2.7)$$

This equation shows that the quantisation energy is a function of the square of the reciprocal radius R^{-2} and the Coulomb energy is a function of the reciprocal radius R^{-1} , illustrating the dominant effect of size quantisation on optical properties. The *smaller terms* in Equation 2.7 include contributions due to polarization, also depicted in Equation 2.6, which are not considered in this form.²⁹

Excitonic Energies in Nanostructures via Comsol

In this work, quantization and electrostatic effects in CdSe QWs were investigated by conducting calculations with the commercial software COMSOL. The use of COMSOL enables a precise definition of the nanostructure while structural parameters can be easily changed. The simulations were performed according to a procedure reported by Panfil et al.³⁰ At first, the Schrödinger equation is solved for electron and hole in a given structure. The Schrödinger equation for the electron is given by

$$\left(-\frac{\hbar^2}{2m_{\text{e}}^*(r)} \nabla^2 + V_{\text{CB}}(r) \right) \Psi_{\text{e}_n} = E_{\text{e}_n} \Psi_{\text{e}_n}, \quad (2.8)$$

with V_{CB} as conduction-band potential. For the hole, the analogue with the respective effective mass and the valence-band potential V_{VB} applies. Equation 2.8 gives the eigenvalue E_{e_n} , neglecting the Coulomb interactions.

In Equation 2.6, the Coulomb interaction is given by Coulomb's law.²⁹ In the approach via COMSOL, however, the Coulomb potential can be derived by solving the Poisson equation for each charge carrier of an exciton in the given structure. For an electron in the first state, the Poisson equation can be written as

$$-\nabla (\varepsilon \nabla \phi_{\text{e}}) = -q |\Psi_{\text{e}_1}|^2, \quad (2.9)$$

with ϕ_{e} as electric potential. The same accounts for the hole with the inverted sign for the charge q . In addition to the electric potential that a charge carrier experiences from the other charge carrier, the interaction of a charge carrier with its mirror charge due to the dielectric mismatch between NC and its surroundings can be considered (*smaller terms* in Equation 2.7). This is shown schematically in Figure 2.3. The self-polarization potential ϕ^{SP} is calculated by

$$\phi_{\text{e}}^{\text{SP}} = \phi_{\text{e}} - \phi_{\text{e}}^{\text{H}}, \quad (2.10)$$

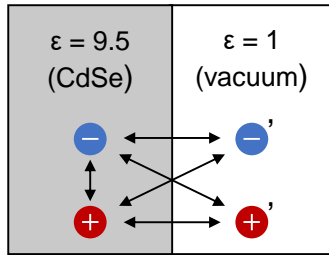


Figure 2.3: Schematic illustration for the electrostatic interactions of excitonic charge carriers at an interface with a dielectric mismatch, as for CdSe ($\varepsilon = 9.5$)³¹ and vacuum. In addition to the direct Coulomb interaction between electron and hole, the interaction with the respective image charges (') must also be considered. (Adapted from ref. [32]).

with ϕ_e^H as electric potential derived by solving the Poisson equation for the semiconductor structure and its surroundings without any dielectric mismatch (homogeneous permittivity of the semiconductor).³⁰ The electrostatic potentials ϕ^{SP} and ϕ_e^H , both derived by solving the Poisson equation, are then introduced in the Schrödinger equation. This is done in iterations and repeated until the eigenvalues E' converge. The Coulomb energy is then given by

$$E_C = \frac{|E'_e - E_e| + |E'_h - E_h|}{2}, \quad (2.11)$$

with the eigenvalues $E_{e,h}$ as determined in the first iteration and the converged eigenvalues $E'_{e,h}$ from the iterative solution of the Schrödinger and Poisson equations.

Photoluminescence Intensity

Besides the emission energy, the intensity of the PL is an important parameter characterizing semiconductor nanostructures. For all fluorophores, radiative recombination competes with non-radiative recombination, in which the energy of the relaxing charge carrier is for example released as thermal energy by emission of phonons.

Figure 2.4 schematically shows a model that was used to describe the PL decay kinetics of CdSe QWs, which will be used as representative model, since it is rather general in nature and applicable for various semiconductor NCs.³³ The simplest model consists of two states, a ground state and an excited state. The transition from excited to ground state can be radiative and nonradiative. Their ratio, as well as the number of excited charge carriers determines the emission intensity. When considering only radiative emission, the population of the excited state decays with

$$\left(\frac{dN}{dt} \right)_r = -k_r N, \quad (2.12)$$

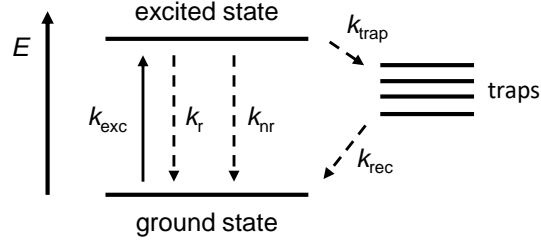


Figure 2.4: Schematic illustration of the model for charge-carrier recombination in semiconductors. In general, charge carrier transitions occur between the excited and the ground state with the rates k_{exc} , k_r and k_{nr} . An example for additional processes is the recombination through trap states (Adapted from ref. [33]).

where N is the population of the excited state at a time t and k_r is the radiative rate. The emissions of photons are random events, thus the decay of the excited state population proceeds exponentially and is given by

$$N(t) = N(0)e^{-k_r t} = N(0)e^{-t/\tau_r}, \quad (2.13)$$

with τ_r as radiative lifetime. In this case, the lifetime is defined as the time at which the number of relaxed charge carriers reached $N(\tau) = N(0)e^{-1}$. When adding the non-radiative processes the total rate equation for the transition of excited charge carriers is

$$\left(\frac{dN}{dt}\right)_{\text{total}} = -\frac{N}{\tau_r} - \frac{N}{\tau_{\text{nr}}} = -N\left(\frac{1}{\tau_r} + \frac{1}{\tau_{\text{nr}}}\right), \quad (2.14)$$

with the non-radiative lifetime τ_{nr} (or the non-radiative rate $k_{\text{nr}} = \frac{1}{\tau_{\text{nr}}}$). This yields

$$N(t) = N(0)e^{-t(1/\tau_r + 1/\tau_{\text{nr}})} = N(0)e^{-t/\tau} \quad (2.15)$$

for the population of the excited states with the lifetime τ , which is reciprocal to the total rate k .^{34,35}

In a PL measurement $N(t)$ is proportional to the measured intensity that changes when varying the transition rates. Non-radiative recombination is often linked to trapping of charge carriers in states that do not contribute to the usual VB and CB of the semiconductor, but lie energetically within the bandgap and can be located at the surface or outside the structure. For example, non-radiative recombination through trap states was implemented in the recombination model for CdSe QWs in Figure 2.4.³³ Mechanisms and processes related to non-radiative recombination are discussed in more detail when considering PL intermittency in Section 2.3.1.

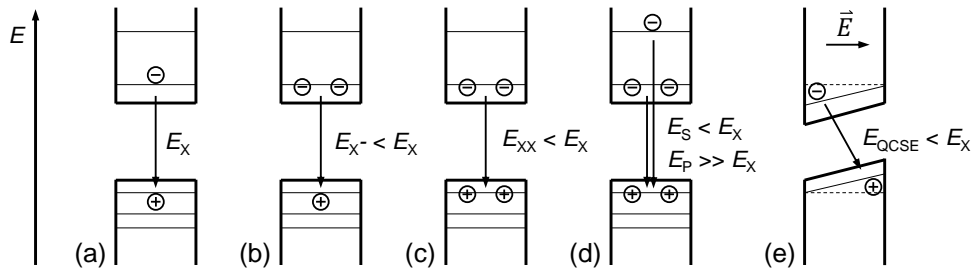


Figure 2.5: Scheme of the effects of multiexcitons and QCSE on the emission energy. (a) Neutral exciton with the emission energy E_X . (b) Exciton with an excess negative charge with E_{X^-} . (c) Neutral biexciton with E_{XX} . (d) Negatively charged biexciton with the energies E_S of the S-S transition and E_P of the P-P/P-S transition. (e) Neutral exciton in an electric field with the reduced energy E_{QCSE} .

Some more specific cases of charge-carrier recombination that can affect the PL of semiconductor nanostructures are briefly described in the following section.

Multiexcitons and Quantum Confined Stark Effect

At low excitation powers, single excitons are excited and recombine either radiatively or non-radiatively. The trapping of one of these charge carriers can lead to charged excitons if a subsequent exciton is generated before the trapped charge carrier got detrapped or recombined. In this way, positive or negative trions can be formed. Further, the excitation of multiexcitons is possible, especially at high excitation powers. If the particle remains neutral, neutral biexcitons are formed. The effects that the increased number of charge carriers can have on the recombination energy are complex. A small red shift in the emission wavelength is usually observed as an increase in Coulomb interactions.³⁶⁻⁴³ The same accounts for negatively charged exciton (trion) emission.^{20,44-46} For positive trions, the emission can be slightly blue-shifted.^{42,44} So far, only transitions at the lowest energetic levels, i.e. S-S transitions, have been considered. When charge carriers are added to a system in which the ground state is already filled, higher states can also be occupied. In this context, additional emission of P-P or P-S transitions of triexcitons and negatively charged biexcitons has been observed for CdSe NPs in the confinement regime, which is blue-shifted by up to 400 meV relative to the S-S emission.³⁶⁻⁴³ The schemes of the recombination of those states are illustrated in Figure 2.5(a-d).

As described above, additional charge carriers can affect the Coulomb interactions and thus the recombination energy of excitons, which can further be altered by electric fields. In the quantum-confined Stark effect (QCSE), the energy potentials in the nanostructure get altered due to an electric field and the emission energy experiences a red-shift, as

illustrated schematically in Figure 2.5(e). This was originally explored for QDs that were exposed to an external electrical field.⁴⁷ However, this effect can also be induced by the electric field of charge carriers of the nanostructure itself. For example, the observation of a reversible blue-shift of the emission wavelength of CdSe/ZnS QDs in water containing atmospheres was explained by the cancellation of a Stark red-shift that was induced by trapped charge carriers on the surface.⁴⁸

2.1.2 Modification of the Photoluminescence of Semiconductor Nanostructures

Much of this work is concerned with changes in the PL properties of semiconductor nanostructures over time. In this area of research, external parameters such as the chemical environment can have a significant impact. Understanding the influence of the chemical environment on the PL properties of semiconductor NCs is crucial for yielding control over the optical properties and for shaping them according to the requirements of potential applications. With respect to this topic, the surface of NCs naturally plays an important role. Before addressing modifications of the chemical surroundings on the PL, some principles for describing the surface of nanostructures will be introduced.

The Surface of Nanocrystals

At the surface of colloidal semiconductor NCs, the well-defined electronic structure of the crystal interior is disturbed by the presence of undercoordinated atoms and modified bonds, typically resulting in an increased amount of electronic states within the band gap. Those surface states can, for instance, induce PL quenching by trapping of photoexcited charge carriers. Considering the large surface-to-volume ratio of NCs, the electronic and chemical composition of the surface plays a major role for many NC properties. Passivation of electronic trap states as well as structural and chemical stability can be provided by organic molecules attached to the surface, forming a capping layer of ligands.^{49,50}

The ligands of colloidal NCs can be classified in the three different classes L-, X- and Z-type. Following the classification of coordination chemistry, the ligands are distinguished based on the number of electrons provided for the ligand-metal bond. The different kinds of surface passivation are schematically illustrated in Figure 2.6. L-type ligands bind datively to the surface by donation of a free electron pair. Phosphine oxides, phosphines and amines are prominent candidates for this class. X-type ligands provide one unpaired electron. According to the original covalent-bond classification, X-type ligands are formally regarded as neutral radicals that form a covalent bond with an unpaired electron on the NC surface. However, in colloidal nanochemistry, X-type ligands are usually presented by

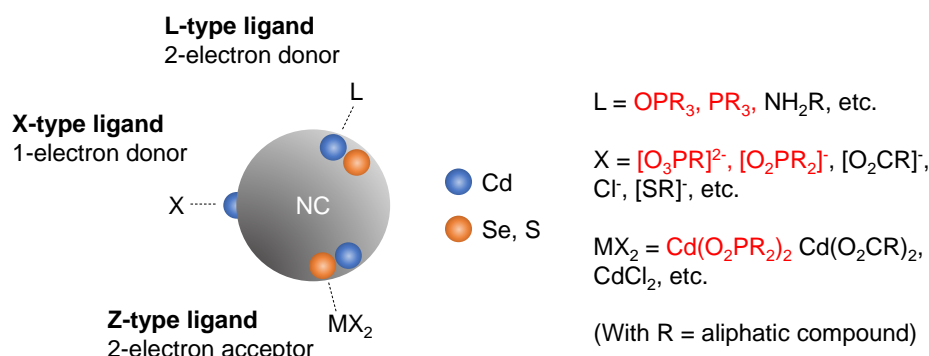


Figure 2.6: Schematic illustration of the different types of ligands for colloidal NCs. The substances used in this work for the synthesis of CdSe and CdS NWs are marked in red. (Adapted from ref. [49–51]).

anionic species that bind to a positively charged site on the NC surface, such as an excess metal ion. Phosphonic and phosphinic acids, carboxylic acids and halogenides represent common X-type ligands. For CdSe and CdS NCs, both L- and X-type ligands passivate undercoordinated Cd ions at the surface. In contrast, Z-type ligands are neutral electron acceptors that can bind to undercoordinated Se or S ions of the respective NCs. Common species are metal phosphonates, metal carbonates and metal halogenides.^{49–51}

After introducing the classification of ligands for colloidal NCs, the following section reviews how different ligands can affect their PL properties. In this area, the knowledge base is largest for spherical colloidal NPs. Therefore, the following section summarizes the main findings reported in the literature for NPs that relate to the experiments conducted in this thesis.

Effect of Ligands on the Photoluminescence

It is commonly agreed that an incomplete surface passivation results in surface trap states that lead to PL quenching due to trapping of charge carriers. Consequently, for wet-chemically synthesized NCs, the conditions during the synthesis itself are important for the optical properties, but also the purification can have an impact. For instance, it was found that purification by centrifugation of CdSe NCs leads to a decrease in the PL intensity with an increasing number of purification cycles.⁵² This observation confirms that stripping of ligands from the surface during the purification process increases the amount of surface trap states. Furthermore, a comprehensive study on the effects of various different substances as ligands on the PL intensity of CdSe NCs can be used as orientation for possible effects of ligands on the PL properties. The effect of some chosen substances

Table 2.1: Effect of the addition of different substances on the PL intensity I_{PL} of CdSe NCs. The change in PL intensity is given in %, relative to the initial emission at the respective emission wavelength of the intensity maximum.⁵²

Substance	HDA	HDT	TOPO	TOPSe	TOP	CdAc ₂	ZnAc ₂	AgNO ₃
ΔI_{PL} (%)	126	-66	34	-61	454	919	437	-100

on the PL intensity are summarized in Table 2.1. In this particular study it was found that L-type ligands such as hexadecylamine (HDA), tri-*n*-octylphosphine oxide (TOPO) and tri-*n*-octylphosphine (TOP) lead to an increased PL intensity, whereas the sulfurous substance hexadecanethiol (HDT), as X-type ligand, led to PL quenching. Remarkably, metal acetates such as CdAc₂ and ZnAc₂ resulted in the most significant increases of the PL intensity. Deprotonation of Se-H groups at the surface with subsequent coordination of Cd ions is discussed as possible mechanism for the enhancement of PL intensity. The addition of AgNO₃ caused complete PL quenching, which will be discussed in Section 2.1.2.

Another study which yielded important findings for the dependence of the PL properties of CdSe NCs on the particle surface was published by Jasieniak and Mulvaney.⁵³ By synthesizing CdSe particles with different surface stoichiometries and analyzing the effects of surfactants on the PL properties it was found that the addition of TOP would only lead to PL enhancement for NCs with Se-rich surfaces. Furthermore, photobrightening, a process which shall be discussed in more detail later, was only observed for Se-rich particles. These findings highlight that surface passivation and the effects on the PL properties are highly dependent on the respective sample, and universal assumptions and conclusions regarding the findings on a specific sample have to be considered with great care.

Effect of Cation Exchange and Doping

When adding an ionic species to a sample of colloidal NCs, the cations can diffuse into the crystal, where they can occupy interstitial positions and act as impurity dopants. Further, the new cations can take the places of the native cations that can be excluded from the crystal by a "kick-out reaction". If only a few atoms are added or replaced, the NC is doped with interstitial or substitutional impurities.⁵⁴ If the process continues, all native cations can be exchanged to form a completely new material. This method enables for example the fabrication of Ag₂Se NWs from CdSe NWs.⁵⁵ Naturally, the optical properties of the initial material can change drastically when performing a complete cation exchange. For CdSe or CdS NCs the exchange to Ag₂Se or Ag₂S leads to complete quenching of the

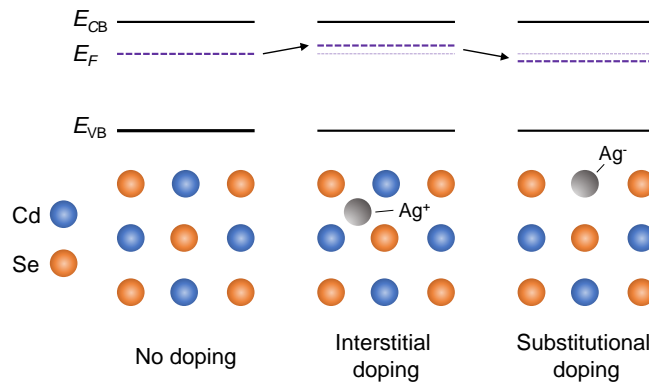


Figure 2.7: Schematic illustration of interstitial and substitutive doping of CdSe with Ag and the effect on the Fermi level. As interstitial impurity, Ag^+ acts as n-type dopant, while p-type doping results from substitutional doping with Ag^- (Adapted from ref. [54, 57]).

initial PL.⁵⁶ However, doping at very low concentrations can alter the electronic features of NCs in a way that even enhancement of the PL intensity can be observed.⁵⁷

For CdSe NCs it was found that the effects of doping with Ag ions are highly sensitive to the concentration of the dopants. For low doping concentrations of 2.7 atoms per 3.1-nm-diameter NCs significant PL enhancement was observed, which weakened towards higher concentrations. The change of the PL intensity was explained with concentration-dependent switching between interstitial and substitutional doping, both of which are schematically illustrated in Figure 2.7.

At low concentrations, Ag atoms would inject one valence electron in the CB, thus being present as Ag^+ ions inside the crystal, acting as n-type dopants and pushing the Fermi level towards the CB edge. At higher concentrations, Cd^{2+} ions are substituted by Ag. Due to the discrepancy of the number of valence electrons of Ag compared to Cd, the substitutional Ag accepts an excess electron. As Ag^- the impurity acts as p-type dopant, shifting the Fermi level to lower energies.^{54,57} The enhancement of the PL intensity at low Ag concentrations is argued to result from the positively charged interstitial impurities. The donor electrons, which could induce Auger quenching, are suspected to quickly get trapped outside the NC.⁵⁷ In theoretical considerations addressing the exciton fine structure of CdSe NCs it was found that the PL enhancement could result from breaking the symmetry of the NC by the dopant. An added positive charge would disturb the selection rules responsible for the dark state in undoped particles, thus leading to a decrease of the radiative lifetime.⁵⁸

Photoinduced Effects

After addressing the chemical modulations of nanostructures that affect their optical properties by changing their composition, the following section is about photoinduced effects that occur during illumination.

Photobrightening and Photodarkening Photoinduced processes in semiconductor nanomaterials that lead to changes in emission characteristics, such as PL intensity or emission wavelength, have been extensively reported over the last decades. This section provides an overview of the main findings related to this work.

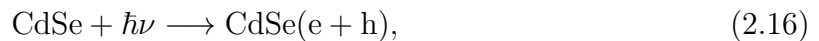
The term photobrightening is originally used to describe a reversible process in which the PL intensity gets enhanced during illumination, due to filling of trap states with charge carriers.⁵⁹ However, several processes can be responsible for a photoinduced enhancement of the emission intensity, and the term photobrightening was used in different contexts in the past. Trap states usually play a crucial role for the mechanisms of photobrightening. For example, it was proposed that photobrightening might be induced by a stabilization of charged trap carriers via ligand rearrangement at the surface, thus increasing the probability for thermalization of trapped charge carriers back to the excitonic ground state, instead of recombining non-radiatively.⁶⁰ Furthermore, changes in the potential barriers between bandedge and trap states due to trapped charge carriers are proposed to be responsible for PL enhancement,⁶¹ as well as electron migration through shallow trap sites in thin films of nanoparticles (NPs).⁶² In several reports, processes are described that lead to a reduction of trapping events by removal or blocking of trap sites. For example, it was proposed that ligands would rearrange and form new complexes at the crystal surface during irradiation, thus enhancing the passivation of surface trap states.⁶³ Detachment of ligands that would initially quench the PL intensity was also reported.^{64,65} Since a large amount of trap states are located at the surface, it is not surprising that correlations of PL enhancement with the environment of the structures was reported as well. In this context, PL enhancement due to adsorption of water molecules^{48,66,67} or amines in the gas phase⁶⁸ was reported. Usually, this kind of photoactivation is reversible and the weak adsorbents can be flushed away by changing the atmosphere. As a significant component of air, oxygen can also influence the PL of NCs. Several studies describe various observations of these interactions. Since this is particularly relevant for this thesis, those effects are described in detail in the next section.

Effects of Oxygen

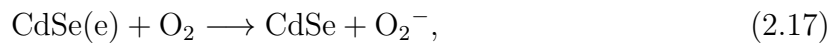
When discussing the effects of oxygen on the PL of semiconductor nanostructures, careful differentiation of several types of interaction is necessary. Both reversible and irreversible

PL modifications, as well as both enhancement and quenching of the PL intensity, have been attributed to interactions with oxygen.

Irreversible Effects The most prominent effect of oxygen on the PL of semiconductor NCs is the irreversible quenching of the PL intensity. Due to the high chemical reactivity of oxygen, photoinduced reactions with the NCs can result in decomposition of the structures, which leads to quenching of the PL intensity. Degradation of NCs via photooxidation was reported for NCs in solution,^{69,70} as well as for NCs on substrates, for both ensembles^{63,71–73} and single particles.^{74–76} The PL quenching due to photooxidation occurs due to destruction of the particle, which results in the formation of new trap states. This includes, but is not restricted to, the destruction of the organic ligands bound to the surface. The oxidation of the particle itself then leads to a shrinking of the particle size. Thus, a useful indicator for photooxidation is the blue-shift of the emission wavelength, due to increased confinement.^{63,72–76} For the mechanism of photooxidation of CdSe QDs, the following procedure was proposed by Hines et al.⁷⁰ Starting with the formation of an exciton



the electron gets scavenged by the oxygen molecule



leaving back the hole to form a reactive site



Then, anodic corrosion results in the formation of the respective oxides, according to



Especially for photooxidation reactions in solution, the formation of singlet oxygen might also play a crucial role. The excitation of oxygen to the singlet state, either by energy transfer after excitation of QDs,⁷⁷ or by direct excitation,⁷⁸ is proposed. The production of the singlet oxygen species in liquid media, such as in biological cells, offers the opportunity of the application of QDs in cancer therapy.⁷⁹

In addition to CdO and SeO₂, CdSeO₃ might be formed as oxidation product, since the formation of CdSeO₃ is thermodynamically the most favorable reaction.⁸⁰ While the exact composition of the oxidation products is not clear, the formation of SeO₂ was repeatedly

reported.^{63,70,80,81} A reduced Cd:Se ratio in oxidized samples suggests the detachment of SeO_2 from the particle over time.^{63,80,81}

Even though this photochemical oxidation is in most cases correlated with photodarkening of the PL, enhancement of the PL intensity due to photooxidation is reported as well. For particles in solution, photooxidation is suggested to act similar as photoetching, in which defects at the surface can be cured. Thus, PL enhancement was observed for CdSe, as well as CdS NCs dispersed in aqueous solutions. Similar as for the photodarkening studies, the observation of a blue-shift of the emission wavelength is usually used as an indicator for photocorrosion.^{82,83} Conversely, the absence of the observation of shrinking particles while observing PL enhancement with oxygen present in the solution lead to the conclusion that oxygen can also induce PL enhancement by passivation of surface states.⁸⁴ In a more specific case, PL enhancement due to photooxidation of ligands was reported as well. It was proposed that highly reactive oxygen species generated by photooxidation of the dopamine ligands passivate surface states of the NCs, resulting in PL enhancement.⁸⁵

In several investigations of thin films of particles, irreversible oxygen-induced PL enhancement was reported as well.^{73,76,86–89} In those studies it is discussed that the formation of an oxide layer of SeO_2 ⁸⁶ or CdO ⁸⁸ at the surface can result in PL enhancement. Thus, the oxide layer would act as passivating shell, similar to an inorganic layer in core-shell QDs.

The reports about both PL enhancement and PL quenching due to photochemical reactions with oxygen highlight the diversity of nanomaterials and that any photoinduced effect is highly dependent on the precondition of the material, as well as of the surroundings. The situation is found to be even more complex, as reversible effects of oxygen on the PL properties of semiconductor nanostructures were also reported and will be summarized in the following section.

Reversible Effects In addition to (photo-)chemical reactions of oxygen with semiconductor nanomaterials that can lead to irreversible PL enhancement and PL quenching, observations of reversible effects of oxygen on the PL have also been reported. Just as for the irreversible effects, both reversible PL quenching and reversible PL enhancement have been observed. A study of single CdSe NPs coated with ZnS by Koberling et al., in which the gaseous surrounding was changed between argon and oxygen, revealed a PL quenching effect by oxygen.¹⁸ The investigation of the blinking dynamics further revealed a shortening of the on-times in oxygen atmospheres. The authors proposed that oxygen molecules, adsorbed at the surface, act as additional trap sites. Similar observations were made for thin films of CdTe NCs, thus leading to the proposition of using CdTe NCs in oxygen sensors.⁹⁰

Contrasting to those findings are the reports of reversible PL enhancement of QDs. At first, bursts of the PL intensity of single CdSe/ZnS NCs in oxygen atmosphere were reported.¹⁹ This reversible process was attributed to an electron transfer to oxygen from non-emissive charged QDs, which then would be neutralized. The PL enhancement effect was correlated with the shell thickness and was suppressed with larger shells. An increase of the intensity enhancement in air, compared to in pure oxygen was explained by a broadening effect of the lowest unoccupied molecular orbital (LUMO) of the oxygen molecule in the presence of water, facilitating the electron transfer. Reversible PL enhancement effects were also studied for CdSe/CdS core-shell quantum wells⁹¹ and QDs.²⁰ In ensemble measurements a continuous more than two-fold enhancement of the PL intensity was observed in oxygen atmospheres. The dim state of the PL in the absence of oxygen was assigned in both studies to negative trion emission, which is formed via hole trapping. In the study of quantum wells, the PL enhancement was attributed to passivation of those hole traps by oxygen molecules.⁹¹ In the study of QDs, the PL enhancement was ascribed to electron scavenging by oxygen, thus neutralizing negatively charged particles. The study of the QDs by Hu et al. further revealed the presence of superoxide radicals $O_2^{\bullet-}$, which are formed when illuminating in solution.²⁰

The effects of oxygen on CdSe/CdS systems are subject of the second part of this thesis and further concepts that are relevant to this topic, such as PL blinking, are introduced and discussed in Section 2.3.1.

In order to conclude the general aspects of optical investigations of semiconductor nanostructures and before discussing the respective systems investigated in this work, Raman scattering is introduced below, which was investigated in addition to the PL properties.

2.1.3 Raman scattering of Semiconductor Nanostructures

The optical properties of a semiconductor material include not only the PL properties but also the light scattering properties. In general, it can be distinguished between elastic scattering processes (Rayleigh scattering) and inelastic scattering processes (Raman scattering). The latter separates further into Stokes and anti-Stokes scattering as either vibrations in the medium are generated or eliminated upon interaction with light. Moreover, resonant Raman scattering denotes the scattering processes if excitation occurs to a real electronic state, instead of to a virtual energy level. For resonant Raman processes the intensity of the scattered light is significantly enhanced. An overview of the scattering processes is illustrated in Figure 2.8(a–b).

Each material exhibits characteristic Raman-active vibrational modes, which allow for an optical characterization of the material in addition to fluorescence. These phonon

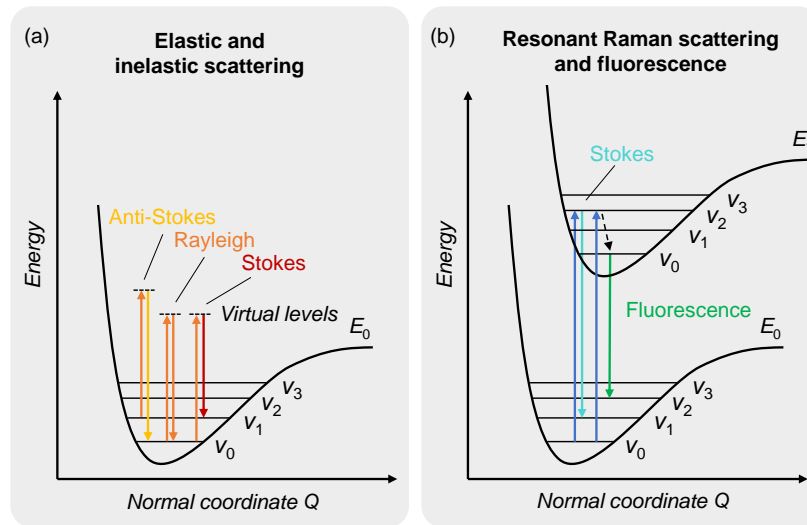


Figure 2.8: Raman scattering. (a) Energy diagram for scattering events via virtual energy levels. In an elastic scattering process (Rayleigh scattering) the vibrational state ν remains the same. Inelastic Raman scattering processes (anti-Stokes and Stokes scattering) occur with changing vibrational states. (b) Energy diagram of fluorescence and resonant Raman scattering via excitation in a higher electronic state (for the sake of clarity, only Stokes scattering is shown). (Adapted from ref. [92]).

modes are classified in acoustic and optical modes. Acoustic modes are vibrations in which neighboring atoms have a common direction of vibration, whereas in optical modes two neighboring atoms vibrate in opposite directions. For both types of phonon modes the atoms can be dislocated in either longitudinal and transversal direction, as illustrated in Figure 2.9(a). In resonant Raman scattering of semiconductor NCs, phonon modes can be amplified by exciton-phonon coupling (EPC). The two parts that usually contribute to this amplification are the deformation potential coupling and the Fröhlich coupling. The deformation potential addresses changes in the chemical bonds due to excitation, which lead to distortion of the atom equilibrium positions. The Fröhlich coupling describes the effect of spatially distanced charges of an exciton on the ions in the lattice. As illustrated in Figure 2.9, the lattice is distorted due to the interaction with the electric field of the exciton. The lattice relaxes upon recombination of the exciton and vibrations are induced.^{93,94}

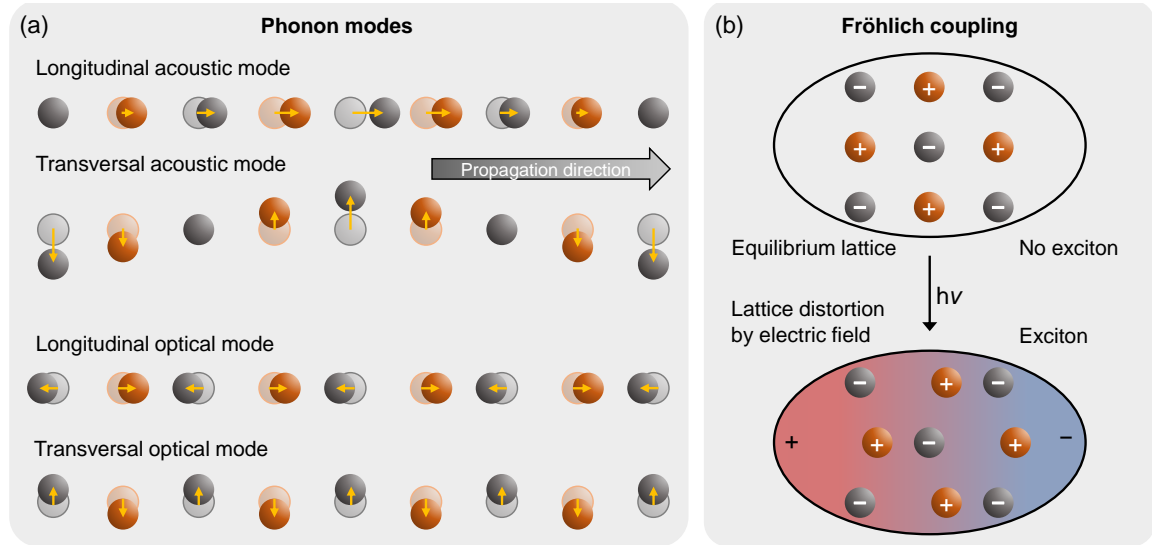


Figure 2.9: (a) Schematic illustration of phonon modes of compound semiconductor materials (Adapted from ref. [95]). (b) Schematic illustration of the Fröhlich interaction in EPC. Phonons are induced by relaxation of the lattice after exciton recombination (Adapted from ref. [93]).

Raman Spectra of II-VI Semiconductor Nanocrystals

In this work the Stokes scattering of CdSe QWs was investigated and therefore the findings concerning the research on the Raman modes of semiconductor nanostructures shall be briefly outlined in the following.

In a typical resonant Raman spectrum of II-VI semiconductor materials, the longitudinal optical (LO) phonon mode provides the most dominant peak. The LO phonon mode is typically accompanied by a low-frequency shoulder (LFS), also referred to as surface optical (SO) phonon mode.^{96–99} For very small NCs also a high-frequency shoulder (HFS) has been observed.¹⁰⁰ To observe transversal optical (TO) modes, the material needs to exhibit a sufficiently high deformation potential coupling. This is given for example in III-V compound materials. For CdTe NCs, the TO phonon mode was observed as well, but in polar materials such as CdSe and CdS, the Fröhlich coupling of exciton and LO phonon is dominant.^{101,102} In a resonant Raman spectrum, each mode appears together with several overtones, which each are shifted by $x \cdot \nu$ with $x \in \mathbb{N}$ in respect to the Raman shift ν of the fundamental mode. Spectra showing the fundamental Raman modes with the first overtone of CdSe and CdS QWs are shown exemplarily in Figure 2.10.

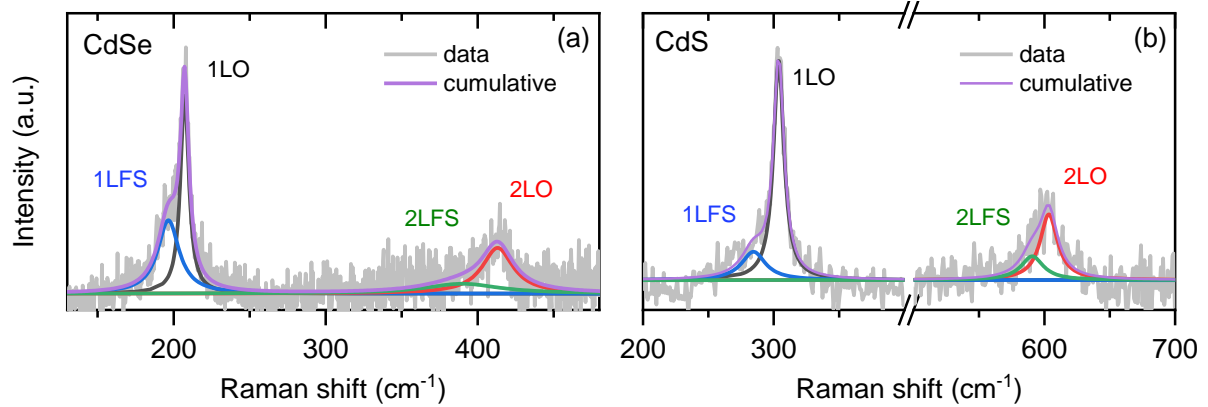


Figure 2.10: Resonant Raman spectra of CdSe and CdS QWs. (a) The fundamental Raman mode 1LO at 207 cm^{-1} with a LFS at 197 cm^{-1} and the first overtone 2LO at 413 cm^{-1} with a LFS at 390 cm^{-1} of CdSe ($\lambda_{Excitation} = 632.8\text{ nm}$). (b) The fundamental Raman mode 1LO at 304 cm^{-1} with a LFS at 285 cm^{-1} and the first overtone 2LO at 603 cm^{-1} with a LFS at 591 cm^{-1} of CdS ($\lambda_{Excitation} = 441.6\text{ nm}$).

LO phonon mode The LO phonon mode of semiconducting NCs can be affected by confinement of phonons. A shift to lower frequencies of the LO phonon mode with increasing confinement was observed for CdSe NCs. However, the effect is not very significant and even for very small NCs with radii of 3 nm, frequency shifts of only 4 cm^{-1} compared to the bulk value of 209 cm^{-1} were observed.¹⁰³ Apart from confinement, the LO phonon frequency can be affected by strain, while compressive strain would result in a shift to higher wavenumbers and tensile strain would result in a shift to lower wavenumbers. Shifts of the LO frequency peak of CdSe NCs after a ligand exchange were explained by this circumstance.¹⁰⁴

Fundamental to overtone ratio The intensity ratio of the fundamental LO phonon mode and the overtones are often correlated with the strength of EPC.¹⁰² However, a direct correlation between EPC strength and I_{2LO}/I_{1LO} for example is arguable as deviations in the resonant Raman processes can occur and because the mechanism of the origin of the overtones itself is still under debate.^{94,105}

SO phonon mode/ LFS For CdSe and CdS NCs a peak appears next to the LO signal, also visible in the spectra in Figure 2.10. This peak, often only observed as shoulder of the LO phonon peak, is broader and of lower intensity. The origin of the LFS is ambiguous and still under debate in the literature. For CdSe and CdS NCs, it is commonly assigned to the SO phonon mode.^{98,106} The frequency of the SO phonon mode is known to be dependent on the dielectric surroundings of the NC, as was shown for example for ZnS

NWs.¹⁰⁷ For ZnO submicron crystals a model was proposed in which changes in the surface charges affect the frequency of the SO phonon mode additionally.¹⁰⁸ Also for CdSe nanorods, changes in the LFS due to growing a ZnS shell were attributed to the change in the dielectric environment via application of the SO phonon model. However, theoretical considerations suggested that the LFS of CdSe NCs would result not from modes located solely at the surface, but from modes distributed throughout the whole NC. In contrast to that, the LO phonon mode would be dominated by motions in the NC interior. These considerations were supported by the observation of a dependence of the LFS on the excitation wavelength. Excitation in resonance to the $1S_e - 1S_{3/2}$ transition would preferentially amplify the modes located in the interior, while excitation in resonance to the $1P_e - 1P_{3/2}$ transition would enhance the lower frequency components near the surface.⁹⁹ Furthermore, for CdS NCs it was found that the surrounding dielectric medium does not have any impact on the frequency of the LFS or SO phonon mode, whereas a sensitivity to surface charges was determined.⁹⁸

Influence of charges Especially the influence of charges on both LO phonon mode and LFS are important for this work. For ZnO NCs, it was found that charging the particles with excess electrons alters both the intensity and the frequency of the Raman peaks. Upon charging, the frequencies of the LO phonon mode and the LFS were observed to shift to lower wavenumbers. This was explained via a screening effect of the ion-ion interaction due to the free charge carriers. Furthermore, a decrease in the ratio of fundamental to overtone peak intensity was observed upon charging, which may indicate a reduction in EPC strength.¹⁰⁵

2.2 Semiconductor Nanowires

The main part of this work is about wet-chemically synthesized CdSe NWs. The synthesis method, the SLS synthesis, is described in the following.

2.2.1 Solution-Liquid-Solid Synthesis

The SLS synthesis of NWs was derived from the vapor-liquid-solid (VLS) synthesis, which is similar in principle. In contrast to its predecessor, the SLS synthesis is performed in solution. For semiconductor NWs such as CdSe NWs, the usage of high boiling point solvents, as for example TOPO is widely spread. The liquid phase is given by the metal NPs that serve as catalysts. Using low melting point metals, such as Ga, In, Sn and Bi, allows for a synthesis at relatively low temperatures. Usually, the SLS synthesis is performed in a range of 200–350 °C. The NPs catalyze both the decomposition of

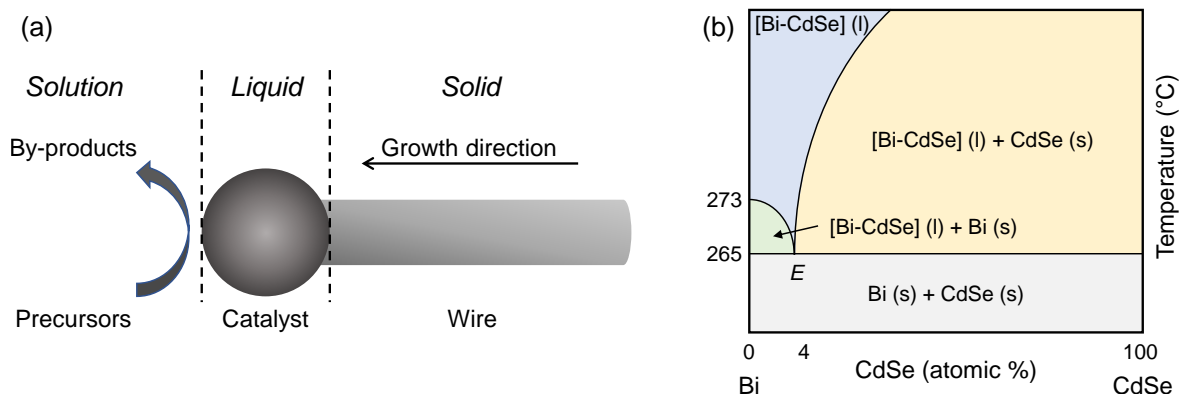


Figure 2.11: Solution-liquid-solid synthesis of semiconductor nanowires. (a) Schematic illustration of the growth mechanism (Adapted from ref. [9]). (b) Schematic illustration of the Bi-CdSe phase diagram. For a bulk system, the melting point of Bi is 273 °C and the eutectic point E of the alloy lies at 265 °C and 4% CdSe in Bi. At the reaction temperature (300 °C) for the CdSe wire synthesis employed in this work, CdSe dissolves in liquid Bi to form a liquid Bi-CdSe alloy. After reaching supersaturation, solid CdSe is formed (Adapted from ref. [110]).

the organo-metallic precursors and the growth of the solid wire. The reaction scheme is illustrated in Figure 2.11(a). The respective ions which form the semiconductor in the end, first dissolve in the metal NP. When supersaturation is achieved, a crystal facet is formed at the NP surface. Further growth of the crystal results in a one-dimensional structure, since the interface of the liquid NP with the newly formed solid semiconductor resembles the only active crystal-growth interface.⁹ Figure 2.11(b) shows the phase diagram of bulk Bi and CdSe. The synthesis of CdSe wires in this work was conducted above the melting point of Bi at 300 °C. For the Bi-particles used in this work, which exhibit an average radius of 3.7 nm, the melting point is even supposed to be reduced to 200–250 °C.¹⁰⁹ Supersaturation is reached at relatively low amounts of CdSe in the Bi-CdSe alloy, starting at 4 atomic% at 265 °C for a bulk system.¹¹⁰

This method enables the synthesis of wires with lengths of several micrometers and widths as small as 5 nm.⁹ The diameter of the wires can easily be controlled by the diameter of the catalyst particles.

Crystal Structure of CdSe Nanowires

The materials investigated in this work are CdSe and CdS, both of which are found in either hexagonal wurtzite (WZ) or cubic zincblende (ZB) crystal structure. The respective unit cells, the smallest unit from which the whole crystal can be yielded by translation,

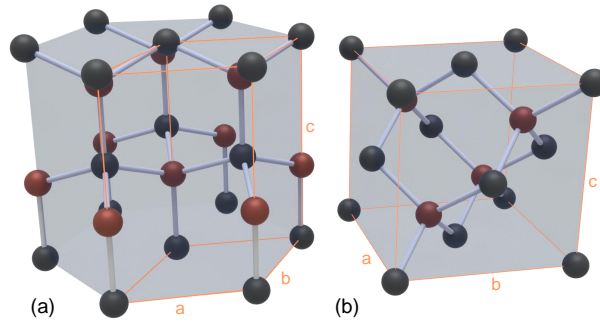


Figure 2.12: Schematic illustration of the (a) wurtzite and (b) zincblende crystal structure. The respective unit cells are marked by orange lines.

are schematically shown in Figure 2.12. In both crystals, the ions fill the tetrahedric gaps of the lattice of the respective counter-ion. In WZ, depicted in Figure 2.12(a), both ions form a hexagonal close-packed sub-lattice and the ion layers stack with the order ABABAB in the 001 direction. In ZB, depicted in Figure 2.12(b), each ion forms a cubic face-centered close-packed sub-lattice. The ion layers stack with a ABCABC pattern in 111 direction.

During the formation of Cd-chalcogenide NWs in the SLS synthesis, the crystal structure of the wire can switch. The nucleation energies for WZ and ZB nuclei are almost equal.¹¹¹ Thus, the resulting wires can obtain domains of each structure along the wire axis. Several synthesis parameters, such as temperature, Cd:chalcogenide ratio and organic ligands can affect the ratio of the fractions in the resulting wires.^{111–113} Wang and Buhro reported a synthesis of CdTe QWs exhibiting nearly phase pure WZ crystal structure.¹¹¹ They proposed that these wires are formed by a solution-solid-solid mechanism and that control over the synthesis can be gained by controlling the aggregate state of the Bi particles by varying the organic precursors. It was found that conversion of the Te-precursor and the reactivity of the Cd-precursor were decisive in this matter. According to their model, excess of Te dissolved in the Bi particle, which is mediated by the reactivity of the Cd-precursor, yields phase-pure WZ wires by growth out of solid particles. On the other hand, decomposition of the Te precursor that results in formation of CdTe clusters in the reaction mixture results in a stoichiometric amount of CdTe dissolved in the Bi particle, which then promotes growth of wires as a liquid particle.¹¹²

2.2.2 Photoluminescence Properties of Semiconductor Nanowires

The general concepts that are important for the optical properties of semiconductor nanostructures were already introduced. Since the main part of this thesis is concerned with

the optical properties of CdSe QWs, in particular the PL properties, a short summary of the current state of the literature is given in this section.

Confinement in CdSe Nanowires

Increasing control of the SLS synthesis of semiconductor NWs over the last two decades has allowed the fabrication of wires with controlled optical properties, such as defined diameters in the quantum confinement regime.^{114,115} The effect of the quantum confinement on the PL emission energy of single CdSe QWs was systematically investigated by Myalitsin et al.¹¹⁶ By performing a correlation study, employing transmission electron microscopy (TEM) and PL spectroscopy of different sized wires, it was found that the size effect on the PL emission was in good agreement with theoretical values obtained by calculations within the effective mass approximation for one-dimensional structures. Further, in a study by Giblin et al., the effects of quantum confinement on the absorption features were demonstrated.¹¹⁷ By measuring the extinction spectra of single CdSe QWs, distinct features of the absorption of higher energy levels that were obscured in ensemble measurements were yielded. Thus, in addition to the size quantization effects for charge carriers in their ground state, diameter dependent information of the energy separation of first excited and higher excited states was determined. Apart from the effects of quantum confinement on the PL properties, another process that is relevant for all fluorescent nanostructures is PL intermittency. The most important findings about PL intermittency of semiconductor NWs will be summarized in the following section.

PL Intermittency in Nanowires

PL intermittency, also known as blinking, is a process that can be observed for all kinds of fluorescent emitters. In this work, blinking is primarily investigated for QDs. Therefore, blinking mechanisms and dynamics are introduced in Section 2.3.1. However, since the elucidation of blinking mechanisms and charge carrier recombination dynamics has played an important role in semiconductor NW research, the most important findings for NWs will be summarized here shortly.

PL intermittency is most prominently known for QDs, however, it is also observed for semiconductor NWs. In contrast to QD blinking, the PL of the wire does not switch to an absolute off-state but the intensity switches randomly between bright and dim states. PL intensity fluctuations of up to 80% have been observed.¹¹⁸ Multiple possible origins of the PL blinking in NWs have been discussed. It was suggested, for example, that parts in the wire in which the crystal structure changes between WZ and ZB provide sites for blinking. Alternating WZ and ZB segments yield a type-II like band alignment, at which excited charge carriers can get spatially separated. This might induce Auger blinking.¹¹⁸

Nonradiative Auger recombination can also be induced by the presence of charged sites, for example at the wire surface. In low-temperature experiments of CdSe QWs, additional emission peaks were observed red-shifted to the near-band-edge emission.¹¹⁹ Supported by numerical simulations, the red-shifted peaks were assigned to complexes of excitons that are bound to charged donor and acceptor sites. In the studies described so far, the blinking behavior was studied by confocal spectroscopy, thus the information is gained from one single spot in each measurement. Apart from localized PL intermittency, blinking of whole NWs was also reported and was explained by filling and emptying of surface traps with photo-excited charge carriers.^{33,120} The authors argue that once the traps are filled, excitons are formed that move along the wire axis and recombine radiatively unaffected by trap sites, thus leading to an increased PL intensity of the whole particle. But this was only observed in a small fraction (<2%) of wires and it was proposed that only "ideal" wires in which excitons are able to move along the wire axis without being hindered by irregularities in the exciton potential.¹²⁰ Reports about localized excitonic emission and the effect of charges on the PL will be discussed in more detail in the next section.

Bound Excitons and Free Charge Carriers

Charge transport and the presence of bound excitons or free charge carriers were extensively investigated in the past. The question whether the properties of CdSe NWs are dominated by bound excitons or separate charge carriers arises because in 1D-structures, charge carriers are in principle able to move along the wire axis, while the degree of confinement is larger than in 2D-structures. In 2D-structures, excitons do not tend to be bound at room temperature (except for ultrathin nanoplatelets) due to the small exciton binding energies with confinement in only one dimension.^{121,122} The investigations about the quantum confinement in CdSe NWs discussed earlier, already showed features of bound excitons. The correlation of spectroscopic data, obtained by extinction and PL emission spectroscopy of different sized NWs, with simulated data highlighted the necessity of implementing Coulomb interactions in the calculations, indicating the existence of bound excitons.^{116,117} Yet, observations of mobile charges were also reported. For example, PL variations were observed in 10 nm thick NWs when applying an external electric field.¹²³ Furthermore, diffusion of photoexcited charge carriers has also been observed without an electric field.¹²⁴ By combining electrostatic force microscopy and PL spectroscopy, it was shown that photoexcited electrons diffuse through the wire, leaving behind a positively charged excitation spot. This study showed that charge carriers of excitons in CdSe NWs can also be separated. The diameter of the wire is likely a crucial factor for this observation, as it is inversely proportional to the Coulomb interactions. For the wire investigated in this study, the diameter of 12 nm results in relatively low binding energies of 20 –

30 meV. Charge separation was further demonstrated in CdSe/CdTe hetero-nanowires, in which negative charges would accumulate in the CdSe part and positive charges would accumulate in the CdTe part.¹²⁵ In regard to the question of free charge carriers that can be mobilized in electric fields, the group of Loomis also contributed a study.¹²¹ In that study, effects of the electric field on the PL intensity of the wires were only observed in ensemble samples in which the wires were embedded in a matrix of residues from the synthesis. The authors suspect charge-carrier injection by $\text{Bi}_3^+(\text{TOP})_n(\text{TOPO})_m$ salts into the wire. From the absence of PL intensity steering in diluted samples, the authors conclude the presence of bound 1D-excitons. The wires used in that study obtained diameters of 7 nm. The results concerning the PL of the wires of some of the studies discussed above are summarized in the following section.

PL Modulation by Charges and Electric Fields

As mentioned above, the effects of charges and electrical fields on the PL of wires were investigated. PL intensity modulation by applying an electrical field was first reported by the Kuno group, who observed increased PL intensity at the end of the wire that pointed in the direction of the positive electrode.¹²³ The authors concluded that mobile negative charge carriers would be transported along the wire axis. The observations in the study by Loomis and co-workers were similar, however, they only observed this in ensemble experiments and attributed the presence of mobile charges to the surrounding matrix.¹²¹ The effects of charges on the PL of wires was also investigated by Schäfer et al. in a study in which the wire is charged through a biased atomic force microscopy (AFM) tip.¹²⁶ The examined wires were neutral at first and showed PL quenching upon injection of positive charges and PL enhancement upon injection of small amounts of negative charges. To explain the observations, it was assumed that the wires exhibit electron traps. Thus, injecting small amounts of electrons fills these traps, inhibiting trapping of photo-excited electrons. Injecting positive charges quenches the PL via the Auger mechanism. Furthermore, photobrightening was observed, but no changes in the state of charge due to the PL enhancement were determined.

Surface of SLS-grown Nanowires

In general, the PL quantum yield (QY) of the NWs in all the studies discussed so far is quite low at $<1\%$ compared to other nanomaterials, such as QDs that exhibit QYs of up to 85%.¹²⁷ Surface traps are assumed to play a crucial role for the high amount of non-radiative recombination in NWs.⁹ One example demonstrating the importance of surface passivation for QWs was reported by Liu et al.¹²⁸ By simply adding ethanethiol to CdTe QWs, heating and re-dispersing in TOP, an increase of the QY from $<1\%$ to

25% was observed. The effect was attributed to the formation of a CdS shell and thus the formation of a type-I core-shell structure. Apart from further reports on growing inorganic shells on NWs, however,^{129–132} effects of surfactants on the PL properties of NWs and even investigations on the composition of the surface of the native SLS-grown NWs itself are rare, and those domains are comparatively poorly understood.

Before going into the results of the investigations on CdSe QWs, some principles will be discussed that are important for the second part of this thesis: the PL properties of QDs.

2.3 CdSe/CdS Core-Shell QDs

After the evolution of synthetic methods to grow semiconducting NPs in solution, efforts were made to alter and control their PL properties. Apart from varying the particle size, creating heterostructured QDs by growing inorganic shells proved to be a useful method yielding large effects on the optical properties of QDs.^{133–136} By encapsulating, for example, CdSe NCs with a material exhibiting a larger bandgap, such as ZnS, surface states are passivated and the charge carriers are confined to the core leading to an increase of the QY.¹³⁵ Such a core-shell bandalignment is called type I bandalignment. An adjoined offset in both VB and CB to higher or lower energies of two adjacent materials, such as for a CdTe/CdSe system, results in charge carrier separation and is referred to as type II bandalignment.¹³⁷ Encapsulation of CdSe NPs with a CdS shell can yield an interesting intermediate case. Nominally the bandedges of the bulk materials would result in a type I core-shell structure, as illustrated in Figure 2.13(a), with both electron and hole confined to the core. Yet, the offset in the CB is small enough that the electron can be delocalized over the shell, while the hole remains in the core, as illustrated in Figure 2.13(b). This bandalignment is referred to as quasi-type II.¹³⁸ Several factors, such as the size of core and shell, as well as the condition of the core-shell interface (gradual or sharp) determine to what extent the electron is delocalized. For very small CdSe cores it was reported that the increased confinement shifts the energy level of the electron to states higher than the offset of the bands.^{138–140} But also strain at the core-shell interface alters the band offset, thus lowering the electron delocalization for smaller cores.¹⁴¹ Another aspect that affects the band alignment is the nature of the core-shell interface itself, as a gradual junction of the different anions with an alloyed intermediate section also leads to larger delocalization of the charge carriers over the particle.¹⁴²

In general, growth of a CdS shell on CdSe cores results in passivation of surface trap states, thus enhancing the QY. Carrier delocalization leads to prolonged lifetimes and the emission energy shifts to lower energies.¹³⁶ The synthetic strategies continuously developed

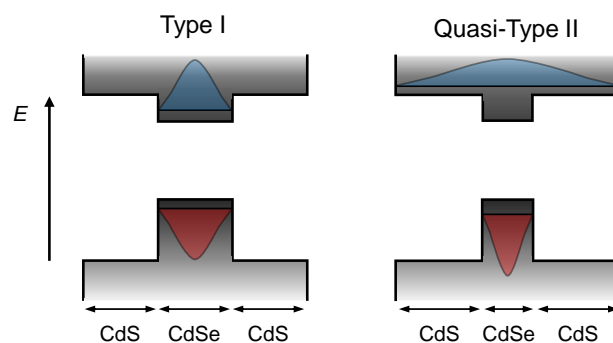


Figure 2.13: Bandalignment in CdSe/CdS core-shell QDs. (a) Nominally CdSe/CdS core-shell structures exhibit a type I band alignment. (b) The electron can be delocalized due to the comparatively small offset between core and shell region of the CB (0–0.3 eV).¹⁴¹ Factors like confinement,^{138–140} strain at the core-shell interface¹⁴¹ or alloyed and gradient interfaces¹⁴² determine the extent of the quasi-type II character of the bandalignment.

during the last two decades, yielding highly emissive CdSe/CdS core-shell QDs. The QDs investigated in this work are synthesized based on a synthesis by Chen et al., who reported the fabrication of QDs with large CdS shells, so called "giant"-shell QDs.¹⁴³ With this method, PL blinking was largely reduced. The origin and mechanisms of PL blinking will be explained in the following section.

2.3.1 Photoluminescence Blinking in QDs

In the course of the advancement of fluorescence spectroscopy of single emitters, a number of phenomena were discovered which could not be resolved in ensemble measurements, such as photon antibunching¹⁴⁴ and fluorescence intermittency.²¹ In general, fluorescence intermittency, also referred to as fluorescence blinking, describes spontaneous changes in the fluorescence intensity of a fluorophore under continuous excitation. An exemplary data set of a time trace of the PL intensity of a QD exhibiting blinking is shown in Figure 2.14(a). The PL intensity switches randomly between the on-state, in which the intensity is at approximately 20 counts/50 ms and the off-state, in which the intensity is on the level of the background signal. Some time periods with intensities in between these two states are also observed. The occurrence of the two states is also clearly visible in the histogram in Figure 2.14(b).

A lot of research, especially concerning PL blinking of QDs, has been addressing this phenomenon over the last decades, proposing several mechanisms. The three most general and most important mechanisms will be introduced for this work. Figure 2.15(a) shows the scheme of the processes in a NP in the on-state, in which excited charge carriers

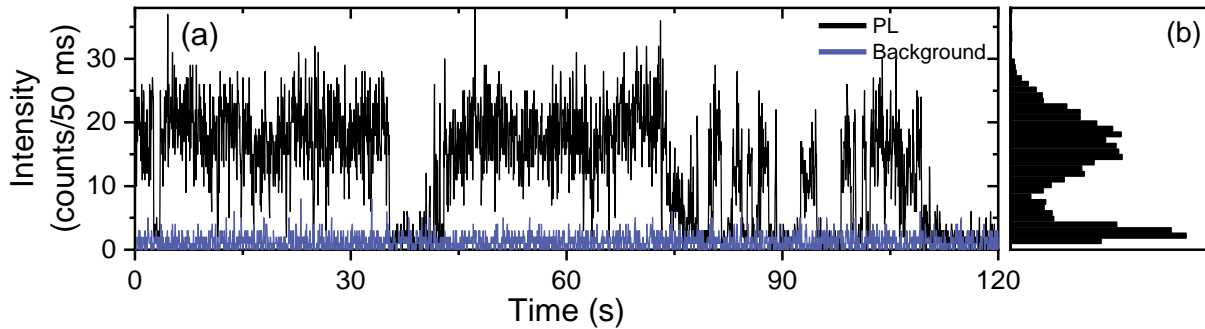


Figure 2.14: Exemplary PL data of a blinking QD. (a) PL time-trace with discrete on- and off-states, which last several seconds, as well as short intensity fluctuations. (b) Histogram of the PL time-trace, highlighting the occurrence of an on- and off-state, along with some intermediate states.

quickly relax to the bandedge via generation of phonons and recombine radiatively. In the off-state, recombination is dominated by non-radiative recombination of charge carriers, for which the different underlying mechanisms are described in the following. The most established blinking mechanism is Auger blinking, also referred to as A-type blinking, depicted in Figure 2.15(b). Here, one charge carrier of an exciton is trapped at the surface of the particle or its surroundings. This can either occur by direct transfer via tunneling or thermo-ejection of a charge carrier to a trap state, or by Auger autoionization. The remaining charge in the particle inhibits efficient radiative recombination by absorbing the recombination energy of subsequently excited excitons. The particle remains in a non-emitting or weakly emitting state, called off-state, until the trapped charge carrier neutralizes the charged particle again, thus promoting the fluorescence back to the neutral emitting state, called on-state.¹⁴⁵ However, not all observations could be explained by the charging model and two additional mechanisms, shown in Figure 2.15(c), were proposed. One of them is based on the interception of hot charge carriers and is also referred to as B-type blinking. Thereby, hot charge carriers get trapped before or during the relaxation process (during which phonons are generated) before reaching the bandedge and recombine non-radiatively, leading to the off-state.¹⁴⁶ A similar mechanism is the bandedge-carrier blinking, sometimes referred to as C-type blinking.¹⁴⁷ In this mechanism, the off-state is also generated by non-radiative recombination of charge carriers via trap states. However, instead of hot charge carriers, charge carriers that already relaxed to the bandedge are trapped.¹⁴⁸ For both B- and C-type blinking, non-radiative recombination centers are activated and deactivated, resulting in blinking of neutral particles, opposed to Auger blinking of charged particles. Further, hot-carrier blinking and bandedge-carrier blinking distinguish themselves in the competition of radiative and non-radiative recombination. For hot-carrier blinking, some charge carriers are intercepted in the cooling process and

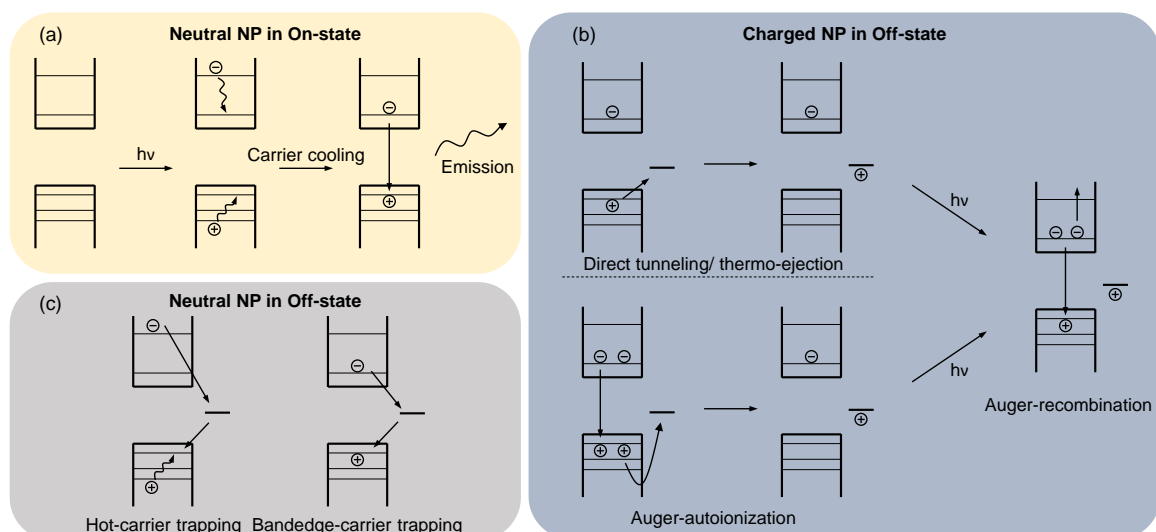


Figure 2.15: Schematic representation of blinking mechanisms in QDs. (a) Excited charge carriers relax via emission of phonons to the band edge and recombine radiatively. (b) Charging of the NP by direct tunnelling or thermo-ejection of a charge carrier to a trap state, or by Auger autoionization. The trion, resulting upon further illumination, undergoes non-radiative Auger recombination. (c) Off-state in a neutral NP while either hot charge carriers or charge carriers at the bandedge recombine non-radiatively via trap states.

recombine non-radiatively without affecting the PL emission, while other charge carriers still contribute to the radiative recombination without being affected by the trapping. Therefore, the PL intensity switches between on- and off-state, while the PL lifetime stays constant. For bandedge-carrier blinking, trapping occurs after cooling of the charge carriers to the bandedge. The rates of trapping and subsequent non-radiative recombination lie in the same range as the radiative recombination. Therefore, PL intensity and PL lifetime are linearly correlated.¹⁴⁸

So far, blinking has been described as the switching between on-state, in which the QD is in a neutral light-emitting state, and the off-state, in which the QD is completely dark for a certain period of time. However, intermediate states, so-called grey states, have also been observed. If the rates of non-radiative and radiative recombination are in the same order of magnitude, the photon emission is not completely suppressed anymore. Typically, this is observed for CdSe/CdS QDs with big shells.¹⁴⁹ In contrast to type-I QDs with large band offsets such as CdSe-core/ZnS-shell QDs, electrons in CdSe-core/CdS-shell QDs are delocalized over a large area due to the small energy offset in the conduction band. This reduces the efficiency of Auger processes in trions to such an extent that the radiative recombination competes with the non-radiative recombination, resulting in a grey state.

Principally, multiple blinking processes can be present in one QD. However, the QD properties determine the dominant recombination pattern. A-type blinking was observed

in a wide range of different QD architectures, but most prominently in CdSe/ZnS type-I QDs.¹⁵⁰ It requires the presence of deep traps, in which charge carriers obtain long retention times in order to allow for excitation of a subsequent exciton, before detrapping occurs. For all types of blinking, trap states at the surface are considered. However, for B-type blinking it was proposed that the non-radiative recombination might depend exclusively on surface traps, as this blinking mechanism can be inhibited by growing large shells.¹⁴⁶ For C-type blinking, the recombination dynamics can be explained by short-lived shallow trap sites that are activated and deactivated during illumination. This activation and deactivation of trapping might be mediated by adsorbents of the surroundings.¹⁴⁸

Since the different blinking mechanisms alter the rates of the radiative and non-radiative decays in different ways, the respective mechanism in a QD can be identified by the fluorescence lifetime-intensity distributions (FLIDs), as illustrated in Figure 2.16. The distinct on- and off/grey-states are marked as red dots. Blinking events that are faster than the chosen bin time are distributed in between those states (also called PL flickering).¹⁴⁶

The intensity I is proportional to the QY, which can be expressed as

$$I \propto \text{QY} = \frac{k_r}{k_r + k_{nr}} = \tau k_r = \frac{\tau}{\tau_r}, \quad (2.20)$$

with k_r and k_{nr} the rates of radiative and nonradiative recombination, τ_r the radiative lifetime and the lifetime τ .¹⁵¹

For Auger blinking, the dark state is dominated by recombination of a charged trion state. Due to the doubled amount of recombination possibilities, the rate of radiative recombination k_r in the bright state becomes $2k_r$ in the dark state. As shown by Galland et al., the distribution of the intermediate states then follows a curved shape.¹⁴⁶ Opposed to that, in hot-carrier blinking, no correlation of intensity and lifetime is observed. This is due to the interception of charge carriers before they reach the exciton level. Here, trapped charge carriers recombine non-radiatively through a bypass channel without affecting the dynamics of the radiative recombination. In the dark state, the intensity is therefore decreased, while the lifetime stays unchanged. Then again, in bandedge-carrier blinking, intensity and lifetime are correlated linearly.¹⁴⁸ Similar to B-type blinking, intensity fluctuations occur due to activation and deactivation of non-radiative channels. Therefore, the radiative rate k_r stays constant, while the non-radiative rate changes. In contrast to B-type blinking, however, the non-radiative channel is in direct competition with the radiative channel, resulting in the linear dependence of intensity and lifetime for bright and dark/dim states.

Consequently, the analysis of the scaling of PL intensity and PL lifetime may be used as indication for the blinking mechanism in a QD. Rearranging Equation 2.20 to the

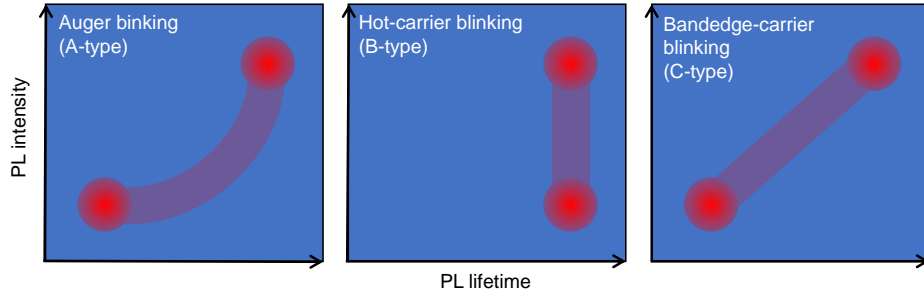


Figure 2.16: Schematic illustration of the fluorescence lifetime-intensity distribution (FLID) in each blinking mechanism. The red points mark the on- and off-states that are clearly distinguishable. Switching events faster than the chosen bin time result in an intensity in between, which is indicated by the purple areas. (Adapted from ref. [147]).

radiative lifetime τ_r allows for the determination of their ratios in the dim and bright state. For Auger blinking the ratio of the radiative lifetimes of the neutral bright state X and the charged dim state X* is

$$\frac{\tau_r(X)}{\tau_r(X^*)} = \frac{\tau(X) I(X^*)}{I(X) \tau(X^*)} = 2, \quad (2.21)$$

since two charge carriers have chances to recombine with one other charge carrier in a trion. For bandedge-carrier blinking the ratio of the radiative lifetimes of the on- and off-state is one.¹⁵¹ However, this only applies when B-type blinking is not present.

2.3.2 Statistical Blinking Analysis

Power-Law Distribution

In the early stages of analyzing the blinking dynamics of QDs, it was found that on- and off-times are distributed exponentially as the recombination dynamics in a three-level model of VB, CB and trap state with fixed rates would suggest. Instead, it was found that the probability distribution $P(\tau_{\text{on/off}})$ of the on- and off-times $\tau_{\text{on/off}}$ is described by an inverse power law

$$P(\tau_{\text{on/off}}) \propto \tau_{\text{on/off}}^{-m_{\text{on/off}}}, \quad (2.22)$$

with $m_{\text{on/off}}$ as the respective power-law exponent.¹⁵² This led to the realization that the rates of trapping and detrapping of charge carriers are not fixed, but distributed. Consequently, several models were proposed to explain this phenomenon, of which some are briefly described in Figure 2.17.¹⁵³ The models shown in Figure 2.17(a–c) all have in common that tunneling of charge carriers to trap states and back is assumed, while the

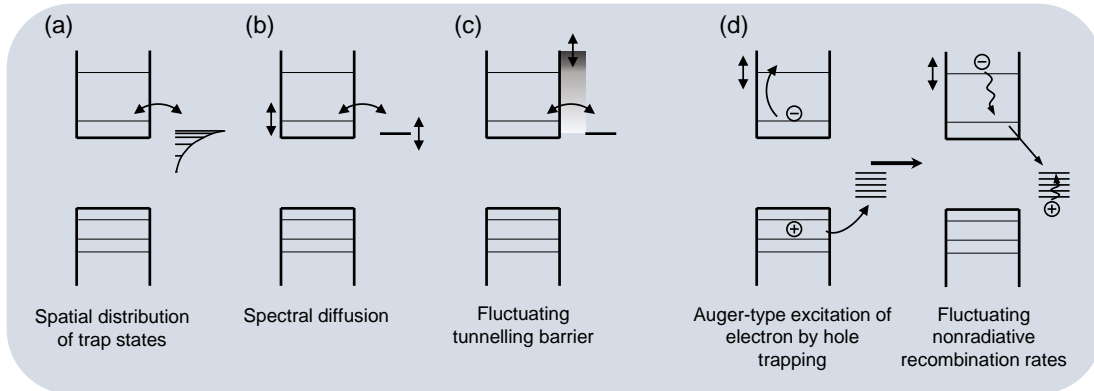


Figure 2.17: Schematic representation of some models proposed to explain the power-law distribution of on- and off-states in QD blinking. (a) Trapping and Detrapping of an electron to one of a manifold of trap states with different depths and distances. (b) Spectral diffusion of energy levels of NC and trap state. (c) Fluctuating height and/or width of tunneling barrier. (d) Fluctuating non-radiative recombination rates, mediated by relaxation processes of trapped hole and excited electron. (Adapted from ref. [153]).

rates of trapping and detrapping are varying for different reasons. These models include the existence of a distribution of trap states with energybarriers of different heights and distances,¹⁵⁴ the occurrence of spectral diffusion of the energy levels of the QD and the trap states,¹⁵⁵ and fluctuations in height and/or depth of the tunneling barrier to a single trap state, induced by fluctuations in the QD environment.¹⁵⁰ In the model shown in Figure 2.17(d), the blinking statistics are explained by fluctuating non-radiative recombination rates. An Auger-type excitation of the electron by hole trapping is assumed. Fluctuations of the relaxation times of hot charge carriers due to spectral diffusion of the excited state would then lead to varying nonradiative recombination rates.¹⁵⁶

The analysis of the PL time traces, the FLIDs and the distribution of the on- and off-times can yield a lot of information about the QD blinking mechanism and was applied intensively by many groups in the past. However, those methods share one disadvantage, as they all depend on the bin time chosen for representation of the data. Therefore, autocorrelation is described below as a method for analyzing blinking that is independent of time binning and immune to biased interpretation.

Autocorrelation

The autocorrelation function describes the degree of similarity of a time-varying signal to itself with continuous time delays over a given time span. The autocorrelation function

$g^{(2)}(\tau)$ is calculated according to

$$g^{(2)}(\tau) = \frac{\langle I(t)I(t+\tau) \rangle}{\langle I(t) \rangle^2}, \quad (2.23)$$

with $I(t)$ as intensity at a time t , τ as time delay, and $\langle \rangle$ indicating averages over the measurement time.

The autocorrelation function is an additional tool to analyze the blinking dynamics. In contrast to the conventional methods, this analysis obtains the advantage of being independent from time binning and setting intensity thresholds. Therefore, it opens the opportunity to analyze fast blinking events and data sets where fluctuations compete with shot noise.

To illustrate the interpretation of autocorrelation functions, some examples are shown in Figure 2.18. Figure 2.18(a) shows a fully uncorrelated constant signal. The corresponding autocorrelation function in Figure 2.18(b) is constantly $g^{(2)} = 1$. Any kind of fluctuations lead to values $g^{(2)} > 1$ at some times. The data for a background measurement with an avalanche photodiode (APD) are shown in Figure 2.18(c). The fluctuations of the signal lead to values of $g^{(2)} > 1$ in the corresponding autocorrelation in Figure 2.18(d). However, since the fluctuations of the intensity of the noise are low (compared to fluctuations due to blinking), the values for $g^{(2)}$ are only insignificantly > 1 . Figure 2.18(e) shows model time-traces with intervals of decreased intensities of 10 s, 5 s and 2 s. The corresponding autocorrelation functions in Figure 2.18(f) exhibit a sharp bend at the respective times of the interval duration. Figure 2.18(g) shows model time-traces with varying numbers of 5 s-intervals. The corresponding autocorrelations in Figure 2.18(h) exhibit different shapes at the respective times. An increased number of intervals in the time trace leads to higher "slopes" in the autocorrelation function. These examples show how the autocorrelation function can give information about blinking events in a PL intensity time-trace. Fitting the autocorrelation function can also be used to derive the power-law exponents of the on- and off-time distributions. It has to be noted, however, that a number of data sets with statistical significance is required for the determination of power-law exponents as considerable deviations in individual cases have been observed.^{157,158}

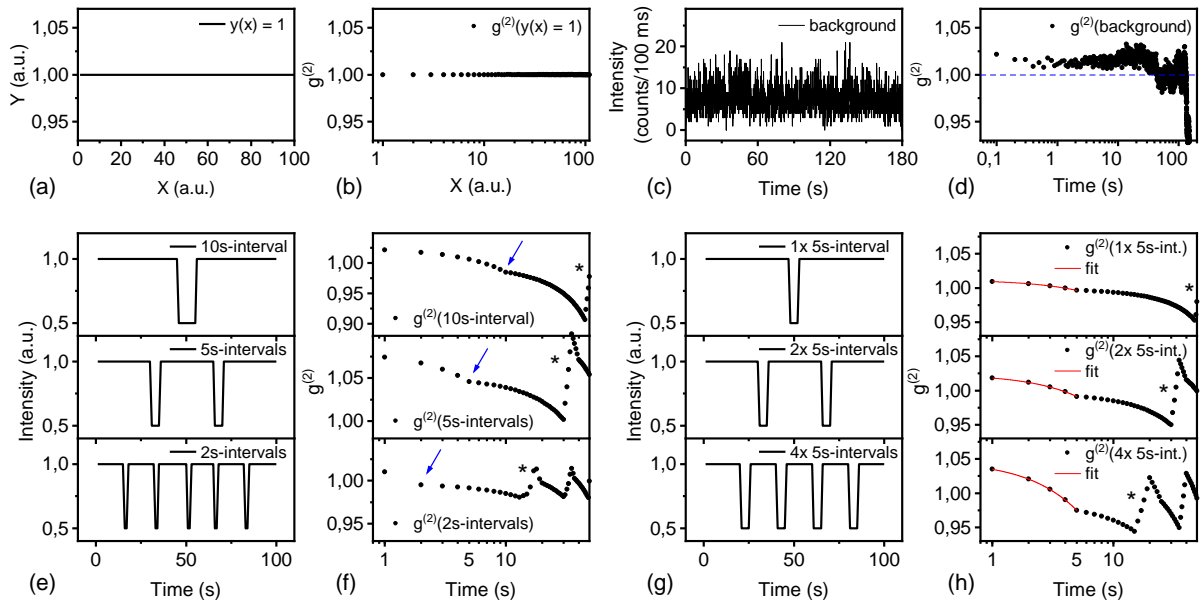


Figure 2.18: Examples for test signals and their autocorrelation functions. (a,b) Function $y(x) = 1$ and its autocorrelation $g^{(2)}$. (c,d) Intensity time-trace of the background noise for a typical measurement with an APD (Poisson distributed) and its autocorrelation $g^{(2)}$. (e,f) Models for intensity time-traces with 10 s-, 5 s- and 2 s-intervals and their autocorrelations $g^{(2)}$. The blue arrows in (f) mark the steps in the autocorrelation data resulting from the lengths of the respective intervals in (e). (g,h) Models for intensity time-traces with one, two and four 5 s-intervals and their autocorrelations $g^{(2)}$. The fits in the data regions, attributed to the intervals, highlight the dependency of the decrease in $g^{(2)}$ with the number of intervals in (g). (*): Spikes at higher times in $g^{(2)}$ are due to the periodicity of the model time-traces and are absent in real data.

3 Methods

After summarizing the theoretical concepts, as well as the state of the literature related to the topic of this thesis, in this chapter, the experimental methods will be introduced. While this chapter is restricted to the principles of the experimental methods, more detailed information about the experimental procedures is given in Chapter 6.

3.1 Confocal Microscopy

Confocal spectroscopy is a widely used technique for the optical investigation of nanostructures, in particular for the investigation of single structures. In contrast to wide-field spectroscopy, only a small spot of the sample is illuminated at a time and the detected light originates only from that area. In order to create an image of fluorescent emitters on a substrate, the excitation light needs to be scanned over the sample. Another important modification compared to conventional optical spectroscopy is the second lens that focuses the emission or scattered light on the detector. The principal setup of a confocal laser microscope is depicted in Figure 3.1. The sample is located in the focal plane of lens 1 (typically an objective), which focuses the excitation light on the sample and collects the emission light. By focusing the emission light on a detector and blocking light of the surroundings with a mechanical barrier such as a pinhole, detection only occurs from one single area that is confined in all three spatial dimensions. For the investigations carried out in this thesis, APDs were used as detectors, for example to create PL scans. The APDs used have a detection area so small that they themselves effectively act as a pinhole. When measuring spectra, the emission or scattered light is focused on the entrance slit of the spectrometer. The slit then acts as a mechanical barrier, confining the detection area in the x-direction, while choosing a narrow region of interest on the detection chip confines the detection area in y-direction. Thus, light from the surroundings is blocked and the signal-to-noise ratio is enhanced, which is crucial for single-structure investigations.

3.1.1 Focal Spot Size

The resolution of a confocal laser microscope is limited by diffraction of light that is focused by a lens. At scales within the resolution limit, the diffraction of light at the

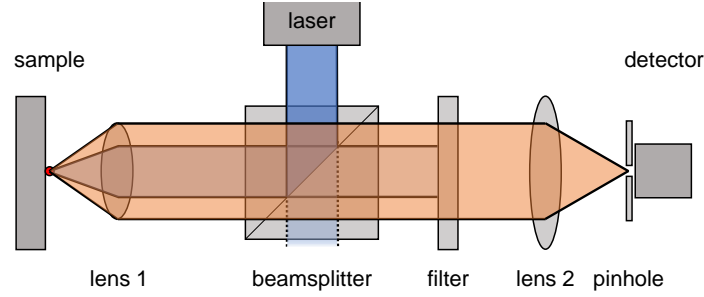


Figure 3.1: Sketch of the general setup of a confocal laser microscope. Light from the focal point of lens 1 is focused through a pinhole on a detector by lens 2, thus enabling only detection of light from a confined space. Typically, filters are used to block the excitation light (blue) from the emission light (orange).

optical components results in the formation of spherical blurred spots instead of sharp contours. The expansion of such a spot in the lateral plane can be described by an Airy pattern according to

$$r_{\text{Airy}} = 0.61 \frac{\lambda}{\text{NA}} = 0.61 \frac{\lambda}{n \cdot \sin \alpha}, \quad (3.1)$$

where r_{Airy} is the radius of the first diffraction ring, λ is the wavelength and NA is the numerical aperture of the objective, which depends on the refractive index of the immersion medium n and on the half of the opening angle α .¹⁵⁹

Most commonly, the resolution limit of a confocal microscope is defined by the possibility of distinguishing two neighboring point objects. According to the Rayleigh criterium, two points are distinguishable if the intensities of the point spread functions that describe the intensity distribution of the blurred spots are at their half maximum at the point of intersection.

Approximations for the full width at half maximum (FWHM) that are often used for the resolution of confocal microscopes are

$$FWHM = 0.40 \frac{\lambda}{\text{NA}} \quad (3.2)$$

in lateral direction and

$$FWHM = 0.45 \frac{\lambda}{\text{NA}} \quad (3.3)$$

in axial direction.¹⁶⁰

When investigating nanostructures via confocal spectroscopy it is crucial to estimate the excitation power that is effectively applied to the sample. A first approximation of the power density can be given by the excitation power over the spotsize, which is estimated by using the FWHM as diameter. If small objects, such as zero-dimensional QDs, are illuminated and the number of excited excitons is to be estimated, the determination of

the intensity maximum can yield a better approximation. To do so, it is necessary to consider the intensity distribution of the excitation light in the focal plane. In the waist of a Gaussian beam the radial intensity distribution $I(r)$ is given by

$$I(r) = I_0 e^{-\frac{2r^2}{w^2}}, \quad (3.4)$$

with the distance r from the center, the intensity I_0 at $r = 0$ and the beam radius w .¹⁶¹ The beam radius w , is defined as half the width of the distribution function at which the intensity has fallen to $1/e^2$ of its maximum. The power P_0 in the beam waist can be written as the integral of the intensity distribution according to

$$P_0 = 2\pi \int_0^\infty I(r)r dr = \frac{\pi}{2} w^2 I_0. \quad (3.5)$$

Therefore, the intensity at the center of the illuminated area is related to the excitation power $P = P_0$ according to

$$I_0 = \frac{2P}{\pi w^2}. \quad (3.6)$$

When using pulsed excitation, the photon flux J is given by the number of photons that arrive per pulse per area. Therefore, the photon flux J_0 , which is considered for the excitation of excitons, is calculated according to

$$J_0 = \frac{I_0}{f} \frac{\lambda}{c \cdot h}, \quad (3.7)$$

with the frequency f , the speed of light c and the Plank constant h . By regarding the absorption cross-section δ of the material, the number of the excited excitons N_{Exciton} can be estimated according to

$$N_{\text{Exciton}} = \delta \cdot J_0 = \mu_i \cdot V \cdot J_0 \quad (3.8)$$

with the empirical intrinsic absorption μ_i and the particle Volume V .¹⁶²

3.2 IR spectroscopy

IR light is energetically in the range of the vibrational levels of molecular bonds. If a molecule has a changeable dipole moment, vibrations can be generated by absorbing IR light. The vibrational energies depend specifically on the respective bond, allowing chemical substances, especially organic molecules, to be analyzed. Therefore, Fourier-transform infrared (FTIR) spectroscopy is a popular method since extensive qualitative

and also quantitative information can be gained for a sample quickly and with low experimental efforts. Especially for functional groups, such as the head groups of ligands used in nanochemistry, FTIR spectra provide specific information. For measuring FTIR spectra, either the transmission or the reflection can be detected. For transmission measurements the sample is commonly embedded in a medium that does not interact with IR light, such as a KBr pellet. This preparation step can be discarded when measuring in the attenuated total reflection (ATR) mode.

The sample stage for ATR-FTIR measurements is usually given by a crystal. At contact of the IR light with the interface of crystal and air, the light gets completely reflected if the incidence angle lies below a certain critical angle (total reflection angle). However, at the interface an evanescent wave reaches inside the medium, in which the wave cannot propagate. There, the light can get absorbed by the sample, enabling the direct measurement of IR spectra with material in contact or close proximity to the interface.

3.3 Electron Microscopy

To investigate the structure of NCs, electron microscopy is a technique of fundamental importance. Due to the interaction of solid material with electrons, structural features can be resolved with a resolution that even allows for the imaging of individual atomic planes. The general principle of electron microscopes is similar to the principle of optical microscopes. Instead of photons, accelerated electrons are used to analyze the sample. The theoretical resolution limit is still set by the wavelength and the numerical aperture (NA). However, the wavelength of accelerated electrons that are used in electron microscopy lies in the range of a few picometer, thus enhancing the theoretically achievable resolution extensively. In practice, the resolution is not set by the diffraction limit as for optical microscopes, but by technical limits, such as imperfect lenses. Still, the resolution of modern transmission electron microscopes lies in the sub-nanometer regime.¹⁶³ The techniques that were applied in this work are transmission electron microscopy (TEM), scanning electron microscopy (SEM) and energy dispersive X-ray (EDX) spectroscopy.

3.3.1 Transmission Electron Microscopy

In order to use TEM the sample has to be sufficiently thin. The detected electrons exhibit information of the medium they transmitted. The contrast in a TEM image is gained by scattering and diffraction events of the electrons while traversing the sample. For the analysis of colloidal NCs this method is advantageous in many respects. Due to their expansion in the nanometer regime, NCs are usually thin enough for the transmission of electrons. The sample preparation for colloidal structures is quite easy, as a diluted

solution can simply be dropcasted on a thin substrate (e.g. carbon film on a copper grid), to obtain monolayers or individual structures for investigation. Thus TEM represents an important tool for the analysis of chemically synthesized NCs. One drawback of TEM and electron microscopy in general is that this method is quite invasive. Especially for semiconducting nanostructures, the electron beam can affect the electronic and optical properties severely, which has to be considered when performing correlation studies. For example, the PL of NCs is usually quenched after contact with the electron beam and the structure can be damaged due to melting and reorganization of atoms.

3.3.2 Scanning Electron Microscopy

In contrast to the conventional TEM method, in which a fixed electron beam is used and the transmitted electrons are detected, in SEM a focused electron beam is scanned over the sample and electrons are detected that scatter backwards from the sample. The resolution is limited by the width of the incident electron beam, which can be as low as 1 nm.¹⁶³ In contrast to TEM, this method can be applied to thicker specimens, whereby only the surface is examined. Ideally, the substrate is electrically conductive in order to avoid charging effects caused by the electron bombardment. The detected number of scattered electrons when scanning the sample results in the formation of a contrast in the image. Several processes that occur upon interaction of the electron beam with the material can be used to gain different information.

In SEM, electrons that are detected after elastic scattering with the nuclei of the specimen are called backscattered electrons. Detection of backscattered electrons can contribute to the contrast of the image, but usually, the most important electrons for the creation of a SEM image are secondary electrons. If inelastic scattering with outer-shell electrons occurs, the electrons can be separated from their nuclei and move as secondary electrons through the material exhibiting further scattering events. If secondary electrons are generated close to the surface (<2 nm) they might escape the material in which case they can be detected as well. Due to the small escape depth of secondary electrons, their detection yields images, which solely display the topography.¹⁶³

3.3.3 Energy Dispersive X-ray Spectroscopy

In both TEM and SEM not only scattered or diffracted electrons might be detected. If inner-shell electrons are separated from their nuclei by inelastic scattering, electrons of higher energy levels can act as their substitutes. The energy released by the relaxation process can be detected as X-ray emission. Since this energy is specific for each element, the chemical composition of the specimen can be analyzed.¹⁶³

4 Results and Discussion

In the following chapter, the most important results obtained during in the course of this work are presented. The majority of the work concerns CdSe QWs and their optical properties. First, the results for the synthesis and the characterization will be shown and discussed. For the optical properties, the influence of the chemical surroundings were investigated. A special focus was set on photoinduced processes observed with oxygen in the gaseous surroundings. Additional experiments with other substances are discussed briefly to conclude this section.

The second part of this chapter deals with the optical properties of CdSe/CdS core-shell QDs. After investigating the effect of oxygen on the PL properties of thin films, the focus was set on the influence of oxygen on the blinking behavior.

4.1 CdSe Quantum Wires – Chemical Analysis

4.1.1 Composure and Surface

CdSe QWs were synthesized via the SLS approach. As catalysts, Bi-particles with an average diameter $d = 7.4 \pm 1.3$ nm were used. Cd and Se were provided by the precursors Cd(DOPA)₂ and Se:TOP. The synthesis was performed at 300 °C with TOPO as solvent. Figure 4.1(a) shows a representative TEM image. The QWs reach dimensions of several

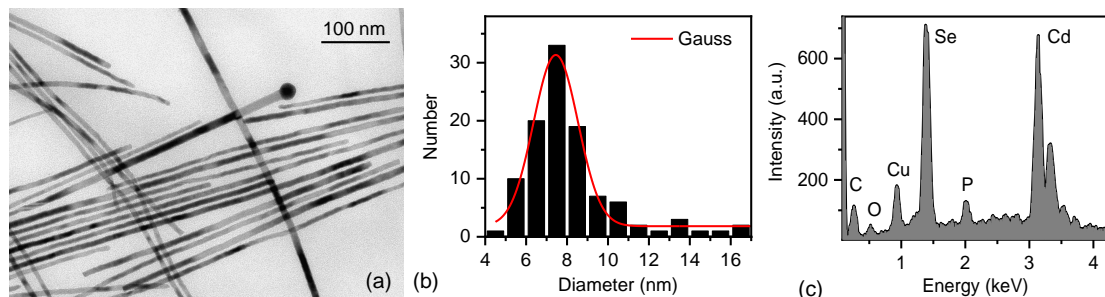


Figure 4.1: CdSe QWs. (a) TEM image. (b) Histogram of the size distribution fitted with a Gaussian (Maximum = 7.5 nm; FWHM = 2.6 nm). (c) EDX spectrum of CdSe QWs on a Cu substrate.

Table 4.1: Se:Cd ratios determined by ICP-MS and EDX measurements of identically synthesized samples. The given values for the EDX measurements are the averaged results of ten measurements each.

CdSe QW sample	Se:Cd ratio (ICP-MS)	Se:Cd ratio (EDX)
1	1.08	1.17
2	1.16	1.41
3	1.14	1.37
4	0.95	–
5	1.18	–
6	1.17	–
average	1.11	1.32
standard deviation	0.0785	0.105

micrometer in length, while the diameters are controlled by the size of the Bi-particles. For the sample shown in Figure 4.1, QWs with an average diameter of $d = 8.2 \pm 2.3$ nm were obtained. The corresponding histogram of the size distribution is shown in Figure 4.1(b). Apart from the sporadic occurrence of a few thicker wires, the size distribution can be represented with a Gauss fit.

EDX Measurements and ICP-MS

The composition was analyzed by EDX spectroscopy and inductively coupled plasma mass spectrometry (ICP-MS). Figure 4.1(c) shows an example of an EDX spectrum. Three peaks can be assigned to C, O and P, which resemble the elements of the organic ligands, while the two main peaks are assigned to Se and Cd. Interestingly, the Se content is larger than the Cd content. As alternative method to evaluate the Se/Cd ratio, ICP-MS measurements of CdSe QWs that were dissolved in aqua regia were conducted. The results of the measurements of three samples for EDX spectroscopy and six samples for ICP-MS are summarized in Table 4.1. The average Se/Cd ratio as determined by EDX spectroscopy is 1.32 ± 0.105 . The average Se/Cd ratio as determined by ICP-MS is 1.11 ± 0.0785 . With both methods an excess of Se was found. This is an important finding, considering that conventionally most colloidal II-VI semiconductor NCs exhibit a metal-rich surface.^{50,164} Undercoordinated metal ions at the surface then get passivated by L- or X-type ligands, such as TOPO and di-*n*-octylphosphinic acid (DOPA) that are also used in the CdSe QW synthesis. However, identification of an excess of Se in the CdSe QWs suggests the presence of Se ions at the QW surface.

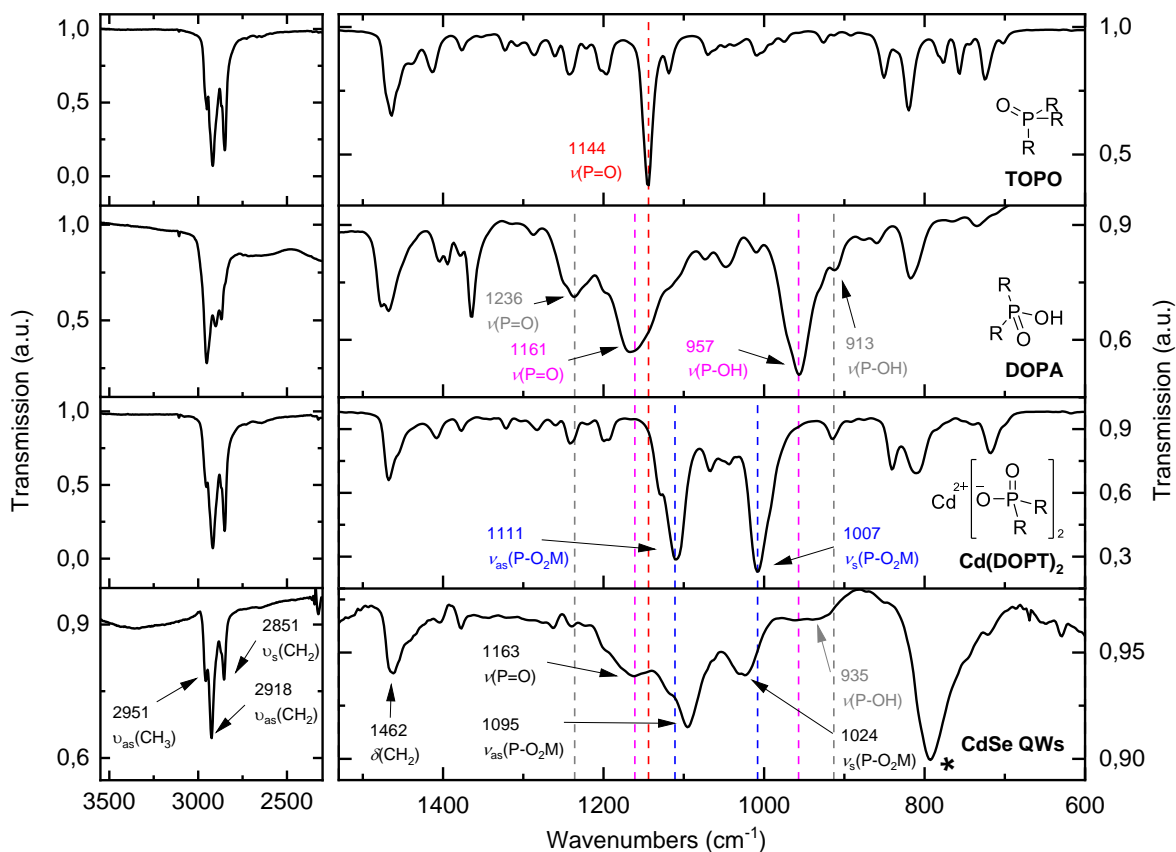


Figure 4.2: ATR-FTIR spectra of TOPO, DOPA, Cd(DOPT)₂ and CdSe QWs. The characteristic peaks of the headgroups of TOPO, DOPA and Cd(DOPT)₂ are marked with dashed lines. (*) marks a peak which is assigned to vibrations of residual toluene in the CdSe QW spectrum.¹⁶⁵ Adapted from Kusterer et al.¹⁶⁶

Organic Ligands

The main part of the investigations carried out in this thesis focuses on the influence of the chemical environment on the properties of the CdSe NWs and on photoinduced processes that occur on the surface. Therefore, the nature of the surface was further investigated. To investigate the organic ligand shell FTIR spectroscopy was employed. At first, the FTIR spectra of CdSe QWs are compared to the spectra of the initial molecules involved in the synthesis. Results of further experiments concern the purification process. At last, results of a thermogravimetric analysis (TGA) study are presented.

IR spectra The FTIR spectra of the CdSe QWs are compared to the spectra of the initial molecules involved in the synthesis, as well as to spectra for colloidal NCs reported in the literature.^{167–169}

In Figure 4.2 ATR-FTIR spectra of TOPO, DOPA, Cd(DOPT)₂ and CdSe QWs are shown. The spectra of TOP and TOP:Se are disregarded, since they do not exhibit any peaks that clearly distinguish them from the other ligands. In all spectra the C-H stretch vibrations of the aliphatic chains around 2900 cm⁻¹ are observed, as well as the bending vibration of CH₂ groups at 1462 cm⁻¹. For TOPO, the characteristic peak of the P=O stretch vibration is observed at 1144 cm⁻¹.¹⁶⁷ The spectrum of DOPA exhibits two main peaks, which are assigned to the P=O stretch vibration at 1161 cm⁻¹ and the P-OH stretch vibration at 957 cm⁻¹ of the phosphinic acid head group.¹⁷⁰ Interestingly, peaks at 1236 cm⁻¹ and 913 cm⁻¹ are also observed (grey lines). Those peaks might be assigned to impurities consisting of phosphonic acid species.^{169–171}

The spectrum of Cd(DOPT)₂ exhibits significant changes compared to that of DOPA. The peaks of the P=O and P-OH stretch vibrations disappear and the spectrum of Cd(DOPT)₂ shows two newly formed peaks at 1111 cm⁻¹ and 1007 cm⁻¹. Those peaks are commonly assigned to the vibrations of the PO₂⁻ moiety bound to the metal.^{168,170} For the nature of the DOPA-metal bond, it is not yet conclusively established if the phosphinic acid head group is delocalized, thus allowing the assignment of the two peaks to asymmetric and symmetric PO₂ stretch vibrations (instead of P=O and P-O⁻/P-OH).¹⁷⁰ However, assignments of peaks in that frequency region to asymmetric and symmetric PO₂ stretch vibrations are found in the literature for NCs.^{168,169}

In the spectrum of CdSe QWs, three peaks can be distinguished clearly at 1163, 1095 and 1024 cm⁻¹. In the literature for CdSe NCs, there are some discrepancies in the assignment of those peaks. The peak at around 1090 cm⁻¹ was assigned by von Holt et al. to the P=O stretch vibration of surface bound TOPO,¹⁶⁷ while the peaks in this region were later associated with vibrations of the headgroup of phosphonic and phosphinic acid at the NC surface.^{168,169} Based on the latest findings, in this work the peaks at 1095 and 1024 cm⁻¹ are assigned to the asymmetric and symmetric stretch vibration of the P-O₂M headgroup of phosphinic acid ligands. Furthermore, the peak at 1163 cm⁻¹ was assigned to the P=O stretch vibration of surface bound TOPO by Son et al.¹⁶⁹ However, the comparison with the spectrum of DOPA suggests a contribution of the P=O stretch vibration of monodentate bound phosphinic acid to this signal. In addition, the spectrum of CdSe QWs in Figure 4.2 allows for an identification of a peak at 935 cm⁻¹. But due to its low intensity and broad width the identification of this peak is questionable. A similar signal in this region has been associated to the P-OH stretch vibration of phosphonic acid bound to the NC surface.¹⁶⁹ Yet, in this frequency range a peak was also observed for metal bound phosphinic acid.¹⁷⁰ In this case, both identification and assignment are ambiguous.

In summary, this study shows that there are no large amounts of free ligand molecules in the purified CdSe QW sample, as the sharp peaks of the precursor materials are not observed in the FTIR spectrum of the CdSe QWs. Yet, the presence of organic molecules is clearly shown by the detection of various CH vibrations. The FTIR spectrum of the CdSe QWs shows unambiguously the presence of phosphinic acid, as several peaks are observed that can be assigned to the vibrations of the phosphinic acid headgroup. These data suggest that the phosphinic acid acts as ligand to passivate Cd ions at the QW surface. The significant shift of the peaks assigned to the P-O₂M stretch vibration, compared to the P=O and P-OH stretch vibration of DOPA indicates bidentate binding with delocalized electrons in the PO₂⁻ moiety. Furthermore, the observation of peaks assigned to P=O vibrations can be interpreted as either monodentate bound phosphinic acid or surface bound TOPO.

Effect of Purification In colloidal nanochemistry, the products of the synthesis are often purified via centrifugation. Usually, the NCs are precipitated and the smaller byproducts can be removed as they stay in solution. After redispersing the NCs in clean solvent, the process can be repeated until the desired purity is achieved. For CdSe NCs it has been reported that as the number of purification cycles by centrifugation and redispersion increases, the L-type ligands are increasingly washed off, leaving the particles with only X-type ligands in the end.¹⁷² Therefore, an analysis of the purification process might yield further insights about the composition of organic ligands at the surface of CdSe QWs. In particular, the question if L-type ligands, such as TOPO, TOP and TOP:Se are present on the CdSe QW surface was not unambiguously answered by the data presented in Figure 4.2.

ATR-FTIR spectra of CdSe QWs after different numbers of precipitation cycles were analyzed. The spectra in Figure 4.3 show the fingerprint area of CdSe QWs without any purification and after one to seven rounds of precipitation. For the first two spectra the peak of the P=O stretch vibration of free TOPO is dominant. This peak disappears after two cycles of precipitation and the peaks of bound phosphinic acid, as described for Figure 4.2, become visible. Note that the transmission of the samples after two cycles of purification is much higher than in the first two spectra, in which the signal of the free ligands masked the signals of the bound ligands. Interestingly, the spectra change between the second and third precipitation cycle. The peak at 1160 cm⁻¹, associated with the P=O stretch vibration, and the peak at 1463 cm⁻¹, assigned to the bending vibration of CH₂, strongly decrease in intensity. These changes represent the decrease of organic material in this purification step. The large decrease in intensity of the peak assigned to the P=O stretch vibration (1160 cm⁻¹) might be explained by a decrease of

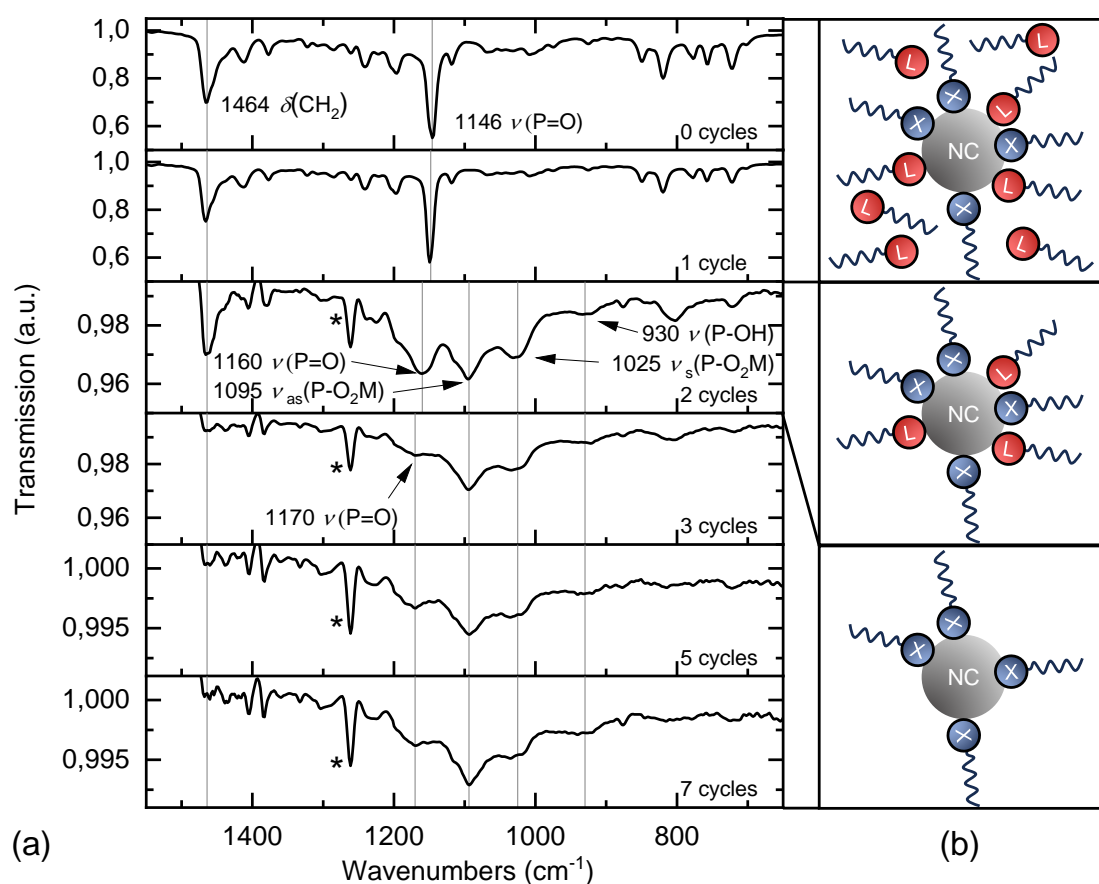


Figure 4.3: Effect of purification on FTIR spectra of CdSe QWs. (a) ATR-FTIR spectra of sample after zero to seven cycles of purification by centrifugation. The peak at 1260 cm^{-1} (marked with *) was identified as artifact. For clarity only the fingerprint region is shown. C-H stretch vibrations at around 2900 cm^{-1} were observed in all spectra. (b) Scheme of ligand passivation of NCs with L- and X-type ligands with progressing purification from top to bottom. Adapted from ref. [172]. (a) is adapted from Kusterer et al.¹⁶⁶

the number of the weakly bound TOPO ligands or monodentate bound phosphinic acid ligands. Assuming that every cycle of precipitation leads to a loss of weakly bound ligands it can be concluded that their amount is negligible after three precipitation cycles, as the spectrum does not change afterwards. This leads to the conclusion that the majority of ligands present at this point is provided by phosphinic acid, which is consistent with findings for CdSe NCs.¹⁷² The effects of purification are schematically illustrated in Figure 4.3(b). The CdSe QWs that were investigated in the PL and Raman study in this work were usually prepared with three cycles of purification. To gain further insight into the composition of the organic ligand shell after three purification cycles, a TGA-FTIR study was performed. This method allows the identification of different ligands by recording spectra at different temperatures as the sample is heated. This allows the identification of ligands whose signal may be masked in the spectra shown above. The results are summarized in the next paragraph.

TGA-IR analysis In order to quantify and differentiate the ligands of the CdSe QWs after three precipitation cycles, TGA-FTIR measurements were conducted. For this, several identically prepared QW batches were deposited dropwise into the TGA crucible, while heating the crucible moderately (50 °C) to accelerate solvent evaporation. During the TGA measurement, the volatile components of the dried samples were investigated by transmission FTIR spectroscopy in the gas phase. For comparison the same experiment was conducted with TOPO and Cd(DOPT)₂, respectively.

Figure 4.4 shows the results of measurements with TOPO, Cd(DOPT)₂ and CdSe QWs. The loss of weight and the derivative thermogravimetric (DTG) curve are plotted in relation to rising temperatures, as shown in Figure 4.4(a). For TOPO, the whole sample evaporates, while the loss of mass starts at around 300 °C. In contrast, Cd(DOPT)₂ evaporates in two steps, while containing 23% of substance not evaporating in the given temperature range. The smaller fraction starts to evaporate at around 200 °C while the majority of the sample evaporates at 400 °C. For CdSe QWs, 47% of the sample evaporates in the temperature range of 200 – 500 °C. The DTG curve reveals an inflection point at 320 °C and a local maximum at 440 °C, indicating changes in the evaporation process.

The fingerprint region of the transmission-FTIR spectra of the evaporation products are shown in Figure 4.4(b). The spectra of TOPO and Cd(DOPT)₂ did not evolve over the measured time, thus only one exemplary spectrum is shown in each case. For TOPO, the peak at 1169 cm⁻¹ is assigned to the P=O stretch vibration of the headgroup. Compared to the spectrum of the solid sample measured with the ATR-FTIR spectrometer, the peak is broadened and shifted by 25 cm⁻¹ to higher frequencies. While the broadening might be explained by the elevated temperatures during the measurement, the shift to

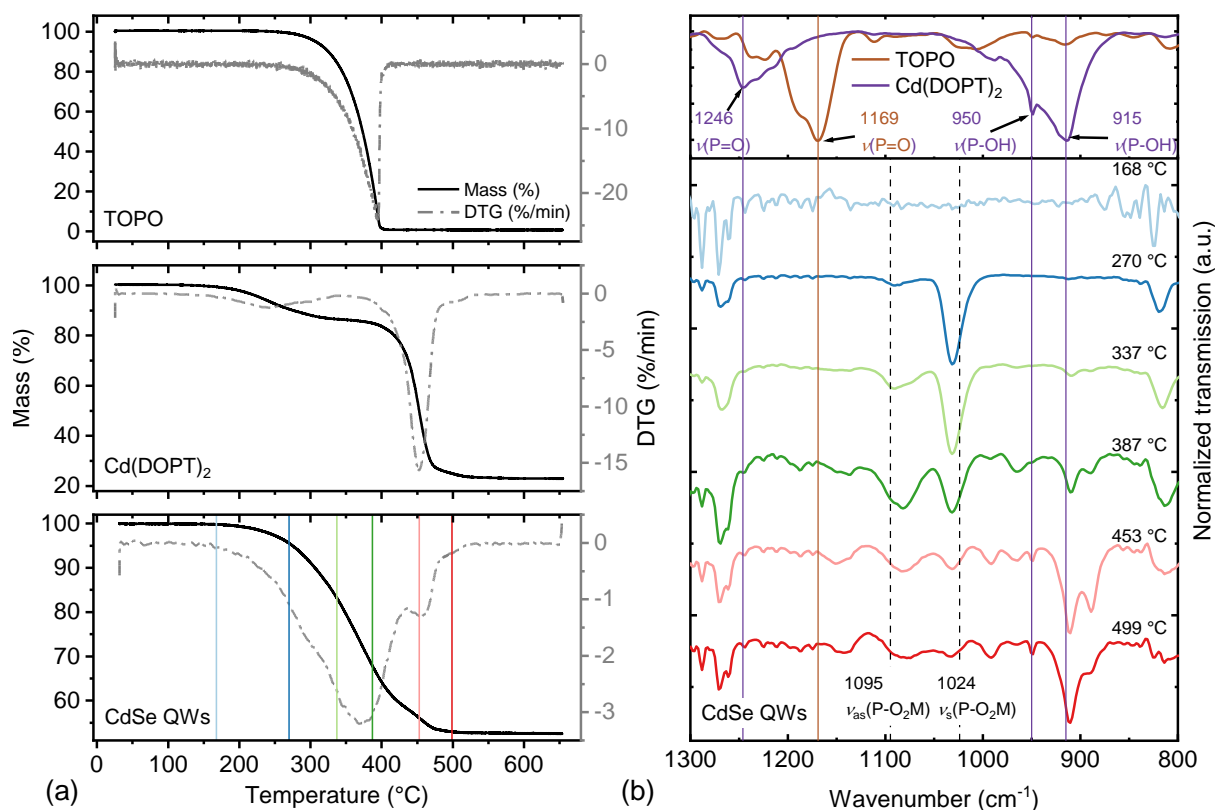


Figure 4.4: TGA-FTIR Measurements. (a) TGA curves of TOPO, Cd(DOPT)₂ and CdSe QWs (heating rate: 10 K/min; inert gas atmosphere). (b) Transmission-FTIR spectra of the evaporation products of the TGA experiments, measured in the gas phase. Peaks identified in the spectra of TOPO and Cd(DOPT)₂ are marked and reference lines are shown in the spectra for CdSe QWs. Additionally, reference lines of the signals of CdSe QWs identified in the ATR-FTIR spectrum of the dried sample (see Figure 4.2) are shown (dashed lines for $\nu_{as}(\text{P-O}_2\text{M})$ and $\nu_s(\text{P-O}_2\text{M})$). For each IR spectrum, the background is subtracted and the intensity is normalized for clarity.

higher frequencies might have various reasons. It is well-known that peak distortion and small frequency shifts can occur when comparing spectra measured in the ATR mode with transmission spectra.¹⁷³ The reason for this is that in the ATR mode, the penetration depth of the evanescent wave at the crystal-sample interface is proportional to the wavelength. Therefore, peak intensities increase toward lower frequencies in ATR-FTIR spectra when compared to transmission FTIR spectra, and the peak maxima, especially of broad peaks, may be shifted toward lower frequencies. Additionally, the different aggregate states (solid and gaseous) of the analyte in the respective measurements may also affect the spectra. For Cd(DOPT)₂, the peaks at 1246, 950 and 915 cm⁻¹ are assigned to P=O and P-OH stretch vibrations, respectively. Surprisingly, the spectrum does not match the ATR-FTIR spectrum of the solid sample. While the peaks, assigned to the P-O₂M headgroup in Figure 4.2, are not observed here, the spectrum exhibits similarities with the spectrum of DOPA. This indicates decomposition due to heating. Yet, the peaks with the largest intensities are usually attributed to the P=O stretch and P-OH stretch vibrations of phosphonic, instead of phosphinic acids. This might indicate oxidation of phosphinic acid to phosphonic acid in the experiment. The observation of two steps in the TGA curve of Cd(DOPT)₂ suggests the presence of another species. However, no distinct features were observed in the FTIR spectra obtained before the major loss of mass at above 400 °C and the only species identified in the spectra are the ones shown in Figure 4.4(b). Therefore, the first stage in the TGA can be explained by residues of water or organic solvent trapped in the solid material, the amount of which is not sufficient to be detected in the FTIR spectrometer.

The transmission-FTIR spectra of the evaporation products of the CdSe QW sample show a development of different peaks with rising temperatures. At temperatures around 300 °C one dominant peak is observed at 1032 cm⁻¹. In this temperature range also a second peak emerges at 1083 cm⁻¹. Along with the development of this peak, increasing intensities at 915 cm⁻¹ are observed, especially at temperatures of 450 °C and above. The changes of the FTIR spectra in these temperature regimes match the observation of the features in the DTG curve. The absence of the peak assigned to the P=O stretch vibration of TOPO shows that no large amount of unbound TOPO is present after three cycles of precipitation, confirming the observations in Figure 4.3. Astonishingly, two of the most dominant peaks observed for CdSe QWs in this experiment are neither present in the spectrum of TOPO nor Cd(DOPT)₂, but are close to the peak positions assigned to the P-O₂M group, observed for CdSe QWs in the ATR-FTIR spectra. While the transmission-FTIR spectrum of the evaporated Cd(DOPT)₂ suggests decomposition of the precursor, the spectra measured for the CdSe QWs can be assigned to phosphinic acid species bound to Cd. The first conclusion is that the bond of undercoordinated Cd at the

QW surface to the ligand molecules is apparently stronger than the bond to the Se atoms in the QW. Secondly, the sequence of the observation of the peaks in this measurement might provide information about the binding conformation of the phosphinic acid head group. The peaks at 1083 and 1032 cm^{-1} were originally assigned to the asymmetric and symmetric stretch vibration of the PO_2^- moiety, bound to the particle surface.¹⁶⁸ Yet, it was already questioned by Alexandratos et al., if the electrons in the phosphinic acid head group are really delocalized, allowing the assignment of a symmetric and asymmetric vibration.¹⁷⁰ The observation of an independent development of the intensity of those two peaks contradicts with an assignment to two vibrations of the same species. Instead, these data suggest the assignment of the peak at 1032 cm^{-1} to a P-OM vibration and the peak at 1083 cm^{-1} to a P=OM vibration. While both vibrations originate from surface bound phosphinic acid, the coordination to the surface is different. Another observation which has to be taken into account, is that the development of the intensity of the peak at 1083 cm^{-1} is linked to the development of the peak at 915 cm^{-1} , assigned to the P-OH vibration. This combination of peaks can be assigned to phosphinic acid bound monodentate via the P=O group to the QW surface. Those interpretations can be seen as good indicators, that monodentate bound phosphinic acid is present at the surface. However, the decomposition processes are not entirely resolved and up to this point the assignment of the respective IR signals is not unanimously clarified in the literature.^{167–170} Therefore, these data allow several ways of interpretation. For example, it is not clear, why the P-OH peak at 915 cm^{-1} dominates the spectrum at high temperatures while no related P=O vibration is observed. Furthermore, another way of interpretation could be the assignment of the peak at 1032 cm^{-1} to the P=O stretch vibration of surface bound TOPO, even though this would deviate from existing literature.¹⁶⁷

In summary the IR data shows repeatedly the presence of phosphinic acid as X-type ligand at the CdSe QW surface. The comparison of the IR spectra at different stages of purification suggest the loss of the majority of L-type ligands after the second centrifugation of the sample. The TGA measurements revealed that 47% of the sample decomposes and evaporates at higher temperatures. The IR spectra of the evaporation products allow several ways of interpretation concerning the nature of surface coordination, while indicating at least partial monodentate binding of phosphinic acid.

4.2 Optical Properties of CdSe QWs

The optical properties of semiconductor nanostructures are defined by their size, shape and composition. While the preceding section focused on the examination of these parameters, the subsequent sections delve into the ways in which the optical properties

are impacted, particularly by the surrounding chemical environment. The investigations focus on the PL and Raman properties of CdSe QWs. For the evaluation of different effects on the PL properties of nanostructures it can be helpful to set up a theoretical model on which the influences of different parameters can be tested. Therefore, the results of COMSOL simulations for the PL properties of CdSe QWs are presented and discussed before addressing the results of the experimental investigations.

4.2.1 Quantization in CdSe QWs

The main part of this work deals with changes of the PL properties of CdSe QWs, induced by changes of their environment. In order to estimate changes in the PL emission energy, the excitonic energies in a model QW structure were simulated via COMSOL. According to the procedure reported by Panfil et al. (see Section 2.1.1), the energy contribution to the effective band gap due to quantization E_{quant} and due to Coulomb interactions E_C were calculated in a cylindrical body of 100 nm length and various diameters. As relative permittivities, $\varepsilon_{\text{CdSe}} = 9.5$ and $\varepsilon_{\text{Ligands}} = 2.3$ were applied within and outside the wire, respectively, to simulate the excitonic energies in a CdSe QW surrounded by organic ligands. The relative permittivity for the ligands is estimated by reducing the relative permittivity of a TOPO monolayer ($\varepsilon_{\text{Ligands}} = 2.6$)¹⁷⁴ to account for an incomplete passivation by ligands.³¹ Calculations are performed with the potentials $V_{\text{in}} = 0$ eV inside and $V_{\text{out}} = \pm 5$ eV outside the structure.³⁰ All relevant parameters are summarized in Table 4.2.

Table 4.2: Parameter for COMSOL simulations.

Parameter	m_h	m_e	$\varepsilon_{\text{CdSe}}$	$\varepsilon_{\text{Ligands}}$	V_{in}	$V_{\text{VB,out}}$	$V_{\text{CB,out}}$
Variable	$0.50m_0$	$0.12m_0$	9.5	2.3	0 eV	-5 eV	5 eV
Reference		[116]		[31]			[30]

The ulterior motive of these theoretical considerations was to gain a better understanding of the parameters affecting the PL emission energy of QWs. For example, an advanced understanding of the effects of the surrounding dielectric medium and of charged species could aid in the interpretation of experimental data. To begin with, the most prominent effect for the PL emission energy of semiconducting nanostructures is investigated — the size quantization.

Figure 4.5(a) shows the contribution of quantization and Coulomb energy to the energy of excitons in CdSe QWs with diameters in the range of 4 – 16 nm as calculated with COMSOL. With decreasing diameter, the energy contribution increases. For comparison,

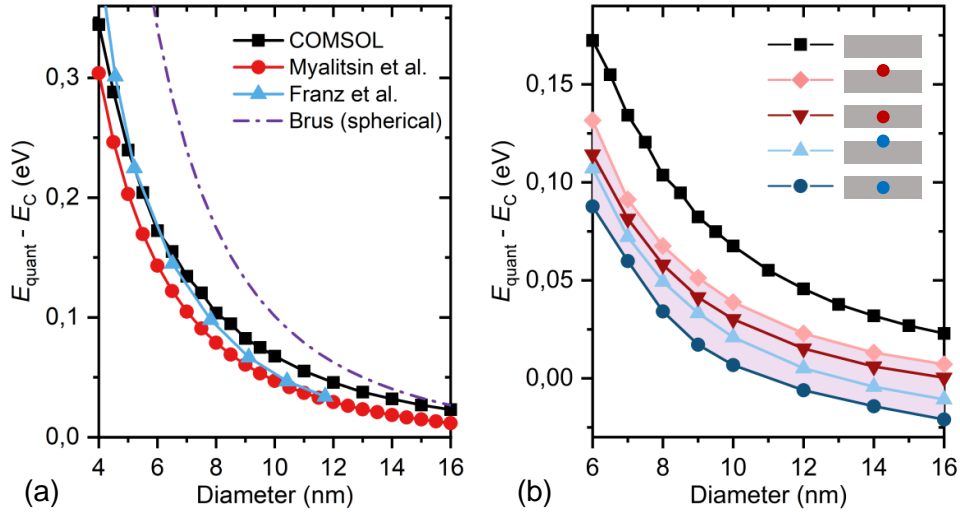


Figure 4.5: COMSOL simulations of (a) uncharged and (b) charged ground-state excitons in CdSe QWs. (a) Energy contribution due to quantization E_{quant} and Coulomb interactions E_C in comparison with calculations from the literature.^{116,119} (b) Comparison of energy contributions with positive (red) and negative (blue) point-charges that are either located within the model QW or at its surface (point inside square versus point at the edge in the legend).

the curve for spherical particles calculated with the BRUS equation (Equation 2.7) is shown.¹¹⁶ The increase in the energy contribution with smaller diameters is significantly lower for the wires than for spherical particles. This illustrates the higher contribution due to confinement in three dimensions instead of two. The data derived by COMSOL are further compared with the data of the studies of Myalitsin et al.¹¹⁶ and Franz et al.¹¹⁹ In the study by Myalitsin et al. an analytical formula, developed by Slachmuylders et al.³² was used, which already includes the effects on the Coulomb energy caused by the dielectric mismatch. In contrast, Franz et al. used an iterative method, much like the strategy applied with COMSOL. In this self-consistent approach the effect of the Coulomb interaction on the wavefunction is implemented. When calculating the energies with a formula, such as the Brus equation for dots or the formula used for wires by Myalitsin et al., the wavefunction is calculated independently. The calculations by Franz et al. were performed with a home written MATLAB script, while the polarization contribution due to image charges, as well as changes of the effective mass at the QW surface (Ben Daniel-Duke boundary conditions) are neglected.¹¹⁹ Especially the latter should be responsible for the deviations in the slopes of the data reported by Myalitsin et al. and Franz et al.¹¹⁹

The general evolution of the datapoints derived by COMSOL is an almost exact copy of the data derived by Myalitsin et al., apart from an absolute offset. The method applied with COMSOL is in general more similar to the method applied by Franz et al. as they are

both self-consistent. However, in COMSOL the polarization effects and the Ben Daniel-Duke boundary conditions are implemented. The absolute offset between the COMSOL data and the data of Myalitsin et al. already occurs when only considering the quantization energy. This might be due to a limitation in resolution in the COMSOL simulations, leading to an overestimation of the quantization energy. Furthermore, some deviations did occur for the Coulomb energy due to the differences in implementing the polarization terms. In COMSOL, the polarization contribution is approximated in a self-consistent manner by solving the Poisson equation with alternating relative permittivities, instead of solving the analytical formula given by Slachmuylders et al.³² Due to the self-consistent procedure applied in COMSOL the polarization terms become neglectable. Even though the result is close to the result of Myalitsin et al., it has to be noted that the accuracy of the approximated contribution due to polarization is questionable. Therefore, this method is not suitable to estimate the small variations in the emission wavelength which could occur when changing the surrounding dielectric medium. After this study was already completed, an improved method for the approximation of the polarization energy via COMSOL was published by Panfil et al.¹⁷⁵

As a next step, point charges were introduced to estimate the effect of charged species on the PL emission energy. The results are shown in Figure 4.5(b). Both negative and positive point charges lead to a decrease in the energy contribution due to the increased Coulomb interaction. These data illustrate nicely that the effect of negative point charges is more pronounced than that of positive point charges. This is due to the larger effective mass of a hole with respect to an electron. With both negative and positive point charge, the attractive Coulomb interaction of the point charge with the counter charge outweighs the repulsion with the same charge. For a negative point charge, this effect is further enhanced by the increased mobility of electrons compared to holes. With regard to the work of Franz et al. in which the effect of donor-acceptor pairs on the PL properties of CdSe QWs were studied, simulations with two point charges were conducted as well.¹¹⁹ Their energy contributions were found to lie mainly in between the values of single point charges, indicated by the purple area in Figure 4.5(b). The calculations showed that the energies of the donor-acceptor pairs and especially their order in the energy diagram are highly sensitive to the exact positions and distances of the two inserted point charges and the diameter of the wire. This makes it difficult to directly assign experimental data to specific model scenarios. Especially for small diameters, the energies of different cases differ only slightly in a small size range.

In summary, those considerations showed how COMSOL can be readily used to perform simulations that can yield valuable insights in the evolution of the effective band gap of semiconductor nanostructures of specific shapes and under specific conditions. The

estimation of the effects of charges on the emission energy can help to elucidate the mechanisms behind the processes investigated in this work on the PL properties of CdSe NWs.

4.2.2 Photoluminescence of CdSe QWs

In order to efficiently investigate semiconductor nanostructures with low QYs, such as colloidal CdSe QWS, confocal spectroscopy is employed. Measurements were performed of single wires or bundles on glass or Si substrates. This method allows facile data acquisition and the ability to compare measurements of the same structure along the wire axis. This enables experiments in which the effects of different chemical environments on a single structure can be investigated, instead of having to take possible inhomogeneities in a sample into account when comparing measurements of different individual NCs.

The theoretical considerations in the previous section highlighted that the electronic confinement is a crucial aspect for the PL properties of semiconductor nanostructures. As such, for 7.5 nm thick CdSe QWs the excitons are confined (Exciton-Bohr radius of CdSe $r = 5.4$ nm)¹⁷⁶ and the emission wavelength is blue-shifted in respect to the emission of bulk material. A typical PL spectrum of a single CdSe QW or a QW bundle is shown in Figure 4.6(a). With these thin QWs, the formation of bundles in solution is common and it is not possible to determine from a PL scan alone whether the wires under investigation are present as a wire bundle or as a single structure. The emission wavelength of 663 nm (1.87 eV) is blue-shifted by 50 nm (130 meV) from the bulk emission of 713 nm (1.74 eV).¹¹⁶ Therefore, the emission energy lies in the range of energies for CdSe QWs of these dimensions reported by Myalitsin et al.¹¹⁶ Further, the blue-shift in the emission energy is in good agreement with the energy contribution due to quantization and Coulomb interaction estimated via COMSOL (see Figure 4.5). Yet, it has to be noted, that the emission energies of the CdSe QWs, analyzed in this work, vary in the range of 660 – 700 nm. The resulting range of energies, blue-shifted by 30 – 130 meV with respect to the bulk emission, corresponds well with the range of energy contributions correlated to charged species, as shown in the COMSOL calculations in Figure 4.5. In most experiments in this work, the observed emission energies were in fact lower than the expected energy of a neutral wire in the respective size range. This is a first indication that the PL of the CdSe QWs is influenced by excess charges that might be generated by the trapping of charge carriers in defect states. For the CdSe QWs examined in this work, no trap emission is observed at room temperature. In the literature, trap emission was observed for CdSe NCs with diameters of 2.0 – 2.2 nm.⁵² The absence of trap emission for CdSe QWs might indicate non-radiative recombination of trapped carriers.¹⁷⁷ For the

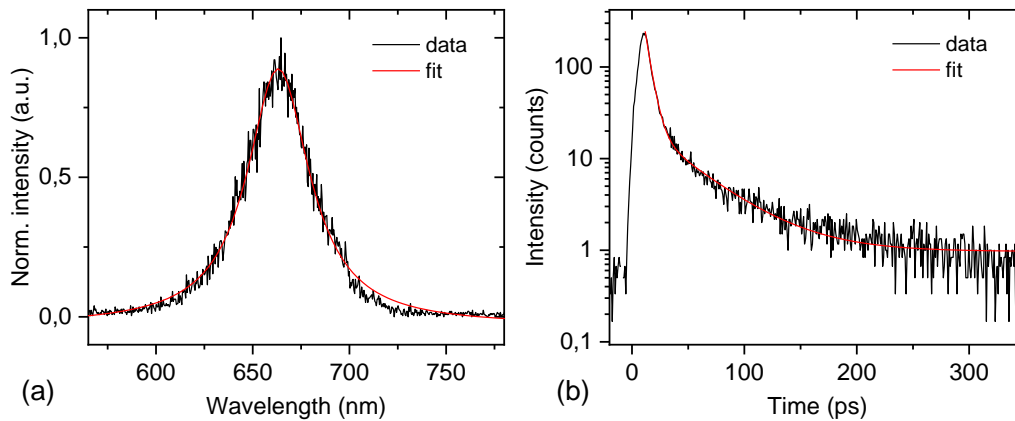


Figure 4.6: PL of CdSe QWs ($d = 7.5$ nm). (a) Emission spectrum fitted with a Lorentzian. (b) Decay curve fitted biexponentially. The data was recorded with a Streak camera (Excitation: $\lambda = 400$ nm, $f = 76$ MHz, pulse width = 150 fs, $P = 77$ kW/cm²).

CdSe QWs in this size range, however, the trap emission could still occur in the IR range, which is not within the detection range of the detectors used in this work.

The emission spectrum shown in Figure 4.6(a) was recorded with a Streak camera that allows for simultaneous examination of the photon emission energy and delay time. The corresponding PL decay curve is shown exemplarily in Figure 4.6(b). The average lifetime lies in a range of 10 – 30 ps (variations due to fitting parameters). These short lifetimes are consistent with findings in the literature.¹⁷⁷

These data are presented here primarily to classify the general optical properties of the QWs studied in this work. The data highlight that the PL properties are consistent with the properties of CdSe QWs described in the literature and are therefore a representative system.^{116,177} Measuring the short PL lifetime of the QWs requires an experimental system, which allows data acquisition with high transient resolution. The setups usually employed during this work for measuring the PL emission of the QWs are not suitable for measuring the decay curves of the CdSe QWs. Since the processes related to the effects of the chemical surroundings that were investigated in this work could be successfully elucidated without the analysis of the decay dynamics, the experiments described in the following sections focus on the PL intensity and wavelength.

4.2.3 Photoluminescence Properties in Oxygen

The effect of oxygen on the PL properties of semiconductor NCs has been widely studied throughout the last two decades. Various effects have been reported and several mechanisms of interactions have been proposed. In order to investigate the effect of oxygen on

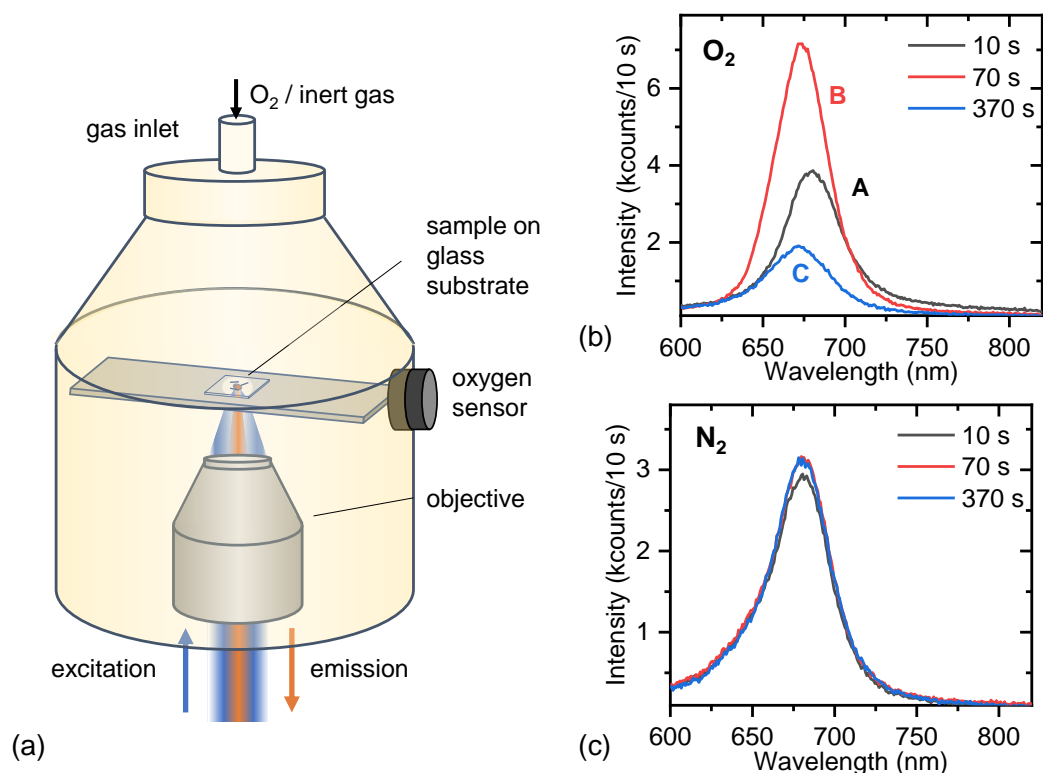


Figure 4.7: PL of CdSe QWs in controlled gaseous surroundings under continuous illumination. (a) Sketch of the setup for confocal measurements in different atmospheres. (b) Evolution of PL spectra in O_2 . The changes in PL intensity follow the scheme A (initial state) \rightarrow B (activated state) \rightarrow C (quenched state). (c) Comparative measurement in N_2 . Excitation: $\lambda = 470$ nm, $P = 56$ kW/cm², cw. Adapted from Kusterer et al.¹⁶⁶

the optical properties of CdSe QWs, confocal spectroscopy of wires on glass substrates was performed, while controlling the surrounding atmosphere by flushing the respective gas through a flow channel or a special gas-changing setup. This is illustrated in Figure 4.7(a). The work concerning the effects of oxygen is especially focused on photoinduced effects. Therefore changes in the optical properties during illumination like photobrightening and photodarkening are investigated.

Figure 4.7(b) shows the typical development of the PL emission spectrum of CdSe QWs in oxygen under continuous illumination. In the first phase, the PL intensity increases (A \rightarrow B) before photodarkening occurs with ongoing illumination (B \rightarrow C). This process is accompanied by a blue-shift in emission wavelength of 26 meV. A comparative measurement in nitrogen is shown in Figure 4.7(c). In nitrogen, no significant changes in PL intensity or emission wavelength are observed, demonstrating the necessity of oxygen for the photoinduced effects.

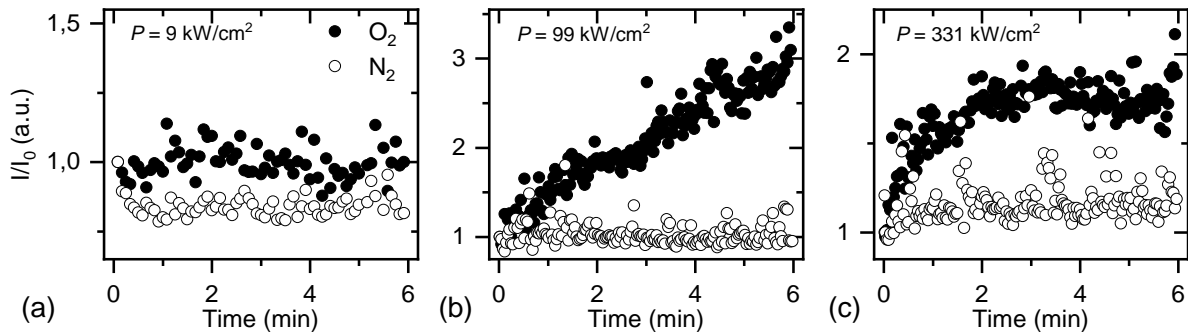


Figure 4.8: Evolution of the PL intensity of CdSe QWs in O_2 and N_2 at different excitation powers. The data points in the time traces depict the integrals of the PL spectra that were recorded as spectra series. (a) 9 kW/cm^2 , (b) 99 kW/cm^2 and (c) 331 kW/cm^2 . Excitation: $\lambda = 633 \text{ nm}$, cw. Adapted from Kusterer et al.¹⁶⁶

Since this process is photoinduced, it is not surprising that a dependence on the excitation power can be found. Figure 4.8 shows the development of the PL intensity (integral of the spectra) over time during continuous illumination in oxygen and inert gas atmosphere at different excitation powers. The data acquired at low excitation powers of 9 kW/cm^2 , depicted in Figure 4.8(a), show no significant changes of the PL intensity in oxygen atmosphere, while a small decrease of the intensity during the first minute of illumination is observed in nitrogen atmosphere. Figure 4.8(b) and (c) show the evolution of the PL intensity at higher excitation powers of 99 kW/cm^2 and 331 kW/cm^2 . In both cases PL enhancement is observed in oxygen atmosphere. While the PL intensity did not reach saturation during the measurement time at 99 kW/cm^2 , it reached saturation after already two minutes at 331 kW/cm^2 . The enhancement factors differ slightly in the range of 1.8 – 3. At both excitation powers the PL enhancement to this extent is only observed in oxygen atmospheres, while only minor effects are observed in nitrogen atmospheres. At 331 kW/cm^2 , the PL intensity increases by a factor of 1.1 during the first minute of illumination and some fluctuations of the intensity are observed during the whole measurement. These observations highlight that the photobrightening effect in oxygen only occurs when a certain power threshold is overcome. In addition, the data also show that the extent of the PL enhancement differs within a certain range, indicating inhomogeneities in the CdSe QW sample.

So far, the data showed that the PL enhancement is photoinduced and dependent on the oxygen in the atmosphere. For a better understanding of the process leading to the PL enhancement, the reversibility is an important factor as it can provide insights into the interaction of oxygen with the CdSe QWs.

Irreversible Photobrightening

In order to investigate the (ir)reversibility of the photobrightening, CdSe QWs are excited locally and illumination is stopped before the photodarkening phase is reached. Figure 4.9(a) shows the data of a spectra series of CdSe QWs in oxygen. The PL intensity increases and the wavelength shifts to the blue during illumination. The excitation is stopped twice for 30 s each. In both cases, the changes in PL intensity and wavelength remain when starting the illumination again and the process continues. These data show the irreversibility (upon illumination) of the photoactivation on a short time scale. In order to investigate this behavior on a longer time scale, PL scans of CdSe QWs before and after photoactivation are compared. Figure 4.9(b) shows the PL scan before the photobrightening experiments. The CdSe QWs were locally illuminated at the marked spots for 180 s and the illumination was stopped before the photodarkening phase was reached. The subsequent PL scans right after the illumination experiments and 20 h later in Figure 4.9(c,d) show that the respective regions are still in the activated state, since the locally increased PL intensity is clearly visible. These results show that the oxygen-induced photobrightening is permanent after stopping the illumination.

The data shown in Figure 4.9 also highlight another aspect concerning the PL properties of CdSe QWs. It was the focus of past investigations in different groups whether the PL of semiconductor quantum- and nanowires is governed by bound excitons or free charge carriers.^{117,121} The photoactivated regions in the PL scans in Figure 4.9(c,d) show locally enhanced emission. If the charge carrier dynamics were dominated by free charge carriers, the PL intensity would increase homogeneously along the wire axis during a photobrightening event. Therefore, the data affirm that CdSe QWs in this size regime exhibit bound excitons, which is in agreement with the literature.^{117,121} For QWs, the fixation of excitons along the wire axis might result from the formation of excitonic complexes that were investigated by Franz et al. via low-temperature spectroscopy.¹¹⁹ Dopants and alternating zincblende and wurzite segments along the wire axis can provide sites for locally bound excitonic complexes in QWs.^{119,178}

The results of the experiments in Figure 4.9 demonstrated the irreversibility of the oxygen-induced photobrightening in an unchanged oxygen atmosphere. Further, the (ir)reversibility when changing the atmosphere is probed. Figure 4.10(a) shows a PL scan of CdSe QWs in air. After local illumination of three spots in air or in O₂ atmosphere, the photoactivated regions can be identified by the enhanced intensity in the PL scan shown in Figure 4.10(b). After switching to N₂ atmosphere another PL scan is recorded, shown in Figure 4.10(c). In this scan, the photoactivated regions are still clearly visible. These data unambiguously demonstrate the irreversibility of the oxygen-induced photobrightening of CdSe QWs. At this point it has to be noted that reversible effects can also

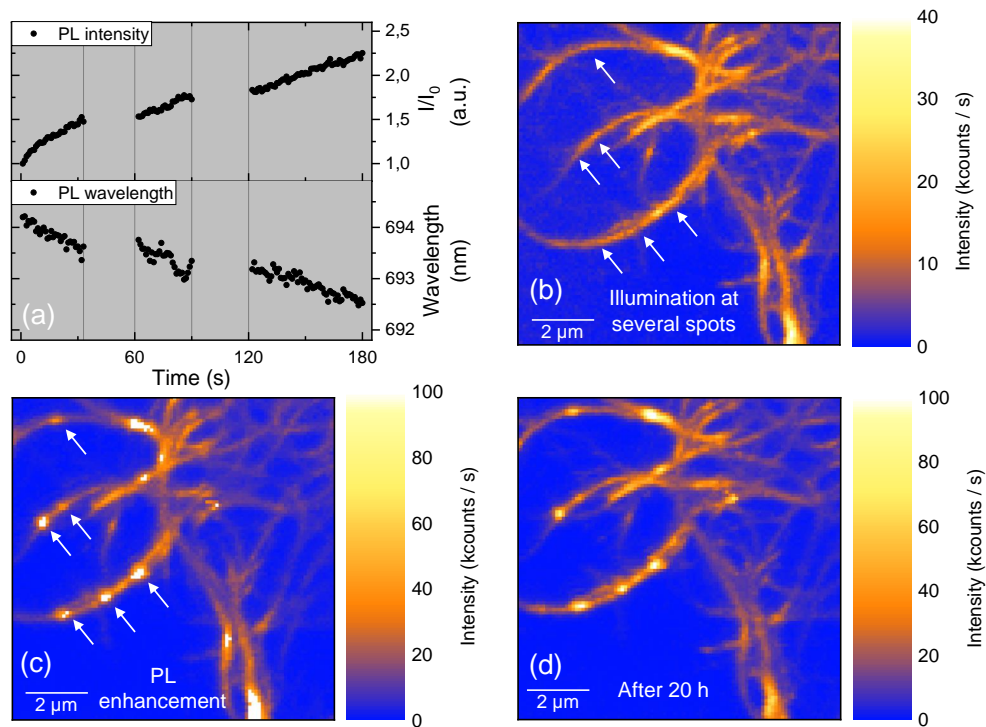


Figure 4.9: Irreversibility of oxygen-induced photobrightening of CdSe QWs when stopping the illumination. (a) Transient evolution of PL intensity and emission wavelength in oxygen, while the excitation is paused two times for 30 s ($\lambda = 633$ nm). (b)–(d) PL scans of CdSe QWs in oxygen atmosphere. (b) PL scan before local illumination at marked spots: $\lambda = 470$ nm, $P = 56$ kW/cm², cw, for 3 min. (c) PL scan after local illumination experiments. (d) PL scan 20 h after local illumination experiments. From Kusterer et al.¹⁶⁶

be observed by changing the atmosphere during illumination. This will be discussed in Section 4.2.3.

As a final experiment concerning the (ir)reversibility of the oxygen-induced effects discussed in this section, the atmosphere is switched during the photodarkening period that occurs after the PL enhancement upon further illumination. Similar to the experiments concerning the irreversibility of the PL enhancement, this investigation can yield insights about the nature of the interaction of oxygen with the QWs. Figure 4.11 shows the respective transient evolution of the PL intensity and wavelength for this experiment. Analogue to the data shown in Figure 4.7(b), the PL intensity follows the scheme $A \rightarrow B \rightarrow C$, while the emission wavelength shifts continuously to the blue within the first minutes of illumination. When changing the atmosphere during the photodarkening phase, a reversible blue-shift of the emission wavelength by 2 nm is observed. This will be discussed in detail in Section 4.2.3. However, the PL intensity remains in the quenched state when exchang-

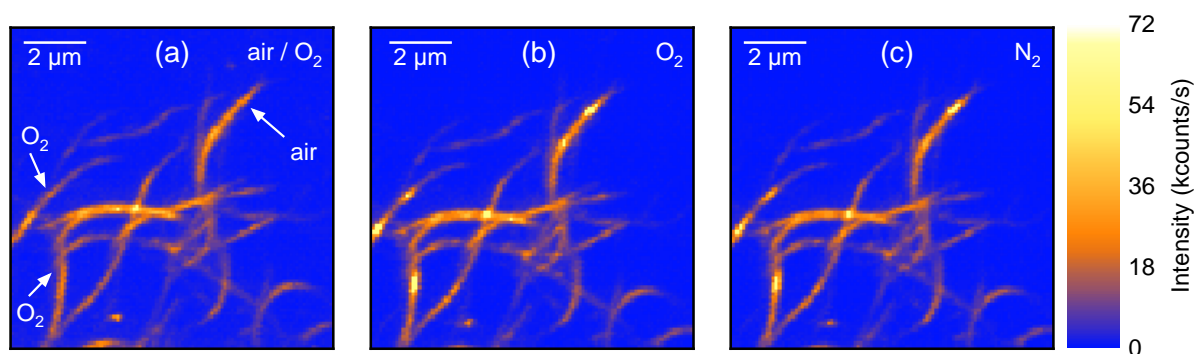
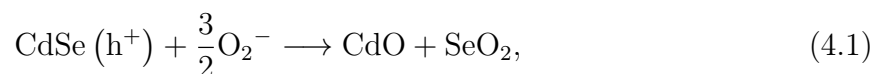


Figure 4.10: Irreversibility of oxygen-induced photobrightening of CdSe QWs when changing the atmosphere. (a) PL scan in air before local illumination in air or O₂ atmosphere at marked spots ($\lambda = 470$ nm, $P = 56$ kW/cm², cw, for 6 min). (b) PL scan in O₂ atmosphere after local illumination. (c) PL scan in N₂ atmosphere after local illumination.

ing the gases. Therefore, not only oxygen-induced photobrightening but also subsequent photodarkening can be explained as an irreversible process.

Mechanism of Irreversible Photobrightening of CdSe QWs The irreversibility of the oxygen-induced photobrightening shows that oxygen does not solely passivate surface traps or acts as electron scavenger, as described for QDs in the literature.^{19,20,91} Since the activation of the PL enhancement is permanent, a stronger interaction has to be accounted for. For CdSe NPs, photooxidation is already a well studied subject. Thermodynamically, the most favorable products are CdSeO₃ and CdO, as well as SeO₂.⁸⁰ The mechanism of photooxidation of CdSe NPs was investigated by Hines et al. and the reaction equation



summarizes the process. It was postulated that oxygen acts as electron scavenger at the surface, leaving the hole h^+ in the particle. The reduced oxygen species then reacts with the positively charged particle resulting in the production of CdO and SeO₂.⁷⁰

In most cases photooxidation is correlated with quenching of the PL intensity.^{63,69–72,74,75,87,88,179} However, PL enhancement due to photooxidation is also plausible. Via the reaction with oxygen, surface defects might get cured, similar to photoetching or inorganic shell growth, thus leading to an increase in PL efficiency. For our CdSe QWs the increased amount of Se, found by EDX spectroscopy and ICP-MS measurements (see Section 4.1.1), gives a strong indication that unpassivated Se ions are present at the surface. A correlation of the occurrence of photobrightening and Se-rich

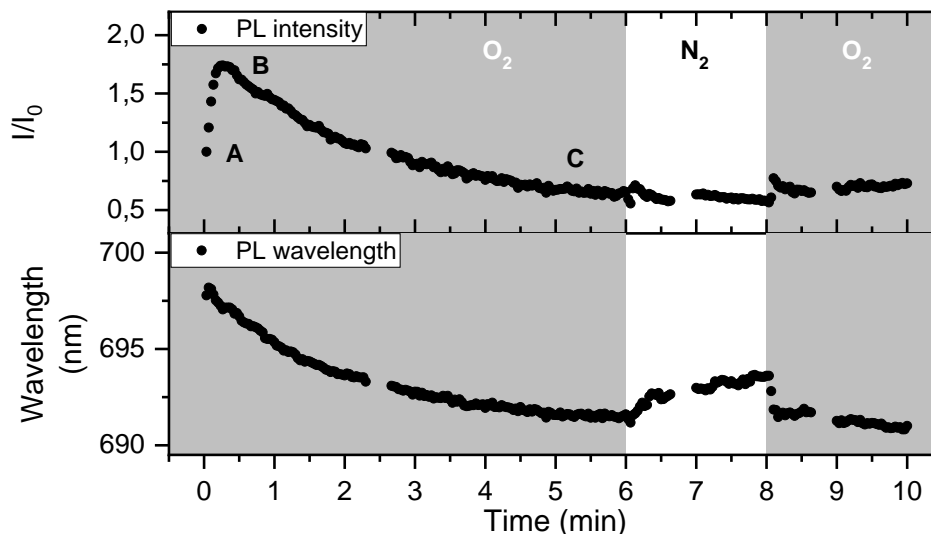


Figure 4.11: Irreversibility of oxygen-induced photodarkening of CdSe QWs. The PL intensity follows the scheme A (initial state), B (activated state) and C (photodarkening). The PL emission wavelength shifts continuously to the blue. In between minute six and eight, the gas is changed to nitrogen. The gaps at minute two, six and eight are due to an automatic correction of the position of the laser focus, in order to compensate for small variations due to the gas change. $\lambda = 633 \text{ nm}$, $P = 200 \text{ kW/cm}^2$, cw. Adapted from Kusterer et al.¹⁶⁶

surfaces was already reported for CdSe NPs.⁵³ Therefore, the findings presented so far, together with the current knowledge about NPs, allow for the proposal of the mechanism that is illustrated in Figure 4.12. The unpassivated Se ions at the surface exhibit excess negative charges. These present trapping sites for photoexcited holes. The remaining excess electrons inhibit radiative recombination by Auger recombination in the initial state A. In the course of illumination in an oxygen atmosphere, oxygen can act as an electron scavenger, removing the electrons from the wire. This leads to a reduction of Auger processes, resulting in the enhanced PL intensity in state B. The continuous blue-shift of the emission wavelength during illumination indicates that formation of oxides already occurs during the photobrightening phase (A \rightarrow B). Due to the excess of Se in the CdSe QWs, the formation of SeO_2 is most likely the most important process for the observed effects. SeO_2 formed at the surface can create an oxide layer or detach from the crystal and evaporate. For CdSe NPs, X-ray photoelectron spectroscopy (XPS) studies revealed a decrease of the Se: Cd ratio with proceeding photooxidation, indicating detachment of SeO_2 from the surface.^{80,81} Consequently, the model depicted in Figure 4.12 proposes that the detachment of SeO_2 , as well as other photooxidation processes such as the formation of CdO and CdSeO_3 and the decomposition of the organic ligands, eventually lead to photodarkening.

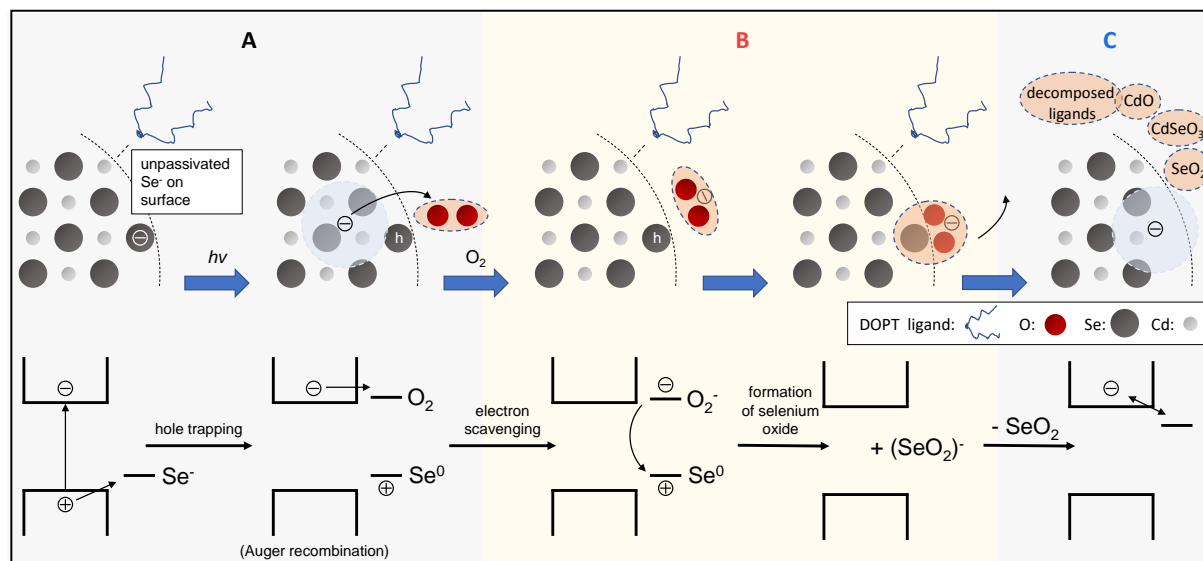


Figure 4.12: Scheme of the proposed mechanism of oxygen-induced photobrightening and photodarkening of CdSe QWs. A \rightarrow B: Inhibition of Auger recombination by electron scavenging leads to PL enhancement. B \rightarrow C: Detachment of SeO_2 and further decomposition by photooxidation leads to PL quenching. From Kusterer et al.¹⁶⁶

Exclusion of Further Mechanisms For the PL enhancement of CdSe NCs a lot of mechanisms have already been proposed in the literature. Further studies have been carried out to determine whether other mechanisms are involved in the effects observed in this work. Several investigations, especially concerning the PL enhancement due to photooxidation were performed with thin films of CdSe NPs.^{76,86–88,180} For example, the formation of SeO_2 at the particle surface, which then acts as ionization barrier was discussed.⁸⁶ Further, it was proposed that the formation of a CdO layer could enhance the coupling of CdSe NPs in thin films, thus leading to an enhancement of the PL intensity.⁸⁸ In order to investigate whether processes that only occur in ensembles play a role in the effects observed for CdSe QWs, measurements of single wires were conducted.

In this study, SEM measurements were conducted after performing the confocal photoexcitation experiments. In order to enable identification of single wires via SEM, larger wires with an average diameter of $d = 28$ nm were used. Figure 4.13(a) shows a scan of the reflected laser light of a CdSe NW on a substrate exhibiting markers. Especially with these larger wires, the use of reflection scans is well-suited for localizing individual structures. The results of a series of spectra, yielded by local illumination in air, are shown in Figure 4.13(b). The PL intensity increases and the PL wavelength shifts continuously to the blue. In this particular case the photodarkening phase did not start within the time span of the measurement. However, photodarkening was also observed

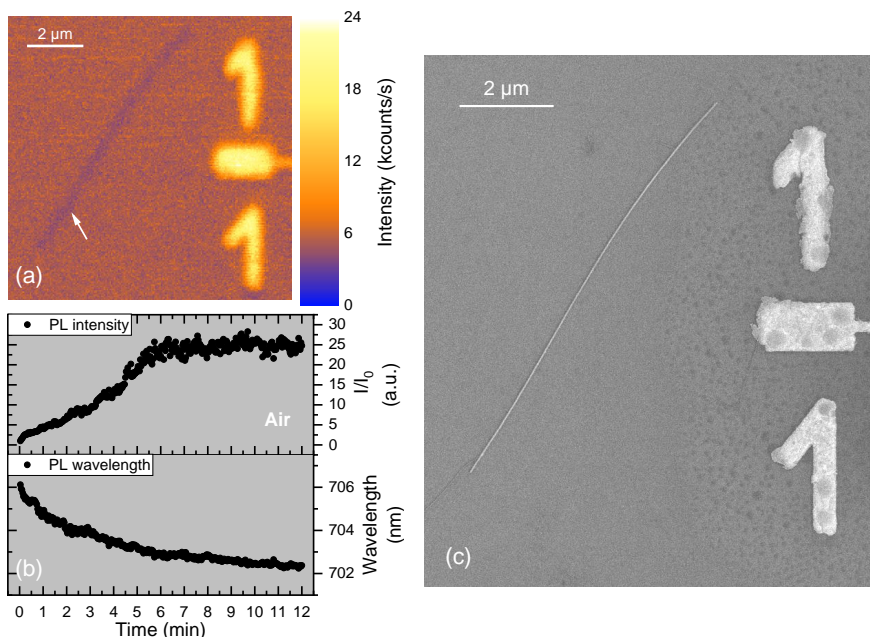


Figure 4.13: PL enhancement of a single CdSe NW ($d_{av.}$ of sample = 28 nm). (a) Reflection scan of a NW on a marked Si-substrate. (b) Transient evolution of PL intensity and wavelength during local illumination at the marked spot ($\lambda = 633$ nm, $P = 6400$ W/cm²). (c) SEM scan of the same NW, recorded after the PL measurement to ensure the presence of a single wire. From Kusterer et al.¹⁶⁶

for higher excitation powers. To verify that the excited wire was a single wire and not a bundle of wires, a SEM scan of the same spot was recorded subsequent to the confocal measurements. Figure 4.13(c) shows the SEM scan, in which a single structure can be identified.

The observation of photobrightening of a single wire shows that effects of photooxidation which were described for thin particle films, like coupling and charge transfer, are not decisive for the observations made for CdSe QWs.

Various other mechanisms for photobrightening, which are not related to O₂ are also described in the literature (see Section 2.1.2). However, the observed dependence on oxygen shows the effect of oxygen to be the dominant effect. One feature that is still worth mentioning here is the role of the organic ligands for photobrightening. For CdSe NPs it was suggested that TOPO–Se complexes might be formed during illumination. Since this would lead to a passivation of surface traps it could be in correlation with the enhancement of the PL intensity.⁶³ For CdSe QWs, however, the investigation of the organic ligands by IR spectroscopy suggests that the majority of the ligands after three purification cycles is given by the phosphinic acid as X-type ligand. According to Morris-Cohen et al.¹⁷² and the data presented in Section 4.1.1, the number of L-type

ligands like TOPO decreases with each step of purification. If the presence of TOPO was decisive for the photobrightening effect, a correlation of PL enhancement with the number of purification steps would be expected. Yet, no dependence of the photoinduced PL enhancement on the level of purification was observed for CdSe QWs (see Figure 8.1 in Appendix).

In summary, the previous section describes the development of the PL properties of CdSe QWs when illuminating in oxygen containing atmospheres. By comparison to measurements in inert gas atmospheres and changing the gases after illumination in oxygen, the nature of the oxygen-induced photobrightening and subsequent photodarkening was elucidated. The evaluation of the spectroscopic data in combination with the knowledge about the CdSe QWs, gained by the analysis of the surface and composition, allowed for the proposal of a mechanism. As an excess of Se was found in the analysis of CdSe QWs, the PL enhancement is assigned to passivation of Se surface sites by oxygen molecules. The irreversibility of the photobrightening suggests photoinduced formation of SeO_2 at the surface. The subsequent photodarkening is assigned to degradation of the particle due to further photooxidation, which is indicated by the blue-shift of the emission wavelength. So far, the focus has been on the irreversible photoinduced effects observed when CdSe QWs are illuminated in oxygen-containing atmospheres. The reversible effects of oxygen on PL properties will be discussed in the following section.

Reversible Effects

In addition to the irreversible oxygen-induced photobrightening of CdSe QWs, reversible effects are observed when changing the gas atmosphere during illumination. Figure 4.14(a) shows representative results of a series of spectra, recorded under continuous illumination while changing the atmosphere between oxygen and inert gas in intervals of two minutes. The graphs show the relative PL intensity and the emission wavelength that were determined by fitting the spectra with Lorentz functions. Four chosen spectra (marked 1–4) of the series are shown in Figure 4.14(b–e). At the start of the measurement in oxygen only one Lorentzian is sufficient to represent the data, as shown in Figure 4.14(b). The PL intensity increases continuously during the first two minutes while the emission wavelength shifts to the blue. When changing to inert gas, a second peak emerges at approximately 655 nm (see Figure 4.14(c)). The intensity of this peak rises abruptly after the gas change and stays constant until the gas is changed back to oxygen. At that point, the intensity of the second peak is reduced drastically. The sudden reversible addition of the blue-shifted peak also leads to a reversible increase in the overall PL intensity in inert gas atmosphere. After changing the atmosphere back to oxygen at 240 s the photobrightening resumes and the PL intensity gets further enhanced, as shown in Figure 4.14(d). Figure 4.14(e)

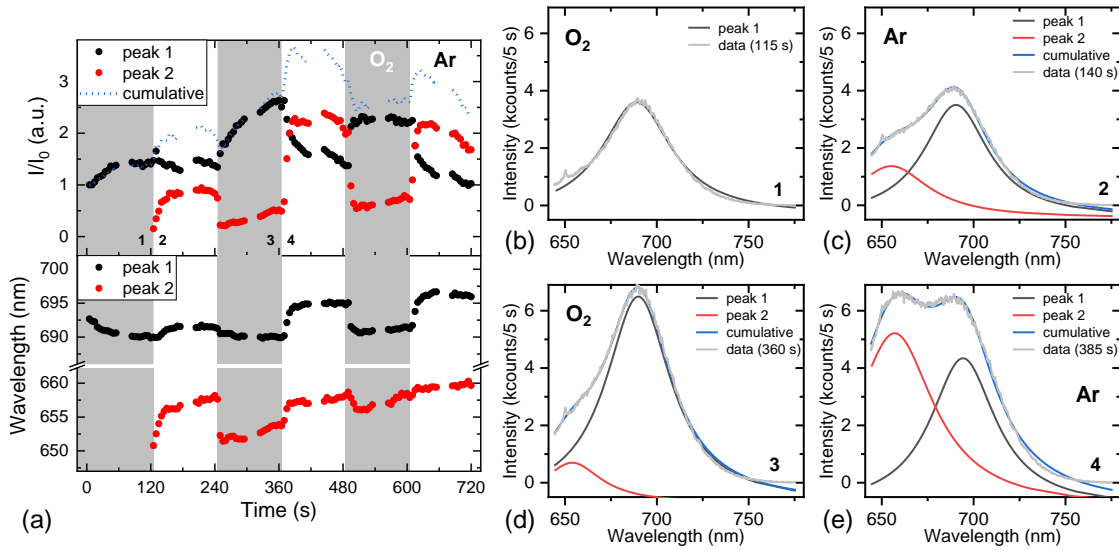


Figure 4.14: Reversible effects of oxygen on the PL properties of CdSe QWs. (a) Evolution of PL intensity and emission wavelength, while switching the gaseous atmosphere between oxygen and inert gas under continuous illumination ($\lambda = 633$ nm, $P = 44$ kW/cm², cw). (b–e) Corresponding PL spectra at the spots (1–4), marked in the intensity time trace in. The gaps in the time trace in (a) result from an automatic correction of the height of the laser focus, in order to compensate for small variations due to the gas changes. From Kusterer et al.¹⁶⁶

shows the spectrum after changing back to inert gas after 385 s of illumination, at which point the second blue-shifted peak emerges again and now even exceeds the intensity of the original peak.

First of all, the data depicted in Figure 4.14 show again that the oxygen-induced photobrightening is irreversible. When changing the gaseous atmosphere back to oxygen after 240 s, the enhanced PL intensity, as well as the blue-shifted emission wavelength do not fall back on the level of the start of the illumination, but to the level prior to the interval of inert gas atmosphere. This supports the assignment of the photobrightening process to an irreversible process. As discussed in Section 4.2.3, the interaction of oxygen with the surface has to be stronger than weak physisorption.

On the other hand, reversible effects are also observed when changing the atmosphere. A second peak emerges reversibly in inert gas atmosphere and is blue-shifted by 100 meV with respect to the initial peak. At the same time the initial peak exhibits at red-shift by 10 meV. These observations are in good agreement with spectroscopic features of charged biexcitons reported for NPs.^{36–43} The existence of charged biexcitons when illuminating in inert gas atmospheres at high excitation powers is plausible. The absence of oxygen as electron scavenger results in an excess of negative charge carriers in the wire.

Subsequent excitation then fills higher energy states. As a result, the blue-shifted peak can be attributed to $1P_e-1P_{3/2}$ or $1P_e-1S_{3/2}$ radiative recombination. On the other hand, the red-shift of the initial peak in argon aligns well with the concept of $1S$ electrons being energetically stabilized due to Coulomb interactions in negatively charged particles.

With 100 meV, the energy separation observed between peak 1 and peak 2 is slightly less than the energy transition shift of 120–200 meV between the second and first excited state for CdSe QWs in this diameter range, as reported by Giblin et al.¹¹⁷ The energy shift reported in the literature refers to the absorption level. The consideration of Coulomb interactions in multiexcitons can explain the lower values observed here. For CdSe QDs, similar discrepancies in the shifts for the P–P emission were observed.^{37,42} In addition to considering the influence of charges on the energy levels, photoselection of larger particles within a sample was taken into account. Both arguments can apply for the CdSe QWs investigated in this work.

For CdSe NPs and for QDs, reversible oxygen-induced processes were previously attributed to oxygen acting as an electron acceptor or electron scavenger.^{18–20} This assignment is in good agreement with the observations made for the CdSe QWs in Figure 4.14, since it explains both the reversibility and the spectroscopic features when the gas is changed.

Another aspect emerging from the data shown in Figure 4.14(a) is the observation of a dependence of the blue-shifted emission peak (peak 2) on the photobrightening in oxygen. After the intervals in oxygen in which photobrightening occurs, the intensity of peak 2 is also enhanced. As discussed in Section 4.2.3 the irreversible changes of the PL are assigned to irreversible photooxidation at the QW surface. The enhancement of the intensity of peak 2 after the photobrightening indicates that oxides like SeO_2 , formed at the surface, get flushed away by the inert gas at the gas change. The removal of SeO_2 could lead to a release of electrons into the QW, thus enhancing the multiexcitonic emission in inert gas atmospheres.

Excitation-Power Dependence Further spectroscopic evidence for the assignment of the concurring recombination processes can be gained by investigating the excitation-power dependence. Figure 4.15(a) shows the evolution of the intensities of peak 1 and peak 2 in oxygen and in inert gas atmosphere at excitation powers that are tenfold higher than for the data shown in Figure 4.14. Due to the higher excitation power, a second blue-shifted peak can not only be identified in inert gas atmosphere, but also in oxygen, albeit at a much lower intensity. In oxygen, both peaks follow the scheme A (initial state) \rightarrow B (photoactivated state) \rightarrow C (photodarkening), as already discussed in Section 4.2.3. In inert gas atmosphere, the intensity of peak 1 rapidly decreases, while the intensity of

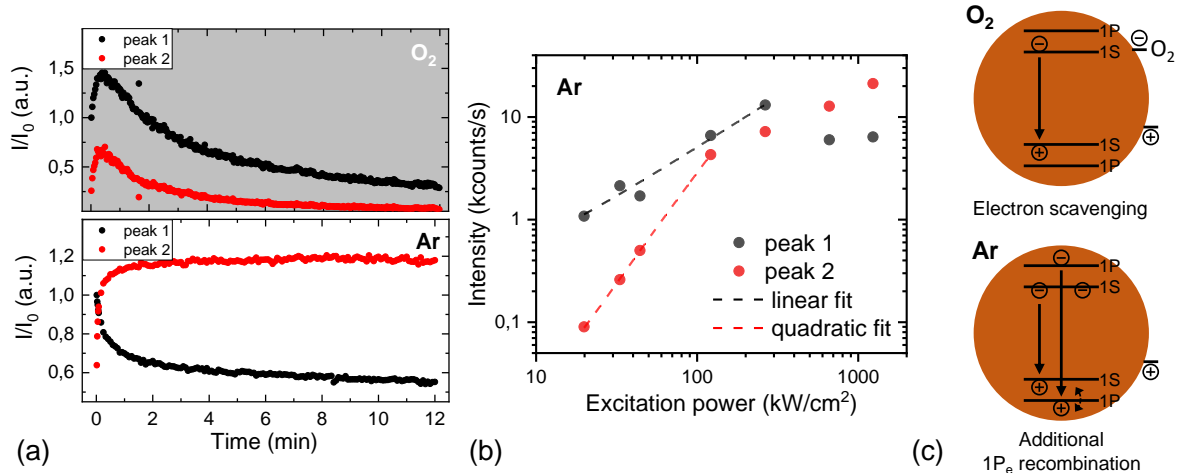


Figure 4.15: Excitation-power dependency of multiexcitonic emission of CdSe QWs. (a) PL intensity time trace in oxygen and in inert gas atmosphere at high excitation powers ($\lambda = 633$ nm, $P = 660$ kW/cm^2 , cw). (b) Intensities of peak 1 and peak 2 in inert gas atmosphere relative to the excitation power. (c) Sketches of the preferred recombination states in oxygen and inert gas atmosphere. From Kusterer et al.¹⁶⁶

peak 2 simultaneously increases and becomes the dominant emission in the spectrum. The intensities of both peaks in inert gas atmosphere are plotted versus the excitation power in Figure 4.15(b). For the initial peak 1, the data can be fitted with a linear fit function, whereas the data of peak 2 follows a quadratic trend. This relation indicates that peak 1 originates from single excitons, whereas peak 2 originates from multiexcitons. To excite one multiexciton, at least two excitation events are required. Thus, the excitation probability increases quadratically with the excitation power. Therefore, the data support the assignment of peak 1 and peak 2 to S-S and P-P/P-S recombination, respectively.^{36,38,39} The scheme in Figure 4.15(c) illustrates the dominant recombination state in the respective atmosphere. In oxygen, electron scavenging neutralizes the negatively charged QW yielding neutral S-S recombination. In inert gas atmosphere, an excess of electrons leads to the occupation of higher states, while the electrons in the 1S states exhibit slightly lower energies due to Coulomb interaction.

A more detailed scheme for the recombination mechanism in dependence of the atmosphere is given in Figure 4.16. The particle gets ionized by hole trapping or autoionization. While this process can also occur with single excitons, exciting with high powers likely results in the formation of biexcitons, thus increasing the probability of autoionization. Either way a negatively charged species X^- is obtained. In the absence of oxygen, further excitation leads to occupation of higher excitation states, followed by 1S and 1P recombination. In the presence of oxygen, however, excess electrons are removed from the 1S

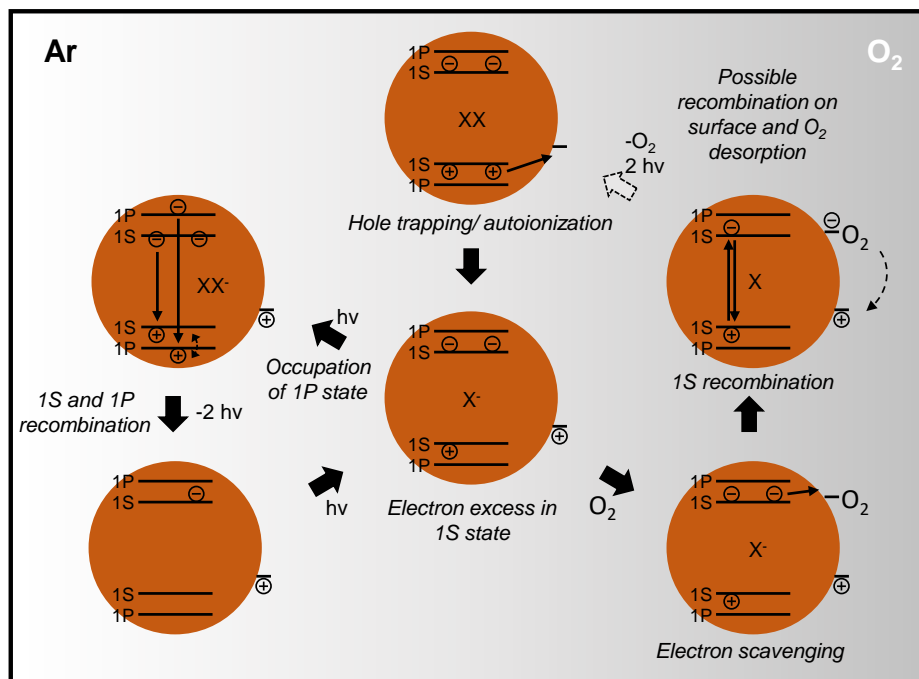


Figure 4.16: Scheme for the mechanism of the development of multiexcitonic emission at high excitation powers in inert gas (left), compared to the emission of neutral excitons in oxygen (right). From Kusterer et al.¹⁶⁶

state, giving way to recombination of neutral excitons. Electrons accepted by oxygen might recombine non-radiatively with trapped holes at the surface, allowing the oxygen molecules to detach from the particle, as proposed for CdSe NCs by Koberling et al.¹⁸

In conclusion, the gas-exchange experiments during continuous illumination reveal a reversible effect of oxygen on the PL of CdSe QWs. The reversible changes in the PL spectra are assigned to electron scavenging. By analyzing of the spectroscopic features of the PL variations upon gas change, the presence of charged biexcitons in inert gases was determined. In the discussion of the data for the CdSe QWs, frequent references and comparisons were made with findings and principles known from investigations of spherical CdSe NCs, as documented in the existing literature. To depict some of the principles outlined in the literature about CdSe QDs and to enable a direct comparison, a few experiments with CdSe QDs will be briefly discussed in the following section.

Comparison to CdSe Dots

Figure 4.17 shows time traces of PL spectra of CdSe NP thin films under continuous illumination. In Figure 4.17(a) illumination is started in inert gas atmosphere, whereas in Figure 4.17(b) illumination is started in oxygen atmosphere. Significant enhancement of the PL intensity is observed in the first minutes of illumination until the PL intensity

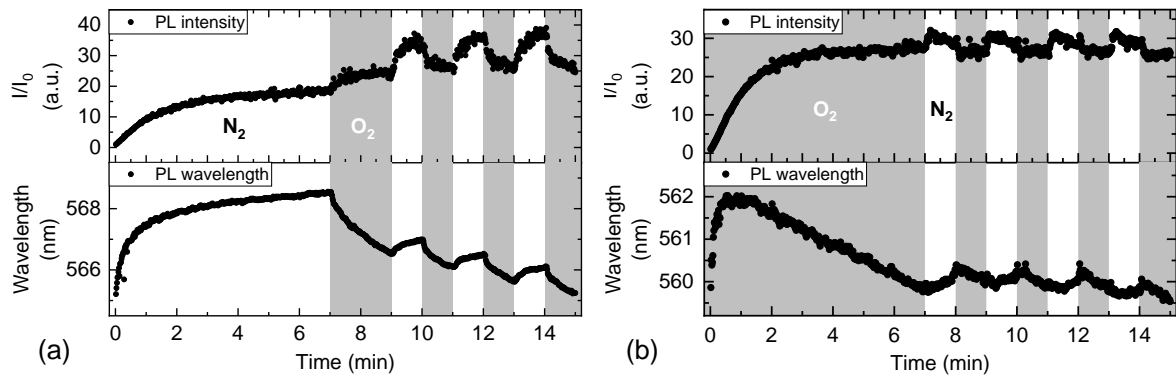


Figure 4.17: Time traces of series of PL spectra of CdSe NP thin films ($d_{\text{particle}} = 4.4$ nm, $\lambda = 405$ nm, $P = 10.8$ kW/cm²). (a) Illumination is started in a nitrogen atmosphere. (b) Illumination is started in an oxygen atmosphere.

saturates. When switching the gas atmosphere to oxygen after first illuminating in inert gas, as shown in Figure 4.17(a), the PL intensity experiences further enhancement. In both atmospheres the PL wavelength shifts slightly to the red in the first minutes of illumination. Upon further illumination, the PL wavelength saturates in inert gas but shifts to the blue in oxygen. In the second phase of the experiment, the gases were switched between inert gas and oxygen, revealing a reversible enhancement of the PL intensity in inert gas atmosphere. The change of gases further reveals the irreversibility of the first PL enhancement events in both atmospheres upon changing the surrounding medium. This accounts especially for the blue-shift of the emission wavelength which is observed when illuminating in an oxygen atmosphere.

Several effects which were described in the literature for CdSe NC thin films are observable in these measurements. Since photoinduced PL enhancement is observed regardless of the atmosphere, processes like ligand rearrangement,⁶³ or electron migration⁶² can be accounted for. In the literature, the red-shift of the emission wavelength during the photobrightening is explained with the Stark effect,⁶² whereas the blue-shift observed upon illumination in oxygen can be attributed to increased confinement due to photooxidation-induced shrinking of the particles.^{63,73} In agreement with findings in the literature, the PL enhancement is promoted in the presence of oxygen.⁵³ However, the effect of oxygen on the PL of NCs is less pronounced than for QWs. This suggests that the spherical NCs examined in this experiment exhibit fewer unpassivated Se sites on the surface. This would also be typical, since most colloidal spherical II-VI NPs exhibit metal-rich surfaces.^{50,164} Regarding the large atmosphere-independent PL enhancement, the data are in good agreement with the electron migration mechanism proposed by Tice et al.⁶² This shows that, for these CdSe NPs, electron trapping is dominant, while for the Se-rich CdSe QWs hole trapping prevails. As far as the reversible effects are concerned, these measurements show

the same behavior, as reported for CdSe NCs embedded in ZnS by Koberling et al., since the PL intensity gets quenched in oxygen atmospheres.¹⁸ Recent reports²⁰ of the opposite observation on bare CdSe NCs highlight the dependence of the observed effect on the respective characteristics of the system.

4.2.4 Raman Properties of CdSe QWs

When exciting CdSe QWs above the band gap, not only the fluorescence, but also the resonant Raman spectra can be obtained. In the following sections, effects of oxygen on the Raman spectra will be discussed.

Raman Modes During Oxygen-Induced Photobrightening

Figure 4.18(a) shows the evolution of the high energy region of the PL peak of CdSe QWs, when illuminating with $\lambda = 633$ nm in air. This region exhibits the 1LO and 2LO phonon peaks at $\nu(1LO) = 208$ cm^{-1} and $\nu(2LO) = 416$ cm^{-1} , each with a respective LFS. During illumination in air, the PL intensity rises for the first 140 s and then gradually decreases, according to the before mentioned scheme of A(initial state) \rightarrow B(activated state) \rightarrow C(quenched state). To analyze changes in the Raman peaks, the PL background is subtracted and the Raman peaks of the 1LO and the 1LFS are each fitted with a Lorentzian. The resulting fit functions are shown in Figure 4.18(b). The most distinctive change in the spectrum is the shift of the LFS to lower wavenumbers in the phase of photobrightening. In the subsequent photodarkening phase, the intensities of both LO and LFS peak decrease and the LFS shifts back to higher wavenumbers. The evolution of the shift of the LFS, together with the evolution of the PL intensity (value at 500 cm^{-1}) is shown in Figure 4.18(c). Despite some fluctuations of the values for the LFS frequency the described trend is clearly visible.

The observed evolution of the LFS is only observed when illuminating in air or oxygen atmosphere. In inert gas atmospheres, the position and intensity of the Raman peaks stay constant. This suggests a direct correlation of the observations for the Raman modes with the processes involved in the irreversible oxygen-induced photobrightening that were discussed in Section 4.2.3.

The LFS of the LO phonon mode is assigned to vibrations at the surface,¹⁰⁶ or to vibrations which are at least more widely distributed than the LO phonon mode.⁹⁹ Correlations of its frequency with the dielectricity of the surrounding medium, as well as with charges are discussed in the literature.^{97,98,108} Since the oxygen-induced photobrightening is a surface related effect, it is consistent that the LFS is affected more than the LO phonon

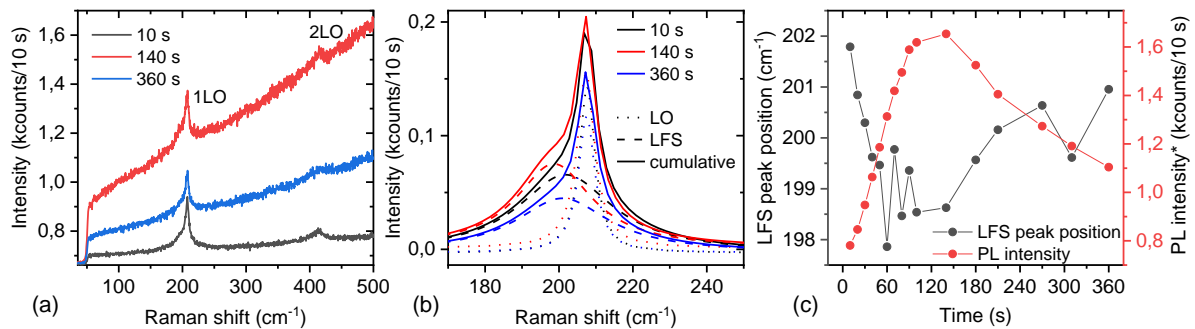


Figure 4.18: Raman spectra of CdSe QWs under continuous illumination in air ($\lambda = 633$ nm, $P = 419$ kW/cm²). (a) Extract of the data showing the evolution of the PL background and the Raman peaks. (b) Lorentz fit functions for the 1LO Raman peak and its LFS. (c) Evolution of the LFS peak position and the PL intensity (the intensity is given by the values at 500 cm⁻¹ in (a)).

mode by this process. Two plausible reasons for the shift of the LFS will be discussed in the following.

First, the dielectricity of the surrounding of the QW might be increased by the formation of oxides, such as SeO₂, yielding a core-shell like structure. A shift of the LFS or SO phonon mode frequency to lower wavenumbers due to an increased dielectricity of the surrounding medium is reported and discussed in the literature.^{97,108} The observed reversal of the shift of the LFS, after reaching a turning point is also consistent with the model for the oxygen-induced processes, proposed in Section 4.2.3. Both the decrease of the PL intensity, as well as the reversal of the LFS shift may be due to the detachment of oxides that have formed on the surface. In addition, the model for the correlation of the LFS frequency with the dielectricity of the surrounding medium can be extended with the effect of dynamic surface charges, as proposed by Liu et al. According to that model the LFS frequency is decreased at higher surrounding dielectricities and/or decreased by the presence of dynamic surface charges.¹⁰⁸ Following the model for the oxygen-induced photobrightening proposed in Section 4.2.3, negative charges that are first delocalized over a large area of the crystal, get fixated at the surface during continuous illumination in oxygen atmospheres. This correlation would also explain the decrease of the LFS frequency and its subsequent increase during continuous illumination in oxygen atmospheres. The combination of both, changes in the surrounding dielectric environment, as well as changes of the dynamic surface charge is also plausible.

In order to conclude the investigation of the effects of oxygen on the Raman spectra of CdSe QWs, the reversible effects are examined in a similar way to the PL studies by changing the gases during continuous illumination.

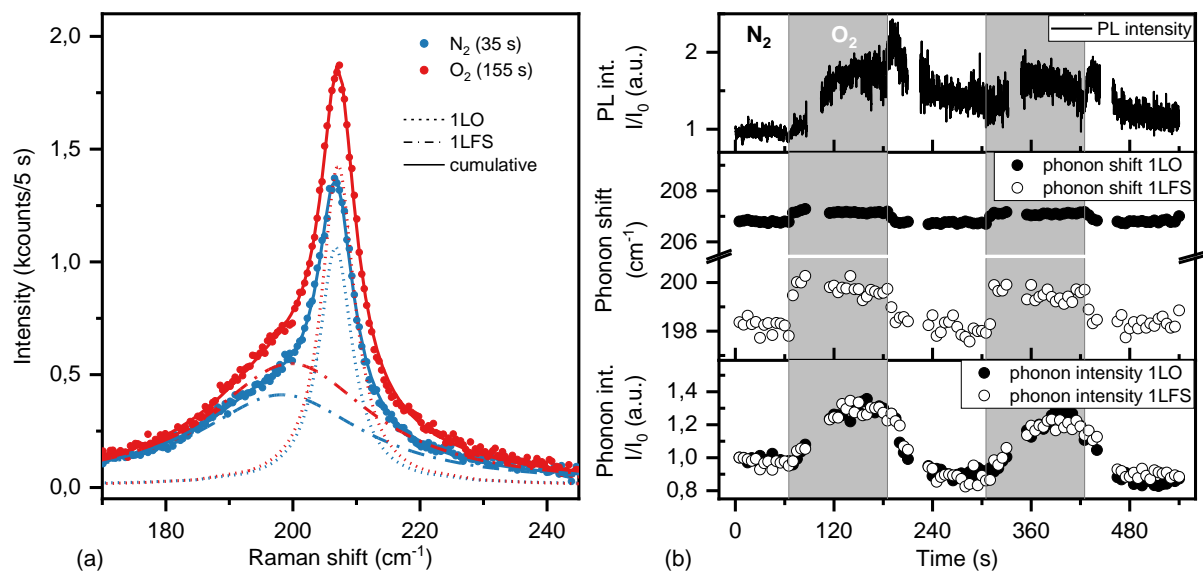


Figure 4.19: Raman spectra of CdSe QWs under continuous illumination in changing atmospheres $\lambda = 633$ nm, $P = 110$ kW/cm². (a) Background subtracted spectra in N₂ and in O₂ atmosphere, showing the 1LO phonon mode and the LFS. The peaks are fitted with Lorentzians. (b) Evolution of the PL intensity and the frequency and intensity of the 1LO and 1LFS peak with changing gas atmospheres. Adapted from Kusterer et al.¹⁶⁶

Reversible Effects of Oxygen

Figure 4.19(a) shows the 1LO optical phonon and its LFS of CdSe QWs in nitrogen and in oxygen atmosphere. Each peak is fitted with a Lorentzian. The comparison of the data in both atmospheres shows that the peak intensities of both LO phonon and LFS are reduced in nitrogen. Further, small shifts of the peak frequencies are observed, which can be seen more clearly in Figure 4.19(b). Figure 4.19(b) shows the evolution of PL intensity and the Raman peak characteristics, obtained by fitting the Raman spectra, during fast exchange of the gaseous surrounding between oxygen and nitrogen. This data representation reveals reversible effects of the atmosphere on the Raman peaks. At the change from nitrogen to oxygen atmosphere, the frequencies of 1LO phonon mode and 1LFS shift within seconds to higher wavenumbers. The 1LO phonon mode frequency shifts from 206.8 cm⁻¹ in nitrogen to 207.2 cm⁻¹ in oxygen, and the LFS shifts from 198 cm⁻¹ in nitrogen to 200 cm⁻¹ in oxygen. Simultaneously, the intensities of both peaks are enhanced. Both frequency shift and enhancement of intensity are reversed as the gas is exchanged back to nitrogen. During the periods of illumination in oxygen, the small gradual shift to lower wavenumbers that was discussed in the previous section is also observed, but the reversible effects are dominant in this measurement.

For ZnO NPs it was reported that the presence of free charge carriers shifts the Raman frequencies to lower wavenumbers by screening of the ion-ion interaction in the NC atom lattice.¹⁰⁵ As discussed previously (Section 2.1.2) reversible features of excess negative charges were observed for the PL properties of CdSe QWs in inert gas atmosphere. The combination of the reports in literature¹⁰⁵ with the interpretation of the reversible effects concerning the PL spectra are strong indicators that the reversible features in the Raman spectra of CdSe QWs are due to the presence of excess negative charge carriers in inert gas atmosphere and their removal in oxygen atmosphere. Interestingly, the shift of the peak position at the gas change is more enhanced for the LFS than for the LO phonon mode. In the literature, a correlation of the LFS with the dielectric surrounding,⁹⁷ surface charges⁹⁸ and resonant excitation of higher states⁹⁹ are discussed.

The notable increase in the reliance of the LFS (compared to the LO phonon mode) on atmospheric conditions, as depicted in Figure 4.19, indicates a substantial correlation with the presence of free charge carriers. With respect to the reports about a dependence of the LFS on the excitation of higher states,⁹⁹ the observations might also be correlated with the observation of enhanced radiative emission of $1P_e-1P_{3/2}$ and/or $1P_e-1S_{3/2}$ transitions at high excitation powers in inert gas atmospheres. However, Lin et al. only reported changes of the LFS.⁹⁹ In this work, analogue changes of the LO frequency are observed, suggesting a dominant correlation of the Raman peaks with the presence of free charge carriers. Another distinct observation is the reversible enhancement of the intensities of the Raman peaks in oxygen. For ZnO particles it was reported that the presence of excess charge carriers did not only affect the frequencies, but also the intensities (integrals) of the Raman peaks.¹⁰⁵ The presence of free charge carriers might lead to a reduction of the EPC strength, resulting in reduced intensities of Raman signals. Another result of reduced EPC can be a reduced 1LO/2LO intensity ratio.^{102,105} However, in this experiment, no change in the ratio of the 1LO and 2LO peaks was observed. If there are no other processes responsible for the intensity changes, this might indicate that the LO overtones do not originate from a "true" resonant Raman process, but a cascade process. In a "true" resonant Raman process, the LO phonons are generated in a single step via virtual states, while in a cascade process, the LO phonons are generated in several consecutive steps during the relaxation of hot charge carriers to the bandedge. However, these hypotheses are not yet conclusively clarified in the literature.¹⁰⁵

In conclusion, the reversible atmosphere dependent changes in the Raman spectra suggest a correlation of the Raman peak frequencies and intensities with the presence of excess charge carriers. Concurrently, the correlation of the frequency of the LFS with the evolution of the PL intensity during continuous illumination in an oxygen-containing atmosphere, highlights the photoinduced processes at the QW surface. Both experimental

analyses depicting the evolution of the Raman spectra in this study underscore the conclusions drawn from the examination of the PL properties. The concurrent exploration of Raman and PL properties highlights the capability to elucidate the character of surface-associated processes and recombination patterns, as well as to pinpoint the factors that impact the optical characteristics of semiconductor nanomaterials on a broader scale.

4.2.5 Effects of Dopants and Ligands on the Photoluminescence of CdSe QWs

In order to investigate photoinduced effects on the PL properties of CdSe QWs by different chemical species, experiments in flow-channels have been conducted. A sketch of the experimental setup for these measurements is depicted in Figure 4.20(a). Analogous to the experiments in the gas-flow setup, the QWs are excited through a glass substrate, on which they are fixed, while the surrounding medium can be exchanged. In addition to exchanging the gaseous surrounding of the wires, this method also allows for the investigation of the effects of liquids and solutions. However, due to the swell-behavior of the flow-channel material poly-(dimethylsiloxan) (PDMS) at contact with unpolar organic solvents, the experiments were restricted to aqueous solutions.

Photoluminescence in Aqueous Solutions

Figure 4.20(b) shows the evolution of the emission spectra of individual CdSe QWs or QW bundles on a glass substrate, while flushing the flow-channel with water. Photoinduced PL enhancement is observed and the evolution of the spectra is similar to the evolution observed in air or in oxygen. This process is discussed in detail in Section 4.2.3. The observation of photobrightening in water, with a similar evolution of the spectra as in oxygen, suggests that the underlying process is the same. Similar observations for CdSe QWs, covered with liquid polyethylene glycol (PEG)200, showed that the oxygen which is diluted in the surrounding matrix is sufficient for the observation of the photoinduced effects (see Appendix Figure 8.2). In order to be able to investigate solely the effects of additives in aqueous solutions, those experiments were conducted at significantly lower excitation powers at which the processes that are referred to oxygen are only marginally pronounced and occur on a slower time scale. For example, Figure 4.20(c) shows a PL intensity time trace recorded at a significantly lower excitation power, at which the PL intensity stays constant during the measured time, until the injected additives reach the sample. In this case, an aqueous methyl viologen dichloride (MV) solution ($c = 36 \mu\text{M}$) was injected. MV is known to efficiently quench the PL of semiconductor nanostructures via photoinduced electron transfer.^{181–183} This is also observed in Figure 4.20(c), as the

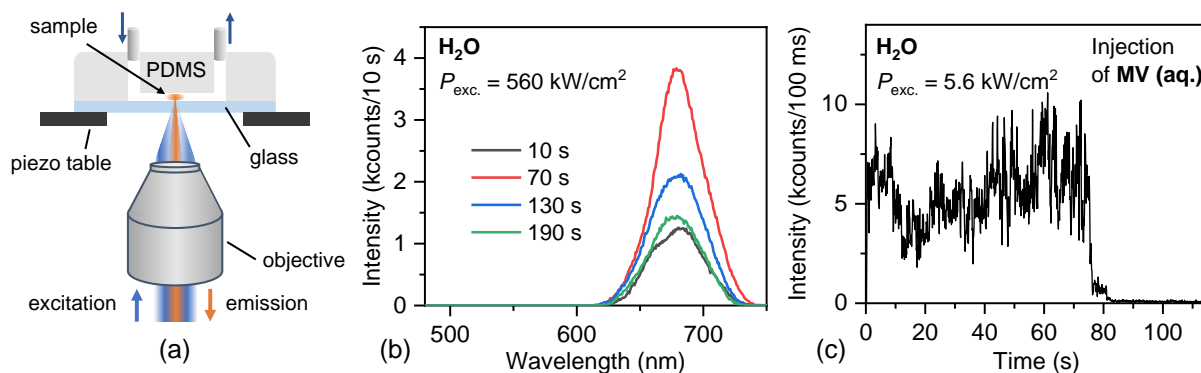


Figure 4.20: Evolution of the PL of CdSe QWs in aqueous solutions. (a) Sketch of experimental setup for measurements in PDMS flow-channels. (b) Evolution of the spectra in H_2O at $P = 560 \text{ kW/cm}^2$. (c) PL intensity time trace in H_2O with injection of MV (aq.) ($c = 36 \text{ }\mu\text{M}$) at $P = 5.6 \text{ kW/cm}^2$. $\lambda = 470 \text{ nm}$, cw.

PL intensity gets completely quenched within a few seconds. This experiment serves as an experimental test of the method, but also demonstrates the effect of high-efficiency electron scavengers on the PL of CdSe QWs.

Similar experiments were conducted with aqueous solutions containing AgNO_3 and $\text{Cd}(\text{Ac})_2$. As discussed in Section 2.1.2, these additives have significant effects on the PL properties of CdSe NCs.

The evolution of the spectra while infusing AgNO_3 (aq.) is shown in Figure 4.21(a). After the injection, the PL intensity exhibits a significant increase by a factor of two, while the FWHM decreases by 50% and the peak maximum shifts to the blue by 12 nm ((1)→(2)). Within 60 s after this PL enhancement, the PL gets quenched completely ((2) →(3)). The evolution of the spectra in the analogue experiment with $\text{Cd}(\text{Ac})_2$ is shown in Figure 4.21(b). In this particular case the initial PL intensity in water is too low to be detected in the spectra with the settings chosen for this experiment. Therefore changes concerning wavelength and FWHM are not available. Yet, a pronounced enhancement of the PL intensity of a factor of more than five is observed after injection of the $\text{Cd}(\text{Ac})_2$ solution. In contrast to the subsequent complete PL quenching observed for $\text{Ag}(\text{NO}_3)$, the PL does not disappear completely but decreases to around 40% of the enhanced intensity.

For the interpretation of the observed effects, it can be referred to the processes for CdSe NCs reported in the literature.^{52,57} It has been reported that the addition of AgNO_3 leads to a cation exchange reaction, which would eventually lead to a complete quenching of the PL (in the visible range).⁵² However, for the doping of CdSe NCs with only a few Ag atoms PL enhancement was observed.⁵⁷ Applying these concepts to the data shown

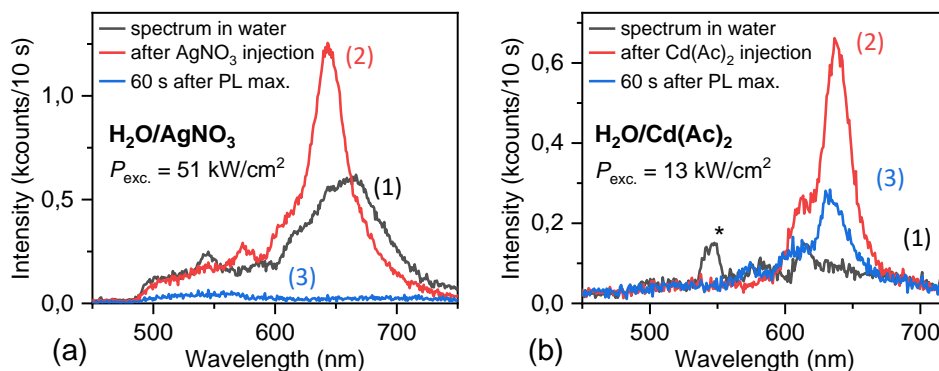


Figure 4.21: Evolution of spectra of CdSe QWs in aqueous solutions in flow channels. (a) Evolution after injection of AgNO_3 (aq.) ($c = 2 \text{ mM}$). (b) Evolution after injection of $\text{Cd}(\text{Ac})_2$ (aq.) ($c = 2 \text{ mM}$). (*) marks detected light of other sources owing to the special experimental setup. $\lambda = 470 \text{ nm}$, cw.

in Figure 4.21(a), allows for the interpretation that the PL enhancement, observed after injection and before the PL quenching, is due to impurity doping by the first arriving Ag atoms at the QWs. Even though this approach yields an explanation for the observed PL enhancement it is questionable if these concepts can also be applied to 1D structures. The explanation of the PL enhancement for the 0D NCs is based on the reorganisation of the exciton fine structure due to breaking the symmetry by inserting an impurity into the particle.⁵⁸ Whether the effect of changes in the exciton fine-structure has a similar impact on the PL in wires is unclear. Another approach might be surface passivation due to Ag^+ ions. Indeed this has been proposed for chalcogene rich II-VI NCs to lead to PL enhancement.¹⁸⁴ This approach would be in good agreement with the findings concerning the composition of the Se-rich CdSe QWs used in these experiments and coincides with the proposed mechanism for the oxygen-based photobrightening (see Section 4.2.3).

For $\text{Cd}(\text{Ac})_2$, it was suggested that this substance could lead to an enhanced surface passivation, thus leading to PL enhancement of CdSe NCs.⁵² Yet, the exact mechanism was not entirely clarified. In principle, $\text{Cd}(\text{Ac})_2$ can act as Z-type ligand and passivate undercoordinated Se^{2-} ions at the surface, thus decreasing the number of surface trap states. In aqueous solution, however, the dissociation products could also act as X-type ligands, passivating undercoordinated Cd^{2+} ions at the surface. Furthermore, the subsequent quenching of the PL intensity is difficult to explain. However, the preservation of some of the enhanced luminescence is the main difference to the cation exchange reaction occurring with AgNO_3 . The complexity of this case makes it difficult to make a definite statement about the effect of the surface passivation. Again, a directional aspect is that PL enhancement due to passivation of undercoordinated Se ions at the surface

coincides with the findings concerning the photoinduced PL enhancement due to oxygen (see Section 4.2.3), but a potential interplay of different effects cannot be discarded.

The results for the evolution of the PL in aqueous solutions, shown in Figure 4.21, have to be considered with some caution. The measurements in the flow-channels were difficult to conduct and controlling the system's stability concerning the focal point was tedious. Furthermore, it was difficult to estimate the exact time of the additives arriving at the investigated CdSe QWs, thus causing some uncertainties concerning the interpretation of the data. Nevertheless, these experiments show that some of the principles found for spherical CdSe NCs also account for CdSe NWs. Further, the observation that substances that may passivate Se surface-sites lead to PL enhancement supports the mechanism proposed for the oxygen-mediated photobrightening.

Effect of Gaseous Propylamine

In order to investigate the effects of L-type ligands on the PL properties, experiments were conducted in which the gaseous surroundings of the CdSe QWs were flushed with an atmosphere, containing gaseous *n*-propylamine. For these experiments, a carrier gas was bubbled through liquid *n*-propylamine before introducing it into the flow-channel.

Figure 4.22 shows the evolution of the spectra of CdSe QWs while flushing the flow-channel with a gaseous mixture of O₂ as carrier gas and *n*-propylamine. The effect of the amine is dominant and further experiments with different carrier gases showed that the main aspects of the effect of *n*-propylamine are not affected by the carrier gas. Figure 4.22(a) shows the evolution of the PL spectra over time as color map. During the measurement of 180 s, the PL intensity is gradually quenched. Strikingly, large fluctuations of both PL intensity and emission wavelength are observed in the process. The spectra recorded at 1 s and at 65 s are displayed in Figure 4.22(b) and (c), respectively. The data can be represented by applying three Lorentzians. The shoulder at higher wavelengths (peak 3) might be assigned to CdSe trap emission,⁵² but this will not be in the focus of the following discussion. Next to the main emission peak in the initial state at 691 nm (peak 1), a second blue-shifted peak at 657 nm (peak 2) appears in a fluctuating manner. The energy shift of 93 meV corresponds well to the energy shift between the two peaks observed in the study of the reversible photoinduced effects of oxygen on the PL properties of CdSe QWs (see 2.1.2). Alkylamines can act as L-type ligands that bind to the NC surface by donating a free electron pair.^{49,50,185} Analogous to the proposed mechanism for the occurrence of emission of higher states at high excitation powers in inert gas atmospheres, it can be concluded that the high energy emission peak is created due to an increased amount of negative charge carriers. In this case the extra

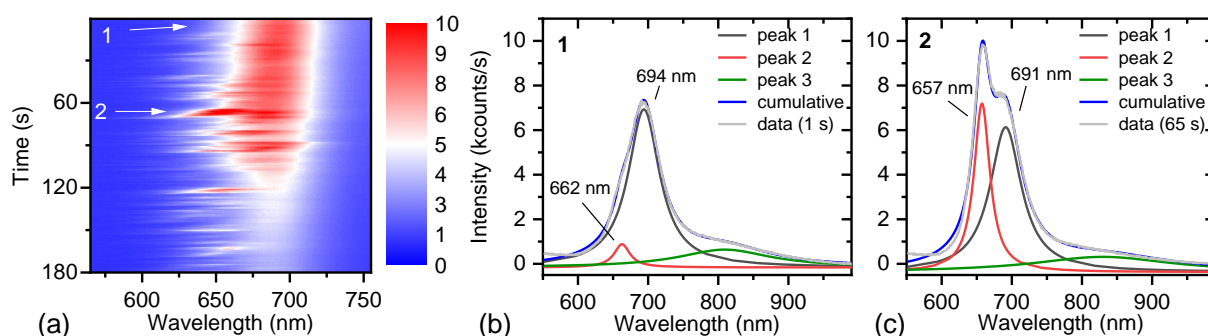


Figure 4.22: Evolution of the PL spectra of CdSe QWs in an atmosphere with gaseous *n*-propylamine. (a) Colormap of the transient data. (b,c) Spectra at 1 s and 65 s (marked with 1 and 2 in (a)), each fitted with three Lorentzians. $P = 62 \text{ kW/cm}^2$, $\lambda = 447 \text{ nm}$, cw.

charge carriers are provided by *n*-propylamine that injects electrons either indirectly by passivation of electron traps, or injects electrons directly by oxidation at the surface.

In conclusion, the flow-channel experiments revealed some interesting features of PL variations. The results for the additives in aqueous solutions can in part be correlated with principles established for CdSe NCs. However, the interpretation of the measured data in this work is not always unambiguous. Reoccurring experimental problems with the stability of the experimental setup complicate the realization of a larger comprehensive study. Nevertheless, the investigations complemented the findings discussed in the previous sections in several ways. For example, the importance of the increased Se content for the optical properties are implemented repeatedly in the interpretation. Furthermore, the results of the experiments with *n*-propylamine are a good addition to the observation of emission of higher excited states with excess negative charge carriers.

4.3 CdSe/CdS Core-Shell Particles

In order to compare the observations and findings on NWs to another system, the PL of CdSe/CdS core-shell particles was investigated. Those QDs resemble a benchmark system in terms of PL-quantum yield. The advancement of synthetic strategies during the last decades led to an almost complete reduction of blinking, thus increasing the suitability in many optoelectronic devices.^{7,143,149,186,187} For CdSe/CdS QDs, some reversible effects of oxygen on the PL properties were already reported by Hu et al.²⁰ In this work, a part of the observations reported in the literature were confirmed. However, some new aspects were discovered and analyzed, leading to a more complete picture of the interaction of oxygen and the PL of QDs. In the following sections, the results of the investigations regarding the impact of oxygen are demonstrated. The PL properties were examined on thin films, as well as on single particles.

4.3.1 Photoluminescence Properties of QD Thin Films

To investigate the properties of QDs on an ensemble level, while profiting from the advantage of high photon collection efficiency of microscope objectives, thin films were examined by confocal spectroscopy. In general, the strategy and methods were similar to those used for CdSe QWs.

Figure 4.23(a) shows the development of the PL properties of CdSe/CdS QDs in a thin film during fast switching of the surrounding atmosphere between oxygen and nitrogen under continuous illumination. Starting in oxygen atmosphere, in the first seconds of the measurement the PL intensity increases by a factor of 1.2 and stabilizes after 30 s. The small increase in PL intensity is accompanied by a very small blue-shift of the emission wavelength of 0.2 nm. When changing the atmosphere to nitrogen, the PL intensity decreases by more than 50%, the emission wavelength experiences a red-shift by 3 nm and the spectrum broadens significantly. Figure 4.23(b) and (c) show representative PL emission-spectra and PL decay-curves in the respective atmospheres. The lifetimes in nitrogen are significantly shorter than in oxygen. In both atmospheres, at least triexponential fit functions have to be applied to represent the data sufficiently. The average lifetimes were determined to be 59 ns in oxygen and 9 ns in nitrogen. The data suggest different states of recombination to be dominant in each atmosphere. By changing the atmosphere during illumination, the states can be switched reversibly as shown by the time trace in Figure 4.23(a).

So far, the data are in agreement with the literature.²⁰ It was reported that oxygen deionizes negatively charged QDs, thus leading to emission of neutral excitons in oxygen, whereas the emission in inert gas is dominated by negative trions. The red-shift of the

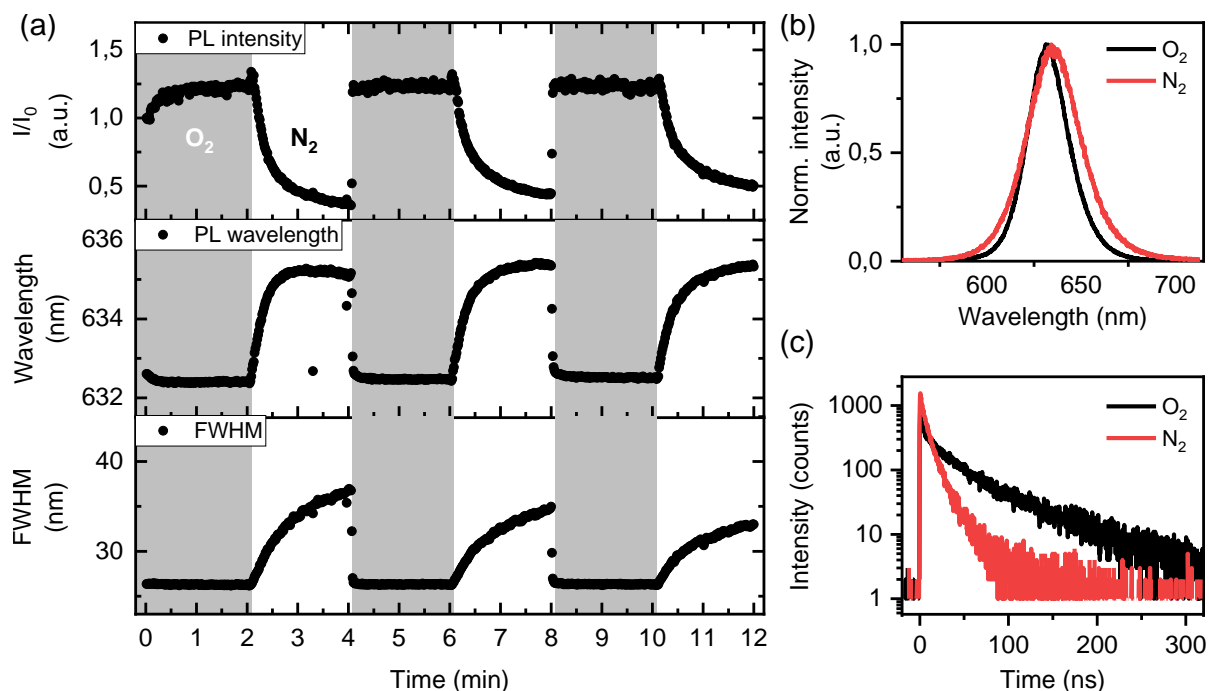


Figure 4.23: PL properties of CdSe/CdS core-shell particles ($d = 12.6$ nm) in a thin film. (a) Development of the PL intensity, PL wavelength and FWHM while switching the gas atmospheres between O_2 and N_2 under continuous illumination ($\lambda = 405$ nm, $P = 20$ μ W, $f = 1$ MHz). (b) PL emission spectra and (c) PL decay-curves in O_2 and N_2 , respectively.

emission wavelength is also characteristic for trions and results from increased Coulomb interactions with the additional charge carrier.¹⁸⁸ The reversible broadening was attributed to the existence of a mixture of neutral and negatively charged QDs in inert gas atmospheres, whereas only neutral QDs would be present in oxygen.²⁰ Further, the shortening of lifetimes in inert gas atmospheres is also in agreement with the assignment to the negative trion state. In trions, Auger recombination can occur as additional non-radiative recombination pathway. Furthermore, the probability for radiative recombination is enhanced due to the increased amount of charge carriers.

Interestingly, when performing the same experiment at lower emission powers, the effect of the atmosphere on the PL properties vanishes. To investigate the influence of the excitation power, a similar experiment was performed, in which the excitation power was varied in a stepwise manner during the measurement. Figure 4.24 (a) shows the development of the PL intensity of a thin film of CdSe/CdS QDs with switching gas atmospheres, while increasing the excitation power step by step. From the data of the intensity time-trace, an excitation-power threshold can be identified. Only at powers above 0.5 μ W, oxygen leads to an enhancement of the PL intensity. Further, the extent of the effect increases with increasing power. The data in Figure 4.24 (b)–(d) support this

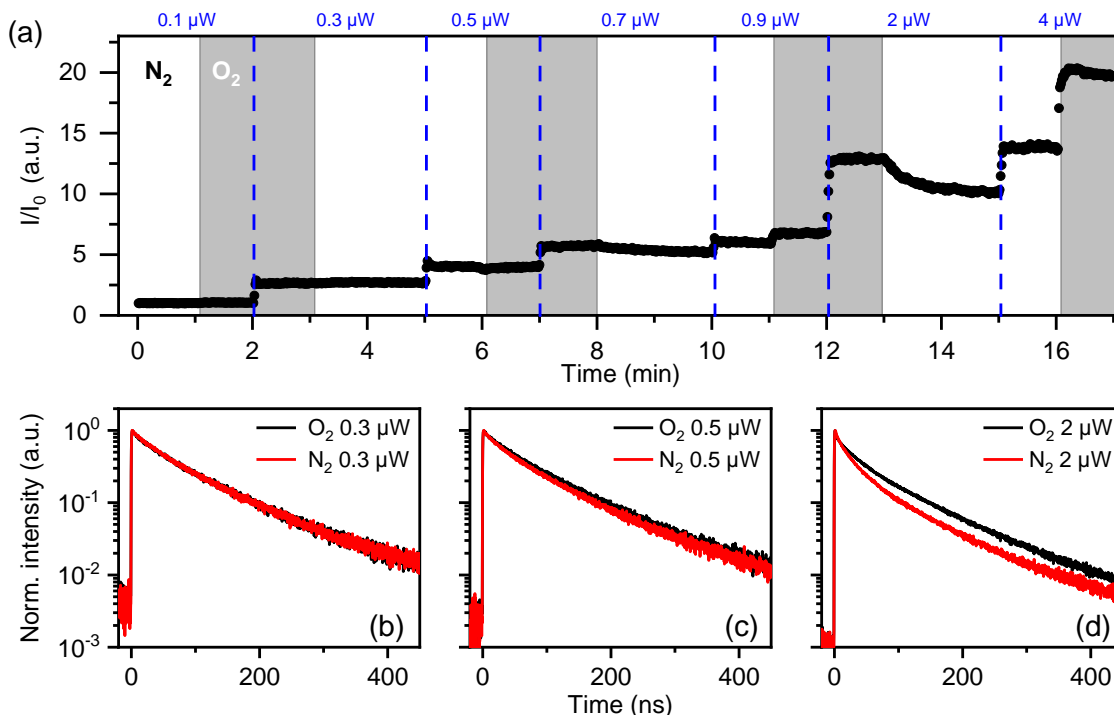


Figure 4.24: PL properties of CdSe/CdS core-shell particles ($d = 12.6$ nm) in a thin film. (a) Development of the PL intensity while switching the gas atmospheres between O_2 and N_2 , as well as increasing the excitation power step by step ($\lambda = 405$ nm, $f = 1$ MHz). (b)-(d) PL decay-curves in the respective gas atmospheres at 0.3 μ W, 0.5 μ W and 2 μ W.

observation: the effect of the atmosphere on the slope of the decay curves increases with increasing excitation power and is only observed above a certain power threshold at all. This disagrees with the findings reported by Hu et al., who observed effects of oxygen at low excitation powers in the regime of single excitons.²⁰

Compared to the QDs used by Hu et al., the QDs used in the experiments shown in Figure 4.23 and 4.24 have a larger CdS shell. Also other parameters in the synthesis, such as reaction time of the shell growth may not be completely identical. As an essential aspect, however, the variation of the shell thickness will be the focus of the following investigations. The samples examined in this work are summarized in Table 4.3. For all samples shown here, the CdSe core NCs have a diameter of 4.4 nm. The optical properties of the QD ensembles are quite similar. They all exhibit high QYs above 80% and the emission wavelengths only varies insignificantly.

The QDs used in the study by Hu et al. were synthesized with smaller cores of 3.5 nm and smaller shells with only 7 MLs of CdS.²⁰ The smallest QD sample investigated here lies in a similar range with respect to size and composition. However, neither that sample nor any of the other samples in Table 4.3 showed the effects of oxygen on the PL at low excitation powers as reported by Hu et al.²⁰ In this work, for all samples an excitation-power

Table 4.3: CdSe/CdS QD samples provided by Sonja Krohn. The diameter d was determined via TEM. The CdSe-core diameter was 4.4 nm for all samples. The number of MLs of CdS were calculated with 0.3375 nm per ML.¹⁸⁹ The QY was determined in an ensemble measurement in solution by Sonja Krohn. The given values for the emission wavelength λ were measured on thin films on substrates.

Sample	Cd-0-310	Cd-0-326-2	Cd-0-343	Cd-0-319	Cd-0-337
d (nm)	7.6	9.1	11.6	12.6	14
CdS MLs	9.5	14	21	24	28
QY (%)	–	86	86	83	84
λ (nm)	631	634	636	633	634

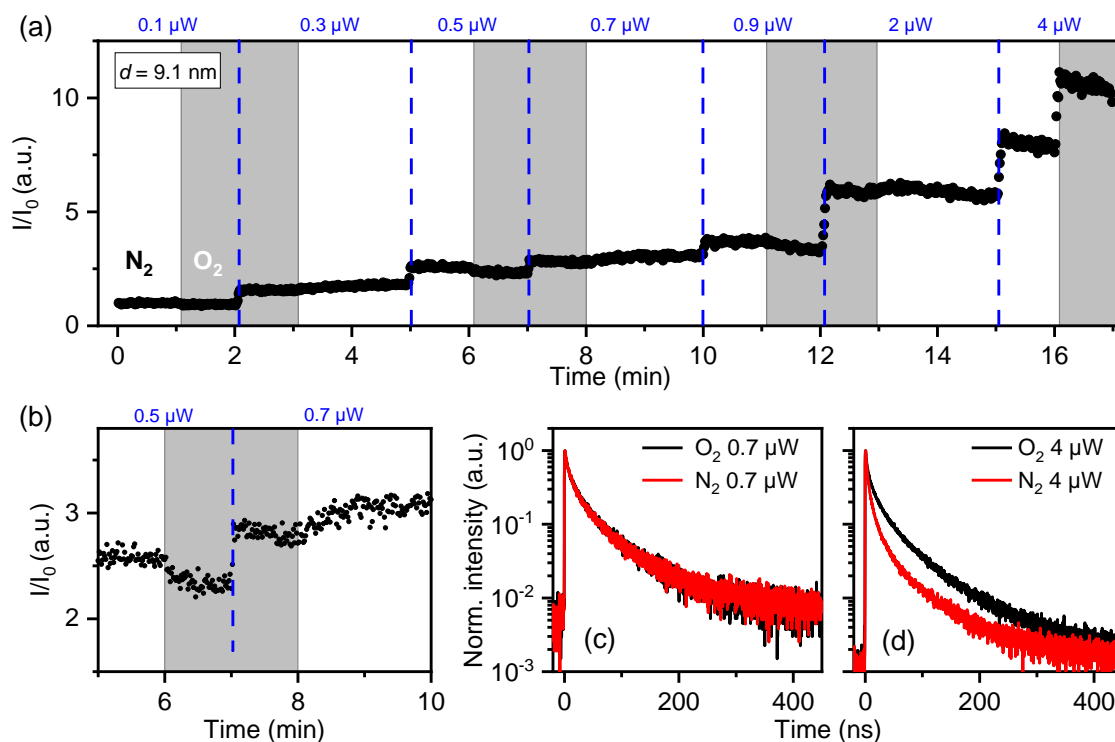


Figure 4.25: PL properties of CdSe/CdS core-shell particles ($d = 9.1$ nm) in a thin film. (a) Development of the PL intensity while switching the gas atmospheres between O_2 and N_2 , as well as increasing the excitation power step by step ($\lambda = 405$ nm, $f = 1$ MHz). (b) Enlarged section of the data shown in (a). (c)-(d) PL decay-curves in the respective gas atmospheres at 0.3 μW , 0.5 μW and 2 μW .

threshold must be overcome to observe an enhancement of the PL intensity in oxygen. This observation might indicate that for the QDs investigated in this work the formation of multiexcitons is necessary to obtain the negative trion in nitrogen atmospheres. For the QDs investigated by Hu et al., excitation in the single exciton regime was sufficient to reach the negative trion state in nitrogen.²⁰ This indicates differences in the ionization processes. In order to determine the excitation power thresholds observed in this work, the experiment shown in Figure 4.24 was performed for every sample in the same manner. Surprisingly, the power threshold showed no correlation to the shell thickness. This observation leads to the following conclusions about the properties of the giant-shell QDs investigated in this work. First, variations of the shell thickness in this size-regime have no impact on the electron scavenging by oxygen. Apparently larger shells do not hinder the delocalized electrons in negative trions from reaching the surface. This seems reasonable, since the offset in the CB between core and shell material is rather small, which likely enables a large delocalization of electrons over the whole particle.¹⁹⁰ Second, the ionization that leads to negatively charged QDs in the first place, is not significantly affected by the shell thickness.

At high excitation powers, all samples in Table 4.3 showed the same PL properties in changing atmospheres as shown in Figure 4.23. Yet, at low excitation powers a peculiar observation was made for particles with smaller diameters of 7.6 nm and 9.1 nm. Figure 4.25 shows the data for QDs with diameters of 9.1 nm. At first glance, the PL intensity time trace in Figure 4.25(a) looks similar to the data of bigger QDs. The significant effect of PL enhancement by oxygen is only observed at high excitation powers. Yet, on a closer inspection, a reversible quenching of the PL in oxygen is observed at low excitation powers, which is highlighted in Figure 4.25(b). This was not observed for larger particles. Decay curves at low and high excitation powers are shown in Figure 4.25(c–d). At high excitation powers the lifetimes are, as expected, prolonged in the presence of oxygen. However, at low excitation powers, the decay curves are identical in each atmosphere, even though a difference in intensity is observed.

The change in the PL intensity while the decay curves remain unaffected can be explained in two ways. First, the number of QDs exhibiting radiative recombination in oxygen atmosphere decreases, while the recombination mechanisms of the QDs that still show radiative recombination stay unchanged. Secondly, a non-radiative channel is added in oxygen, which does not compete with the radiative channel, similar to B-type blinking, in which hot charge carriers are trapped. The first explanation would only account for ensemble measurements, while hot charge-carrier trapping should also affect the blinking statistics of single particles. Either way, instead of the formation of negatively charged trions, which only occurs at high excitation powers, another process has to be accounted

for. According to the mechanism proposed by Koberling et al.,¹⁸ adsorbed oxygen at the particle surface can provide additional trap-like states by acting as an electron acceptor. Electrons trapped this way could then recombine non-radiatively with holes trapped at the surface. The observation of unchanged decay curves in Figure 4.25(c) suggests that either, there are QDs which then would get quenched completely, or that only hot charge carriers can participate in this process.

In summary, the experiments show that while the oxygen-induced effects reported by Hu et al.²⁰ could be replicated in this work, the overall picture of the influence of oxygen on the PL properties of CdSe/CdS QDs is more complex than assumed to this point. In order to observe any effects by oxygen for "big-shell particles" a power threshold has to be overcome. And for "small-shell particles" even the opposite effect on the PL intensity was observed at low excitation powers. In order to shed more light on the underlying processes, single-dot measurements were performed and will be discussed in the following sections.

4.3.2 Photoluminescence Properties of Single Particles

In contrast to ensemble measurements, in single-particle measurements PL blinking can be investigated. By determining the blinking dynamics on a single-particle level, effects that were observed for the collective might be clarified. Single-particle measurements were performed on the same samples discussed in the section above. QDs with diameters of 12.6 nm and 9.1 nm were investigated in atmospheres of oxygen and nitrogen at high and low excitation powers. In this section the two samples will be referred to as "big-shell" and "small-shell" QDs, respectively. The excitation powers are given as excitons per pulse, which were calculated according to the approach described in Section 3.1.1.

Single "Big-Shell QDs"

Figure 4.26 shows the data of single-particle measurements of "big-shell QDs". The PL time-traces in Figure 4.26(a) and (d) at low excitation powers (0.07 excitons/pulse) in oxygen and nitrogen look very similar. No clear blinking events can be observed, neither at the chosen bin time of 100 ms, nor at lower bin times. Only small intensity fluctuations differ from a constant shot noise limited emission. The occurrences of the detected photons can both be described with Poisson distributions, as shown in Figure 4.26 (b) and (d). Further, the PL-decay curves in Figure 4.26(c) and (f) are almost identical. In both cases the data is represented by monoexponential fit functions. The lifetimes were determined to be 76.7 ns and 76.5 ns in oxygen and nitrogen, respectively.

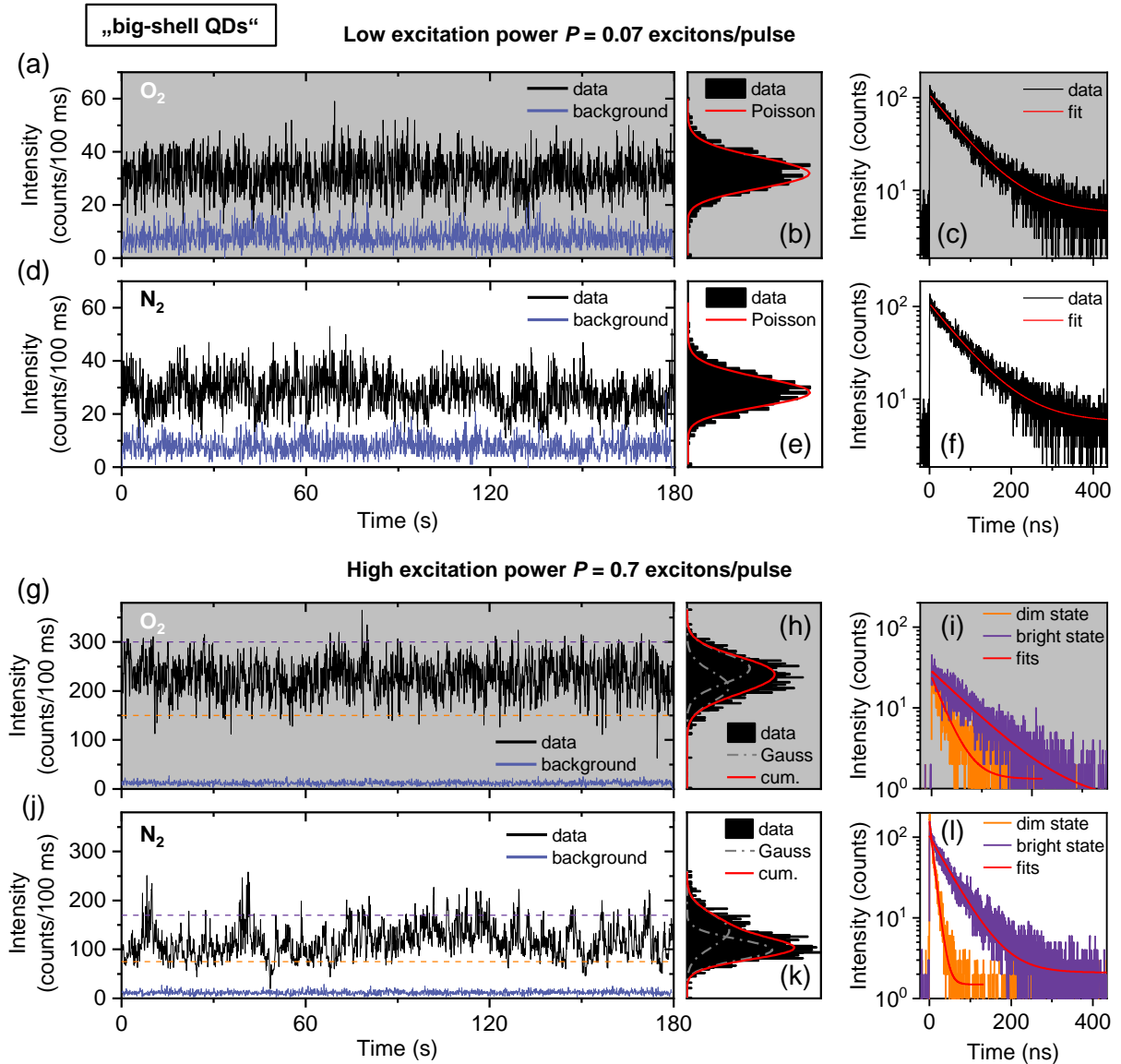


Figure 4.26: PL properties of a representative single CdSe/CdS QD ($d = 12.6$ nm). (a–c), (d–f) Data at low excitation powers (0.07 excitons/pulse) in O_2 and in N_2 , respectively. (g–i), (j–l) Data at high excitation powers (0.7 excitons/pulse) in O_2 and in N_2 , respectively. First column: Time traces of the PL intensity of the QD and the intensity of the background (bin time = 100 ms). Second column: Histograms with Poisson distributions (b,e), or Gauss functions (h,k). Third column: PL decay-curves with monoexponential fit functions. The decay-curves in (i,l) result from the bins above and below the thresholds marked in the respective time trace (called here bright and dim states). Fitting results are given in Table 4.4. All measurements were performed on the same QD with $\lambda = 405$ nm and $f = 1$ MHz.

These observations are in agreement with the ensemble measurements for "big-shell QDs" at low excitation powers. No effect of the atmosphere on the PL properties is observed as long as the power threshold, found in the ensemble measurements, is not overcome. The absence of blinking events in these particles is in contrast to the data reported by Hu et al.,²⁰ in which blinking was observed at excitation powers in the single exciton regime. A preferred occupation of the bright state in oxygen versus the dim state in inert gas was reported. The absence of blinking in the low-power experiments for the "big-shell QDs" in this work is most likely related to the absence of an effect of the atmosphere.

In contrast to the data at low excitation powers, differences in the respective atmospheres are observed at higher powers of 0.7 excitons/pulse. The comparison of the PL time-traces in oxygen and in nitrogen, shown in Figure 4.26(g) and (j), reveals the enhancement of the PL intensity by oxygen, which was already observed in the ensemble measurements. Both time traces exhibit intensity spikes and dips. The occurrences no longer follow a Poisson distribution, as shown in Figure 4.26(h) and (k). Each distribution is fitted with two Gauss functions. The majority of events lies around 230 counts per 100 ms in oxygen and around 100 counts per 100 ms in nitrogen, while the distribution is broadened towards lower counts in oxygen and towards higher counts in nitrogen. This representation highlights that in each atmosphere there is an occasional change between the prevailing recombination states, which is also manifested by the spikes and dips in the time traces. Due to the relatively large bin time chosen in this representation, the intensity levels of the spikes and dips are obscured, which is why they do not reach the level of the dominating state in the other atmosphere. This will be discussed in more detail later. The fluctuations in both time traces at high excitation power allow for the determination of thresholds for high- and low-intensity bins, hereafter referred to as bright and dim state. Figure 4.26(i) and (l) show the decay curves for the bins above and below the respective thresholds marked in the time traces. The decay curves can be represented by monoexponential fit functions. For the total data, the decays are fitted with triexponential fit functions (not shown here), yielding average lifetimes of 77.1 ns in oxygen and 33.2 ns in nitrogen. The determined lifetimes are summarized in Table 4.4.

First of all, the results of the single-particle measurements confirm the findings of the ensemble measurements in respect to the power threshold that has to be overcome in order to observe the PL enhancement effect by oxygen. This is in contrast to the data reported by Hu et al.²⁰ The differences in the blinking properties (almost no blinking in this work versus occasional blinking in the work of Hu et al.) are probably linked to this phenomenon. Further, the changes of the PL that occur at high excitation powers in this work are not as drastic as those reported by Hu et al. for low excitation powers. In this work, the PL intensity drops only to 40% of the value in oxygen when illuminating in

Table 4.4: Average PL lifetimes of the "big-shell QD", determined from the data shown in Figure 4.26.

		low power		high power	
		O ₂	N ₂	O ₂	N ₂
total	fit	monoexp.	monoexp.	triexp.	triexp.
	τ_{av} (ns)	76.7	76.5	77.1	33.2
bright state	fit	-	-	monoexp.	monoexp.
	τ_{av} (ns)	-	-	72.6	47.8
dim state	fit	-	-	monoexp.	monoexp.
	τ_{av} (ns)	-	-	30.2	9.74

inert gas, instead of to 18% in the case of Hu et al. Also the change of the average lifetime when changing to inert gas is not as drastic, since the average lifetime decreases by 57% instead of 91% (from 22 ns to 2 ns in the work of Hu et al.). This is most likely correlated with the fact that in this work high excitation powers are needed to observe an effect of the atmosphere. At these excitation powers, multiexcitons may be involved, affecting the PL intensities and lifetimes. Yet, the comparison of the bright and dim states for these data can yield further information about the respective mechanism of the charge-carrier recombination. This will be elaborated in Section 4.3.3.

Single "Small-Shell QDs"

Figure 4.27 shows the same set of data for a "small-shell QD". At low excitation powers in oxygen significant blinking or flickering of the PL intensity is observed in the time trace in Figure 4.27(a). The relatively broad histogram in Figure 4.27(b) can be fitted by two Gauss functions. Figure 4.27(c) shows two decay curves, which were obtained for time bins below and above certain thresholds, for which the levels are marked in Figure 4.27(a). In the following, the high-intensity bins are referred to as bright states and the low-intensity bins are referred to as dim states. Figure 4.27(d–f) shows the data obtained by illuminating the same dot in nitrogen. Far less flickering is observed and the PL intensity stays mostly on a lower level. The decay curves for the bright and dim states at low excitation powers, depicted in Figure 4.27(c,f), can be represented with monoexponential fit functions.

At high excitation powers, the trends observed for low excitation powers are similar, as shown by the data in Figure 4.27(g–l). In oxygen, severe PL fluctuations are observed, while the PL stays mostly on a lower level in nitrogen. By comparing the time traces in oxygen at high and at low excitation powers slight differences are noticeable as less flickering is observed at high powers, and the PL is in the dim state for longer periods.

Table 4.5: Average PL lifetimes of the "small-shell QD", determined from the data shown in Figure 4.27.

		low power		high power	
		O ₂	N ₂	O ₂	N ₂
total	fit	biexp.	biexp.	triexp.	triexp.
	τ_{av} (ns)	41.8	23.0	32.2	16.3
bright state	fit	monoexp.	monoexp.	biexp.	biexp.
	τ_{av} (ns)	49.6	24.9	57.6	29.8
dim state	fit	monoexp.	monoexp.	biexp.	biexp.
	τ_{av} (ns)	6.66	8.96	7.16	6.18

Here, the decay curves cannot be represented by monoexponential fit functions. The data for the bright and dim states shown in Figure 4.27(i,l) are fitted with multiexponential functions.

In contrast to the measurements of "big-shell QDs" an effect of the atmosphere is already observed at low excitation powers. By comparing the time traces in oxygen and in nitrogen, shown in Figure 4.27(a) and (d), it becomes obvious that in nitrogen the PL blinking is largely suppressed, but the PL stays mostly in the dim state. Therefore, in contrast to the results for the "big-shell QDs", the results obtained for the "small-shell QDs" are more similar to those reported for CdSe/CdS QDs by Hu et al.²⁰

The determined average lifetimes for both excitation powers in both atmospheres are summarized in Table 4.5. At low excitation powers, fitting the decays of the total data (not shown in Figure 4.27) yield average lifetimes of 41.8 ns and 23.0 ns in oxygen and in nitrogen atmosphere, respectively. Therefore, the effect of oxygen is still not as drastic as reported by Hu et al.²⁰ and the lifetime is only reduced to about half when switching from oxygen to nitrogen. This indicates the requirement of a more complex description of the processes observed in this work. To analyze the fluctuations in more detail, the blinking statistics are evaluated.

4.3.3 Blinking Analysis

Fluorescence Lifetime-Intensity Distributions

The nature of the blinking mechanisms in a QD can be identified by the analysis of the fluorescence lifetime-intensity distribution (FLID).¹⁴⁶⁻¹⁴⁸ In general, the shape of the correlation of the FLID can be used to determine the blinking mechanism present in a QD. A linear relation of PL intensity and lifetime can indicate bandedge-carrier blinking,

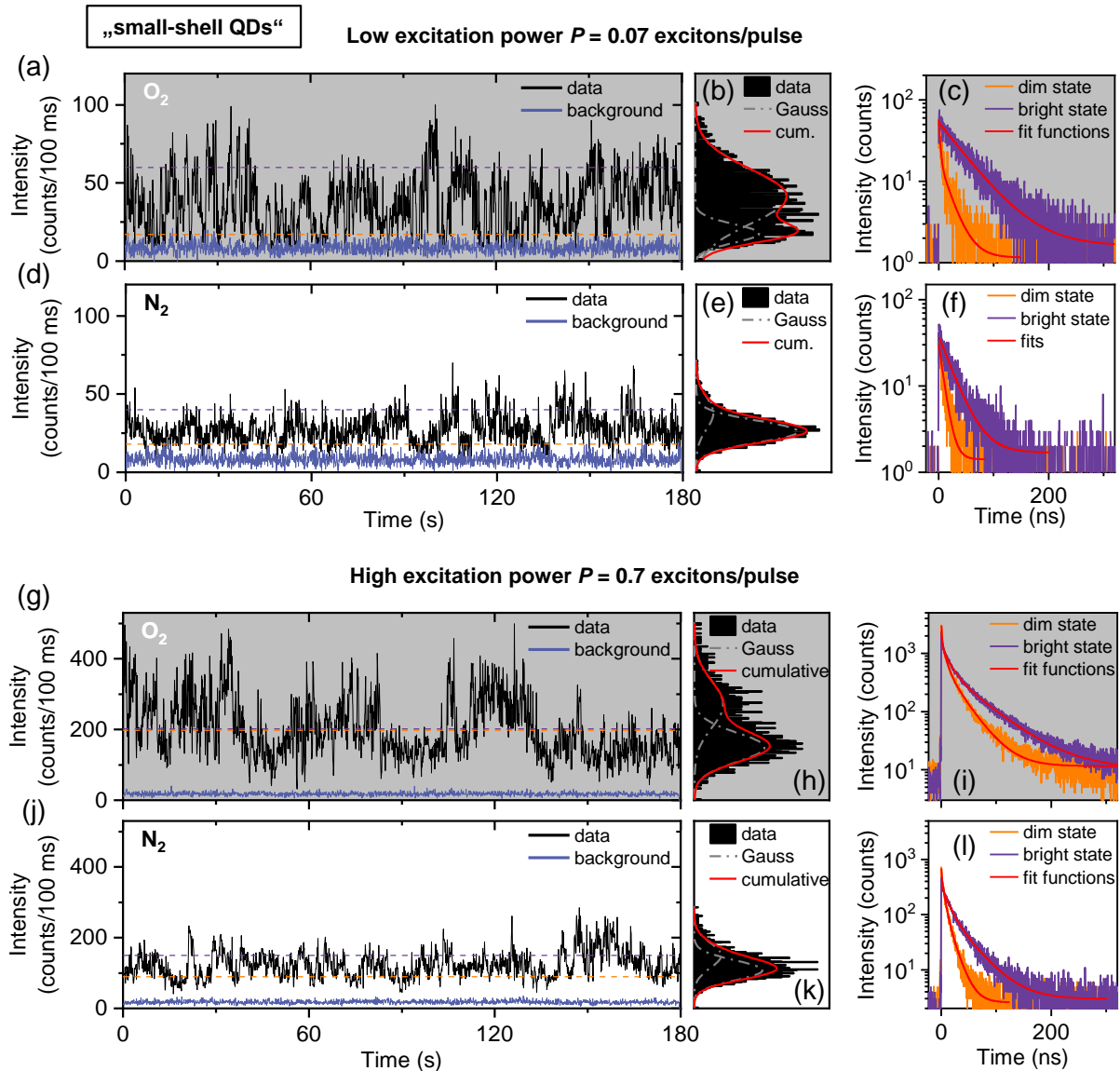


Figure 4.27: PL properties of a representative single CdSe/CdS QD ($d = 9.1$ nm). (a–c), (d–f) Data at low excitation powers (0.07 excitons/pulse) in O_2 and in N_2 , respectively. (g–i), (j–l) Data at high excitation powers (0.7 excitons/pulse) in O_2 and in N_2 , respectively. First column: Time traces of the PL intensity of the QD and the intensity of the background (bin time = 100 ms). Second column: Histograms with Gauss functions. Third column: PL decay-curves of the data points above and below the thresholds marked in the respective time trace (called here bright and dim states). Fitting results are given in Table 4.5. All measurements were performed on the same QD with $\lambda = 405$ nm and $f = 1$ MHz.

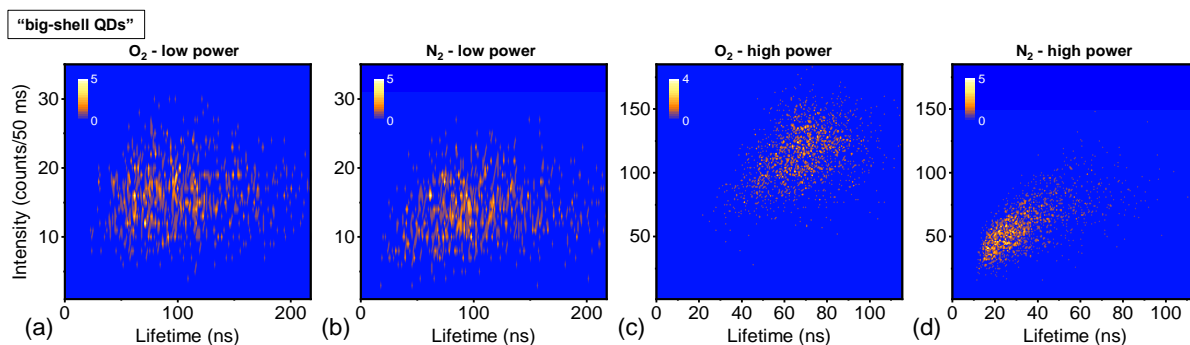


Figure 4.28: FLIDs of a single CdSe/CdS QD ($d = 12.6$ nm) in O_2 and N_2 at low (0.07 excitons/pulse) and high (0.7 excitons/pulse) excitation powers. (a–b) FLIDs at low excitation powers in O_2 and N_2 . (c–d) FLIDs at high excitation powers in O_2 and N_2 . The underlying data are shown in Figure 4.26. Bin time: 50 ms.

whereas a curved "line" is related to Auger blinking.¹⁴⁸ No correlation is usually assigned to hot-carrier blinking (see Figure 2.16).¹⁴⁶

"Big-shell QDs" Figure 4.28 shows the FLIDs for the "big-shell QDs" in oxygen and nitrogen atmospheres, each at low (a–b) and at high (c–d) excitation power. In agreement with the assessments made before, differences in the PL dynamics are only observed at high excitation powers when changing the atmospheres.

At low excitation powers in Figure 4.28(a,b), the distribution of lifetimes is relatively broad, but as no blinking was present (see Figure 4.26), no bi-modal distribution or other correlation is observed. At high excitation powers in Figure 4.28(c,d), the effect of the atmosphere becomes very clear. In oxygen, both PL intensity and lifetime are at a higher level than in nitrogen. Additionally, very rare intensity fluctuations lead to a slight asymmetric distribution in each plot. Since the PL stays mostly in the respective dominant state, which is presumably neutral emission in oxygen and emission of negatively charged trions in nitrogen, no further analysis is possible for the respective FLID diagrams. However, it is possible to determine the radiative lifetime scaling of the bright and dim states in each atmosphere.

Yuan et al.¹⁴⁸ state that the radiative lifetime scaling can indicate the dominant blinking mechanism in a QD, as bandedge-carrier blinking leads to a factor ≈ 1 and Auger blinking leads to a factor ≈ 2 . The factor 2 in Auger blinking is due to the competition of charged trions in the dark/dim state with neutral excitons in the bright state. In trions, the charge carriers have twice as many opportunities to recombine as the charge carriers of neutral excitons.

For this analysis, the bright and dim states set in the time traces in Figure 4.28 are compared. At the excitation powers used in this experiment it is likely that multiexcitons are involved, which complicates the determination of the radiative lifetime scaling. However, this problem can be avoided by only considering the bins that contribute to monoexponential decay in the bright and dim states. For the case in oxygen, the radiative lifetime scaling of the bright state X and the dim state X* is calculated according to

$$\frac{\tau_r(X)}{\tau_r(X^*)} = \frac{\tau(X) I(X^*)}{I(X) \tau(X^*)} = \frac{72.6 \text{ ns}}{(310 - 12) \text{ cnts}/100 \text{ ms}} \frac{(131 - 12) \text{ cnts}/100 \text{ ms}}{30.2 \text{ ns}} = 0.96,$$

with the intensities $I(X) = 310 \text{ cnts}/100 \text{ ms}$, $I(X^*) = 131 \text{ cnts}/100 \text{ ms}$, $I_{\text{background}} = 12 \text{ cnts}/100 \text{ ms}$ and the respective lifetimes $\tau(X) = 72.6 \text{ ns}$, $\tau(X^*) = 30.2 \text{ ns}$.

The scaling factor of the radiative lifetimes is ≈ 1 . This is usually associated with bandedge-carrier blinking. Yuan et al. already observed a correlation of the presence of oxygen on bandedge-carrier blinking. They proposed that oxygen molecules enable bandedge-carrier blinking by opening and closing trap sites for bandedge carriers through adsorption and desorption of oxygen molecules on the surface.¹⁴⁸ The analysis of the radiative-lifetime scaling approves the proposed correlation.

Performing the same analysis for the data of the "big-shell QD" in nitrogen yields a scaling factor of the radiative lifetimes of 1.5. The determination of a factor that is significantly >1 is a clear indication of the presence of trions undergoing non-radiative recombination via the Auger effect.¹⁴⁸ This is in agreement with the proposition of Hu et al., that negatively charged species are formed in the absence of oxygen in the atmosphere.²⁰ However, for the "big-shell QDs" this is only observed at high excitation powers, at which most likely multiexcitons are present.

"Small-shell QDs" Figure 4.29 shows the FLIDs for the "small-shell QDs" in oxygen and nitrogen atmospheres, each at low (a–b) and at high (c–d) excitation power. In contrast to the FLIDs for the "big-shell QDs", the effect of the atmosphere is clearly observed even at low excitation powers, which confirms the assessments made in the previous sections.

The FLID in oxygen at low excitation powers, shown in Figure 4.29(a), spreads over a large range in both lifetime and intensity direction. In this distribution some events with a linear correlation of intensity of lifetime might be identified, along with events that are either correlated in a curved shape or are not correlated at all. While a direct identification of a dominating blinking mechanism is not possible, the FLID indicates that several blinking mechanisms are present. At high excitation powers in oxygen, the FLID in Figure 4.29(c) reveals a majority of linearly correlated events, thus indicating bandedge-carrier

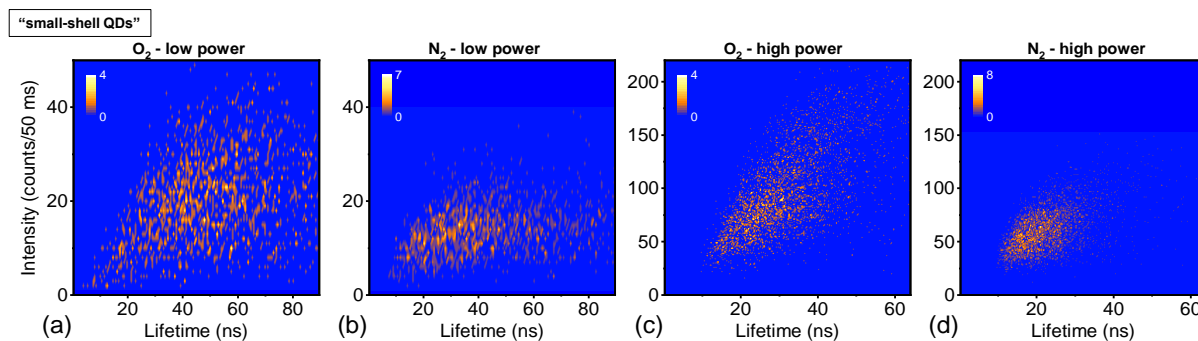


Figure 4.29: FLIDs for a single CdSe/CdS QD ($d = 9.1$ nm) in O_2 and N_2 at low (0.07 excitons/pulse) and high (0.7 excitons/pulse) excitation powers. (a–b) FLIDs at low excitation powers in O_2 and N_2 . (c–d) FLIDs at high excitation powers in O_2 and N_2 . The underlying data are shown in Figure 4.27. Bin time: 50 ms.

blinking. The FLIDs in nitrogen, shown in Figure 4.29 (b, d), exhibit the events that are characteristic for trion emission, as the PL intensity stays in a low regime. Interestingly, at low excitation powers, also events with long lifetimes are observed, whereas at high excitation powers the lifetimes are distributed more narrow. This might indicate the occurrence of additional processes at low excitation powers, which are suppressed at high excitation powers, at which trion emission is more dominant. Elongation of PL lifetimes without change in the PL intensity, as shown in Figure 4.29(b) has previously been attributed to the quantum-confined Stark effect (QCSE) due to surface charges.¹⁹¹ But the narrowing of the lifetime distribution could also result from the formation of multiexcitons at higher excitation powers that shift the average lifetimes to lower values.

Similar as for the "big-shell QDs", the ratio of the radiative lifetimes of the bright and the dim state are calculated according to Equation 2.21. Again, the thresholds are used that are marked in Figure 4.27 to compare the bright states with the dim states. At low excitation powers, the radiative lifetime scaling factor in oxygen is 0.6, and for nitrogen a factor of 0.5 was determined. These values of below one indicate hot-carrier blinking. In hot-carrier blinking, non-radiative recombination occurs without affecting the radiative recombination process. This leads to detection of events with low intensity, but lifetimes that are still on the level of the events of high intensity. Thus, the increase of the lifetime of the events detected in the dim state leads to a reduction of the calculated radiative lifetime ratio. Even though the calculations technically do not yield the ratio of the radiative lifetimes when hot-carrier blinking is present, the results can still be used to estimate the blinking mechanism as discussed.

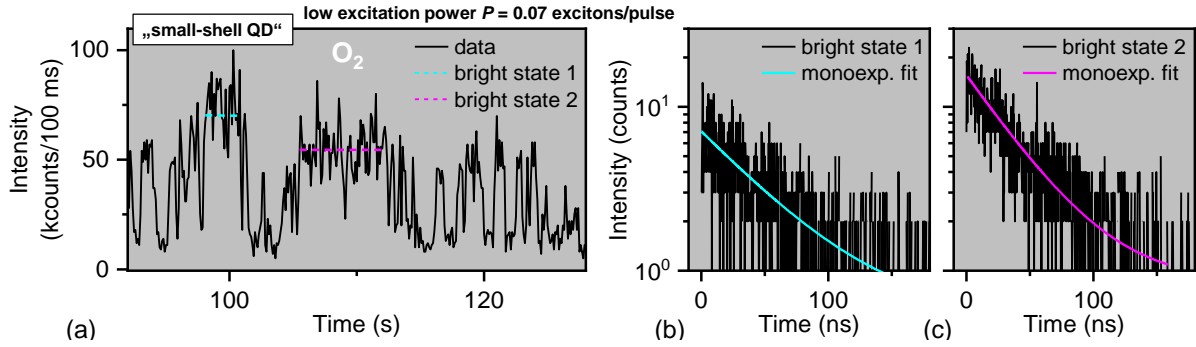


Figure 4.30: Blinking analysis of a representative single CdSe/CdS QD ($d = 9.1$ nm) in O₂ at low excitation power (0.07 excitons/pulse). (a) Extract of the PL intensity time-trace of Figure 4.27(a), exhibiting two periods of "bright states" with different intensities. (b) PL decay-curve of data points of "bright state 1". (c) PL decay-curve of data points of "bright state 2". Both decay curves are fitted monoexponentially. $\lambda = 405$ nm, $f = 1$ MHz.

Furthermore, the determination of radiative-lifetime scaling factors of below one for these data suggest that Auger blinking does not have a substantial impact on the optical properties of the QDs at low excitation power.

The presence of bandedge-carrier blinking, however, can still be found by investigating the PL time-trace of "small-shell QDs" in oxygen at low excitation powers in more detail. Figure 4.30(a) shows an extract of the PL intensity time-trace of Figure 4.27(a). In the "bright state" two periods can be determined, in which the intensity remains on an almost constant level for a couple of seconds. The respective PL decay-curves can be fitted monoexponentially, as shown in Figure 4.30(b,c). For those two states the ratio of radiative lifetimes is

$$\frac{\tau_r(X_1)}{\tau_r(X_2)} = \frac{\tau(X_1) I(X_2)}{I(X_1) \tau(X_2)} = \frac{53 \text{ ns}}{(71 - 8) \text{ cnts}/100 \text{ ms}} \frac{(55 - 8) \text{ cnts}/100 \text{ ms}}{39 \text{ ns}} = 1.0,$$

with the intensities $I(X_1) = 71$ cnts/100 ms, $I(X_2) = 55$ cnts/100 ms, $I_{\text{background}} = 8$ cnts/100 ms and the lifetimes $\tau_1 = 53$ ns, $\tau_2 = 39$ ns. The scaling factor of one for the radiative lifetimes in the extracted time periods demonstrates the presence of bandedge-carrier blinking. Therefore, the evaluation of the radiative lifetime scaling of "small-shell QDs" in oxygen suggests both bandedge-carrier and hot-carrier blinking being involved in the recombination dynamics.

In summary, for the "small-shell QDs" in oxygen, the analysis of the FLIDs and the radiative lifetime scaling reveals features originating from bandedge-carrier blinking, as well as hot-carrier blinking, while characteristics of Auger blinking, such as a scaling factor of two, were not found. These observations might appear surprising, since in the

nitrogen atmosphere, the emission of a dim state that is usually assigned to trion emission, is observed almost exclusively.^{20,148,149} This might intuitively lead to the conclusion that the blinking mechanism is governed by Auger recombination. However, at low excitation powers, no radiative lifetime scaling factors >1 were observed, neither in oxygen nor nitrogen atmospheres, which would indicate the presence of Auger blinking. In contrast, radiative lifetime scaling factors of approximately 0.5 were found. While trion emission might still be relevant at high excitation powers, at low excitation powers hot-carrier blinking seems to play a dominant role.

For the data of the "small-shell QD" at high excitation power, the analysis of the radiative lifetimes cannot be performed in the same way. The decay curves of the bins considered as bright and dim state of the data in Figure 4.27(i,j) are fitted biexponentially. In contrast to the other data sets, it was not possible to place the thresholds at positions at which the decay curves could be fitted monoexponentially. The decay curves in Figure 4.27(i,j) exhibit steep components at the start of the decay, indicating the contribution of multiexcitons.¹⁹² The values of the radiative-lifetime scaling factors fluctuate significantly, depending on whether the recombination of the biexcitons is neglected or included. In addition, the values are affected by the method of calculating the average lifetime, as either the amplitude-weighted or the intensity-weighted lifetime can be considered. These factors inhibit a reasonable analysis of the radiative-lifetime scaling for the "small-shell QD" at high excitation power.

However, considering the observation of hot-carrier blinking and bandedge-carrier blinking for the "small-shell QD" at low excitation power, along with the occurrence of Auger blinking (of negative trions) in the "big-shell QD" at high excitation power, it is reasonable to assume that all of these processes occur in the "small-shell QDs" at high excitation power. The increase in the PL intensity in oxygen, observed in the single-dot experiment, as well as in the ensemble measurement, suggests that the negative trions in a nitrogen atmosphere and the deionization in an oxygen atmosphere are the primary processes in the "small-shell QDs" at high excitation power.

At this point, the conclusions are summarized in a proposed model that is illustrated in Figure 4.31. For the "big-shell QDs" at low excitation powers in Figure 4.31(a), emission of neutral excitons is observed in both nitrogen and oxygen atmospheres. Figure 4.31(b) shows the recombination patterns for the "small-shell QDs" at low excitation powers. In the absence of oxygen, hot holes get trapped at negatively charged sites on the surface and recombine non-radiatively with the electrons. Thus, characteristics of hot-carrier blinking are observed in nitrogen atmosphere. In oxygen atmospheres a new channel of recombination is opened. Since oxygen acts as electron acceptor, molecules adsorbed at the surface can provide a trapping site for bandedge electrons that then undergo non-

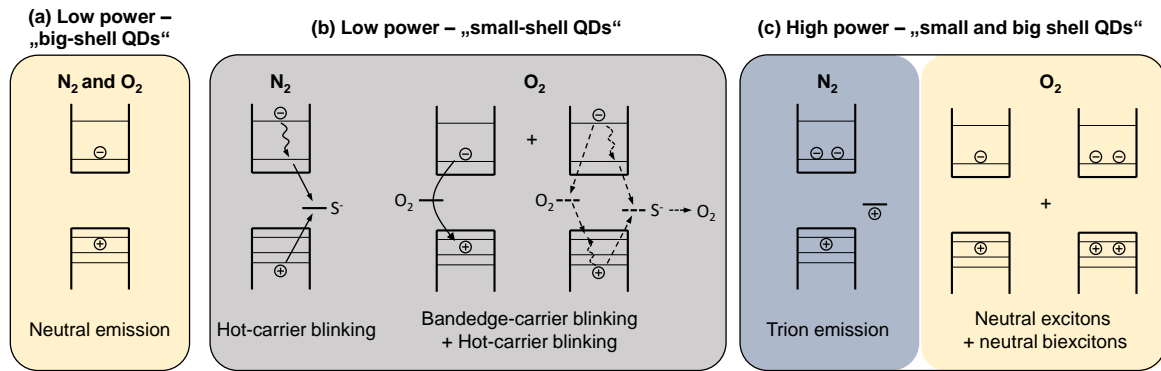


Figure 4.31: Scheme of the dominant recombination patterns in "big- and small-shell QDs" in oxygen and nitrogen atmospheres. (a) At low excitation powers, the "big-shell QDs" exhibit emission of neutral excitons in both oxygen and nitrogen atmospheres. (b) At low excitation powers, the "small-shell QDs" exhibit characteristics of hot-carrier and bandedge-carrier blinking. While hot-carrier blinking is dominant in nitrogen, in oxygen bandedge-carrier blinking is also observed. Hot-carrier blinking may be partially inhibited by passivation of hole traps by oxygen, while oxygen itself may act as a trap site for hot electrons (dashed arrows). (c) At high excitation powers in both "small- and big-shell QDs" multiexcitons are involved. In nitrogen, negatively charged trions are formed, while neutral species are obtained in oxygen. While for "big-shell QDs" the drawn states are dominant in each atmosphere, for the "small-shell QDs" in oxygen strong fluctuations between those states occur.

radiative recombination, thus introducing characteristics of bandedge-carrier blinking. As electron acceptors, oxygen molecules might also passivate the negative surface charges that act as trapping sites for hot holes.⁹¹ This could explain the overall higher intensity in oxygen, observed for the single dot in Figure 4.27. Yet, the radiative lifetime scaling factor of <1 suggests that hot-carrier blinking is not fully inhibited. In fact, trapping of hot charge carriers might still occur with adsorbed oxygen at the surface as trapping site. Both trapping of hot electrons by oxygen, as well as passivation of negatively charged trap sites (S^-) are sketched in Figure 4.31(b) on the right side.

These findings provide new insights for the explanation of the findings for the ensemble measurements of the "small-shell QDs" (see Figure 4.25), in which lower intensities were observed in oxygen with the lifetimes remaining constant. While the mean PL intensity in the single-particle measurement (Figure 4.27) is enhanced in oxygen, the PL quenching in the ensemble experiment suggests that for the majority of QDs the addition of centers for non-radiative recombination by oxygen has a larger impact than the passivation of defect sites. In the ensemble measurement, it is not possible to distinguish whether the number of emitting particles or the blinking is changing. The single-particle measurement

shows that the blinking does change, but that hot-carrier blinking, which was considered a possible explanation for PL quenching by oxygen in the ensemble measurement, also occurs primarily in nitrogen. The second possible explanation for the PL quenching in the ensemble measurement is the reduction of the number of emitting particles by oxygen. However, other processes in ensemble measurements, which are naturally not present in single-dot experiments, such as electron migration between particles, might also affect these results.

Figure 4.31(c) illustrates the states of recombination for "small- and big-shell QDs" at high excitation powers. Due to the formation of multiexcitons, Auger blinking might have a larger effect than for low excitation powers. In the absence of oxygen trion emission occurs. In oxygen, the PL is dominated by the emission of neutral excitons and biexcitons. For the "big-shell QDs" this accounts almost exclusively (very rare fluctuations), while for the "small-shell QDs" in oxygen strong fluctuations occur.

Further insights in the recombination mechanisms might be yielded by the analysis of the statistics of the blinking events that will be conducted in the following section.

On/Off-time Statistics

In the literature, usually the first step in investigating the blinking statistics is to investigate the distributions of the on- and off-time durations. Figure 4.32 shows the cumulative distributions of the durations of the on- and off-state for the "small-shell QDs" in oxygen and nitrogen at low and high excitation powers, respectively. All distributions show a linear progression in a double logarithmic plot. Therefore, the distributions follow a power law, described in Equation 2.22. As discussed in Section 2.3.2, the power-law dependence of the on- and off-times is evidence for the fluctuation of the rates of either trapping and detrapping of charge carriers, or non-radiative relaxation processes. The power-law exponents $m_{\text{on/off}}$ lie between -1.13 and -2.05, which is in good agreement with values reported in the literature.¹⁹³ At low excitation powers in Figure 4.32 (a–b) the difference of the atmosphere on the blinking statistics is apparent, since large shifts in the respective power-law exponents are observed. The change of m_{on} from -1.31 to -2.05 and from -1.67 to -1.14 for m_{off} when switching the atmosphere from oxygen to nitrogen reflects the observation that the QDs exhibit extensive PL blinking in oxygen, while they stay mostly in the off/dim state in nitrogen. In oxygen, longer on-times are more likely, resulting in a lower slope of the distribution than in nitrogen. The opposite accounts for the slopes of the off-time distributions, since shorter off-times are more likely. The on- and off-time distributions at higher power in Figure 4.32(c–d) are also governed by a power law. The independence of this phenomenon from the excitation power is in agreement with the literature and highlights its general validity.¹⁵²

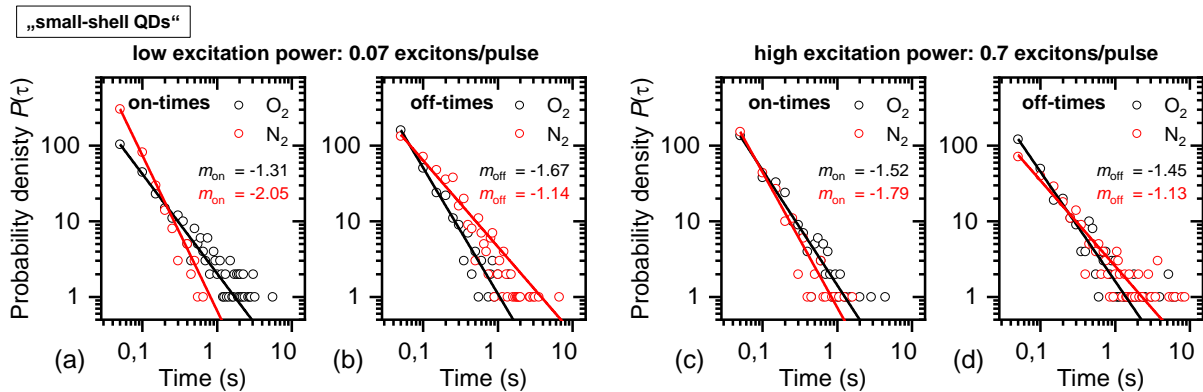


Figure 4.32: Distributions of the time periods for on- and off-states of single CdSe/CdS QDs ("small shell": $d = 9.1$ nm) in O_2 and N_2 at low (0.07 excitons/pulse) and high (0.7 excitons/pulse) excitation powers. (a–b) On- and off-times at low excitation powers in O_2 and N_2 . (c–d) On- and off-times at high excitation powers in O_2 and N_2 . The underlying data are shown in Figure 4.27. A bin time of 50 ms was used and the thresholds were set at the overlap of the two Gaussians that were applied to represent each histogram. For simplicity, it was not differentiated between an off-state and a dim state.

The changes of the power-law exponents with changing atmospheres show that the distribution function of the on- and off- times, thus the trapping and detrapping rates, are actually changing. In agreement with the analysis conducted earlier, the change of the power-law exponents indicate that the blinking mechanism is indeed changing with the atmosphere. Thus, the analysis of the on- and off-time distributions is an additional tool, supporting the analysis of the time traces and lifetimes.

The data analysis made so far has some limitations, especially concerning fast events. As all methods involve time binning some information might be hidden or obscured. For the representation of the time traces with bin times of 100 ms, as well as for the FLIDs and the probability densities with bin times of 50 ms, blinking events that are faster than the selected bin time will not be displayed. Moreover, the distributions for the on- and off-time duration depend on the threshold value, set in the time trace. In this study each threshold was set at the overlap of the Gaussians that were applied to fit the histograms. However, there is some room for error in the initial fitting and the overlap levels can vary at different bin times. For the data of the "big-shell QDs" this method fails completely, as no distinct on- and off-levels are identified. To address these problems, the autocorrelation functions are examined. Autocorrelation analysis can be used to investigate fluctuations of a signal with much smaller time binning.

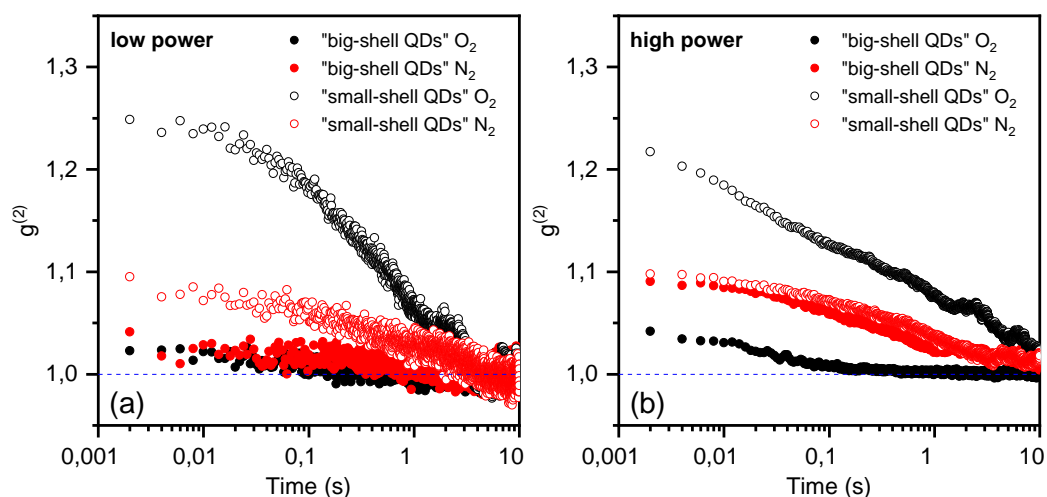


Figure 4.33: Autocorrelation functions for single "small-shell" and "big-shell" CdSe/CdS QDs in O₂ and N₂. (a) Autocorrelation functions at low excitation power (0.07 excitons/pulse). (b) Autocorrelation functions at high excitation power (0.7 excitons/pulse). The underlying data are shown in Figure 4.26 and 4.27.

Autocorrelation

Figure 4.33 shows the autocorrelation functions of both "small-shell" and "big-shell" QDs. $g^{(2)}$ was calculated according to equation 2.23. The slope of the decay of the autocorrelation data and the offset of $g^{(2)}$ in respect to $g^{(2)} = 1$ correlate with the number of fluctuation events, as discussed in Section 2.3.2. In general, large numbers of fluctuation events lead to larger offsets of $g^{(2)} > 1$ and thus larger slopes in the autocorrelation. Figure 4.33(a) depicts the autocorrelation functions at low excitation powers. For the "big-shell QDs" the slopes of the functions are quite small and independent of the atmosphere. In contrast, the autocorrelation functions of the "small-shell QDs" exhibit larger slopes and large deviations between both atmospheres are apparent. Especially in oxygen, $g^{(2)}$ reaches relatively large values of 1.25 at times of 2–10 ms.

In the PL time-traces of the "big-shell QDs" at low excitation power (see Figure 4.26(a,d)) almost no fluctuations are observed. This is confirmed by the small slopes of the autocorrelation functions and values of $g^{(2)} \approx 1$. However, the intensity time-trace for the "small-shell QDs" at low excitation power in nitrogen, shown in Figure 4.27(d), suggests that the QD is dominantly in the dim state, while rare fluctuations to the on-state are observed. The quantity of those fluctuations, plus events that were too fast to be visible in the time trace, are reflected in the increased slope of the autocorrelation function and higher values of $g^{(2)}$ than for the "big-shell QDs". In oxygen, the large amount of blinking, observed in the time trace in Figure 4.27(a), expresses itself unambiguously

in the autocorrelation function, which has a significantly larger offset and larger slope at times of 0.02–1 s.

Figure 4.33 (b) shows the autocorrelation functions at high excitation powers. For the "small-shell QDs", a similar trend is observed when comparing the slopes in both atmospheres as for the measurements with low power. Higher values of $g^{(2)}$ are observed in oxygen than in nitrogen. In comparison to the data at low excitation power, the slopes in nitrogen are quite similar, whereas the function in oxygen contains an additional step at times of 20–200 ms. Likewise, for the "big-shell QDs" there is an even more pronounced step in the same time range. Strikingly, the values for $g^{(2)}$ are only elevated at lower times and approach one at times higher than 100 ms. What is also surprising is that $g^{(2)}$ exhibits larger values in nitrogen than in oxygen for the "big-shell QDs" at high excitation power.

At high excitation powers, fluctuations in the PL intensity are observed for each system leading to elevated values of $g^{(2)}$ in all autocorrelation functions. The aforementioned steps in the autocorrelation function for the "small-shell QDs" in oxygen indicate the presence of PL fluctuations on both low and high time scales, which corresponds to the observation in the PL intensity time-trace in Figure 4.27(g). When comparing the PL intensity time-traces of the "big-shell QDs" at high excitation powers in both atmospheres in Figure 4.26(g,j), it becomes clear that the PL switches occasionally to the on-state in nitrogen, while being mostly in the dim-state, whereas in oxygen far less fluctuations are observed. This is mirrored in the higher values of $g^{(2)}$ in nitrogen compared to in oxygen. Furthermore, the autocorrelation function of the "big-shell QDs" at high excitation power in oxygen reveals bunched photons at time scales below 100 ms, which were concealed in the PL time-trace in Figure 4.26(g), as the bin time was set on 100 ms. Especially the step in the autocorrelation function at ≈ 10 ms shows the occurrence of fluctuations with time periods in that range.

In summary, some aspects of the data of the PL intensity time traces of Figure 4.26 and 4.27, such as the quantity of fluctuations, are shown more precisely in this representation. Further, processes have been revealed that were obscured due to binning. Especially, the observation of fast fluctuations of the PL intensity of "big-shell QDs" in oxygen at high excitation powers could only be evaluated to some extent in the time trace (see Figure 4.26(g)), but becomes very clear by the step in the autocorrelation function in Figure 4.33(b). The analysis of the FLIDs and radiative lifetime scaling of this data set suggested the presence of a mixture of neutral single and biexcitons. This, as well as fast blinking events between neutral emission of biexcitons and emission of negative trions might be reflected in the step in the autocorrelation function. As final step to improve

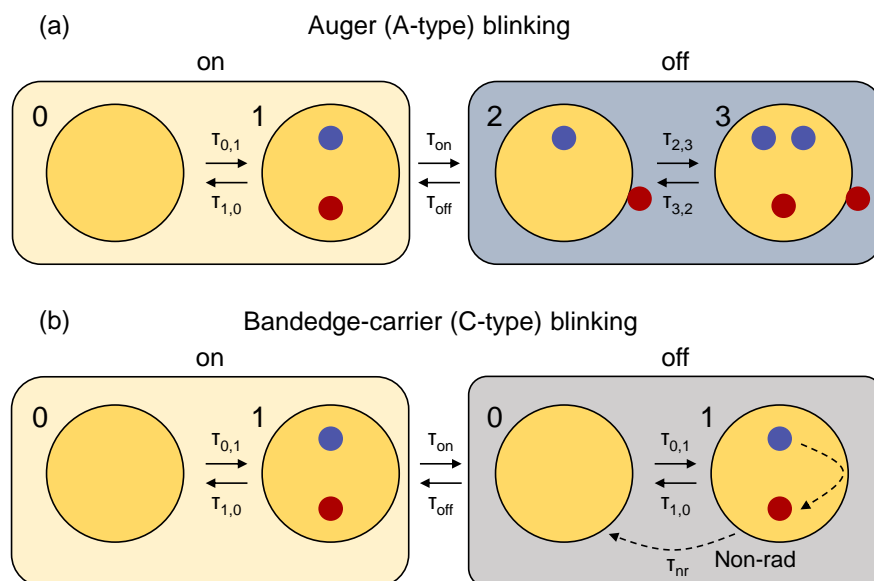


Figure 4.34: Scheme for MC simulations. Electrons and holes are represented by blue and red dots. (a) Auger (A-type) blinking. The states 0 – 3 are defined as follows: 0: QD is not excited. 1: Single neutral exciton. 2: One charge carrier is trapped. 3: Charged trion. (b) Bandedge-carrier (C-type) blinking. The system switches only between state 0 and 1, while a non-radiative recombination channel with fluctuating rates from state 1 to state 0 is implemented. Characteristics of hot-carrier (B-type) blinking should be gained by implementing fluctuating values for $\tau_{0,1}$ instead.

the understanding of the processes observed for the QDs investigated in this work, Monte Carlo (MC) simulations were conducted.

Comparison to Monte Carlo Simulations

The analysis of the PL fluctuations conducted so far, demonstrates that it is not easy to gain information about the system from the experimental data directly. Creating artificial time traces of a known model system that can be used for comparison provides great potential to link the information present in PL intensity fluctuations with underlying processes. To compare the measured data with data sets obtained with known parameters, Monte Carlo (MC) simulations were performed. The simulations model the time-dependent emission of each individual photon to generate a flux of emitted photons. The simulated data sets were created using a MATLAB script written by Christian Strelow. In general, the switching between states is calculated on the basis of random numbers with certain probabilities. Data points are generated according to the scheme shown in Figure 4.34(a). Starting in stage 0, the excitation of an exciton is simulated by implementing an excitation probability. If the system transitions to stage 1, the next

step may result in an emitted photon due to radiative recombination occurring at an experimentally determined rate. On the other hand, the system can go into the off-state by charge-carrier trapping. Running this simulation in multiple cycles produces a series of events that correspond to the measured data of emitted photons in a real QD, exhibiting Auger blinking. Since this analysis was conducted before performing the extensive discussion about the intensity-lifetime scaling, the calculations were performed based on the Auger-blinking mechanism. A scheme for a system exhibiting bandedge-carrier blinking is illustrated in Figure 4.34(b). There, a non-radiative recombination channel from stage 1 to stage 0 with fluctuating rates is added (dashed arrow). To simulate hot-carrier blinking, fluctuating values for $\tau_{0,1}$ should be implemented. This simulates the trapping and non-radiative recombination of charge-carriers that do not relax to the bandedge, which is analogous to a fluctuating excitation rate.

So far, however, calculations were performed according to the Auger mechanism. The results are shown as an example in Figure 4.35. The following parameters were used for the calculations. For $\tau_{1,0}$ and $\tau_{3,2}$ the average lifetimes of the bright and dim state, as determined from the data of the "small-shell QDs" in oxygen at low excitation powers, were implemented ($\tau_{1,0} = 50$ ns and $\tau_{3,2} = 15$ ns). τ_{on} and τ_{off} represent the reciprocals of the transition rates for ionization and neutralization. As discussed in Section 2.3.2, those rates are not constant, but can be described by a range of rates that are exponentially distributed. According to the model proposed by Kuno et al.,¹⁹⁴ on- and off-durations can be expressed as

$$\tau_{on} = \tau_{1,2} \cdot e^x \quad (4.2)$$

and

$$\tau_{off} = \tau_{2,1} \cdot e^{x'}, \quad (4.3)$$

with pre-exponential factors $\tau_{1,2}$ and $\tau_{2,1}$, and x and x' as stochastic variables. The normalized distributions of x and x' are given by

$$L(x)_{on} = \alpha_{on} \cdot e^{\alpha_{on}x} \quad (4.4)$$

and

$$L(x')_{off} = \alpha_{off} \cdot e^{\alpha_{off}x'}, \quad (4.5)$$

while the power-law coefficient $\alpha_{on,off}$ was set to -1.5.¹⁹⁴

Calculations were performed with varying values for $\tau_{1,2}$ and $\tau_{2,1}$, while the examples shown here are the ones that approach the experimental data the closest.

Figure 4.35 shows two exemplary data sets generated via the MC method. The PL intensity time-trace in Figure 4.35(a) exhibits a high amount of fast fluctuations (flickering)

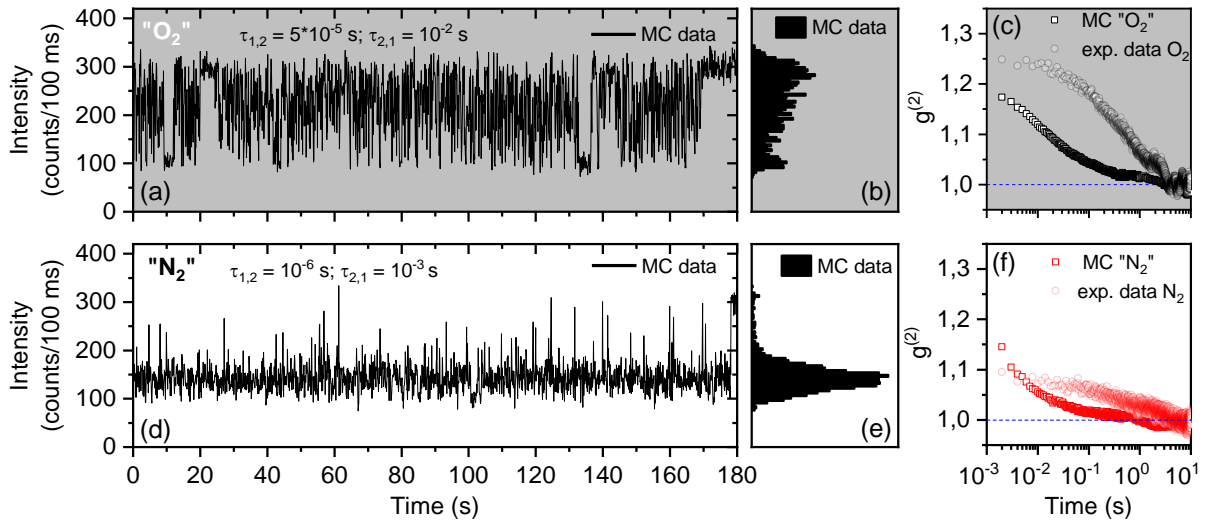


Figure 4.35: Results of Monte Carlo (MC) simulations to recreate the data of "small-shell QDs" at low excitation powers (see Figure 4.27). First row: Results to represent the data in O_2 . Second row: Results to represent the data in N_2 . (a,d) Simulated PL intensity time-traces. (b,e) Histograms. (c,f) Autocorrelations of simulated and experimental data (bin time: 2 ms).

with some longer periods in the bright/dim state. The histogram in Figure 4.35(b) shows a bi-modal distribution of the intensities with a large fraction of events that are located in between bright and dim state as the switching is faster than the bin time (100 ms) chosen for this representation. The data set approximates the experimental data in Figure 4.27(a) and the intensity flickering occurs with a similar frequency. Small deviations still occur, as the intensity distribution is shifted to higher intensities, with respect to the experimental data. Figure 4.35(c) shows the autocorrelation of the simulated time trace in comparison to the respective experimental data of Figure 4.33(a). The offset of $g^{(2)}$ in respect to $g^{(2)} = 1$ at small times is slightly lower in the simulated data than in the experimental data. However, a larger deviation is given by the shape of the autocorrelation, as $g^{(2)}$ of the experimental data rises at higher times and exhibits a plateau at small times. In contrast, the simulated values increase at shorter times.

Figure 4.35(d) shows a time trace that is similar to the data obtained in inert gas atmosphere. The PL intensity remains mainly in the dim state, while occasional fluctuations to a bright state occur. The resulting histogram in Figure 4.35(e) obtains one peak that is slightly broadened to higher intensities. Both time trace and histogram are in good agreement with the experimental data shown in Figure 4.27(d,e). Figure 4.35(f) shows the autocorrelations of the simulated data in comparison to the experimental data of Figure 4.33(a). The offsets of $g^{(2)}$ in respect to $g^{(2)} = 1$ at low times lie in similar ranges. Yet, the shape of the two autocorrelations are different. For the experimental data the values

of $g^{(2)}$ reach saturation at low times, while the slope of the simulated autocorrelation gets steeper at that point and the rise of the slope starts at lower times.

The results of the simulations show that the experimental data can almost be recreated by adjusting the probabilities to switch between bright and dim state. The general trend of extensive flickering in oxygen atmosphere versus a dominating dim state in nitrogen atmosphere can be represented with the applied model. However, some deviations still occur, which is especially highlighted by the additional data representation, the autocorrelation. The different shape of the autocorrelation suggests discrepancies between the mechanism behind the simulated and the experimental data, which agrees with the analysis of the blinking statistics discussed in the previous sections. Preliminary data of simulations employing bandedge-carrier blinking and hot-carrier blinking show promising results to represent the experimental data more accurately, thus highlighting the potential of this method for the analysis of PL blinking. However, the detailed elaboration of these additional simulations is beyond the scope of this thesis.

5 Summary

In this work, the effect of the chemical environment on the optical properties of semiconductor nanostructures was investigated. In the first part, colloidal CdSe QWs were synthesized and examined. The investigations focused on the effect of oxygen on the PL and Raman properties. One goal was to elucidate the mechanism behind oxygen-induced photobrightening, as well as the description of the reversible effects of oxygen. In the second part, CdSe/CdS core-shell QDs were examined with regard to the effect of oxygen on their PL properties. In that part, the investigations focused on PL blinking.

CdSe QWs were synthesized via the SLS method. In order to gain a better understanding of the wire composition and their surface properties some analytic investigations were conducted. By EDX spectroscopy and ICP-MS it was found that the wires exhibit a small excess of Se in regard to Cd. To investigate the ligand shell, FTIR spectroscopy was used. The analysis of the FTIR spectra during the purification process and the results of coupled FTIR-TGA experiments suggest that the majority of the ligand shell is composed of the X-type ligand DOPA. In combination with the EDX and SEM data, those results lead to the conclusion that the wire surface contains unpassivated Se. The PL properties of CdSe QWs were examined by confocal spectroscopy. By using gas-exchange setups or flow-channels, the surroundings of the QWs could be exchanged while examining the same individual nanostructures. The investigation of the effects of oxygen revealed irreversible and reversible effects. Oxygen-induced photobrightening, during which the PL intensity increases two- to threefold and the emission wavelength shifts to the blue, was found to be irreversible when both stopping the illumination and changing the atmosphere to inert gas. The combination of reports about photooxidation of CdSe NCs in the literature, with the experimental findings in this work led to the elucidation of the mechanism for the oxygen-induced photobrightening of CdSe QWs. Unpassivated Se ions at the surface can act as hole traps, thus resulting in an excess of negative charges upon illumination. In this state, non-radiative recombination, for example via the Auger mechanism, is very likely and the PL intensity is partially quenched. Since oxygen can act as an electron scavenger, the excess electrons can be removed, which increases the charge balance and results in a higher PL intensity. The irreversible character of this process suggests the formation of oxides, such as SeO_2 . The subsequent irreversible PL quenching is assigned to

further degradation of the structure due to further photooxidation. In addition, reversible changes in the emission spectra were observed when changing the gases during continuous illumination. Additional blue-shifted emission in inert gas atmospheres was assigned to the emission of higher excited states due to excess negative charges. In accordance with findings in the literature for CdSe NCs, those observations were assigned to electron scavenging by oxygen. The conclusions were confirmed by the investigations of the Raman spectra, where especially shifts of the LFS could be correlated with changes in the PL properties. This correlation strategy provides a broadly applicable tool for investigating surface-related photoinduced effects of nanostructures.

Further investigations for the CdSe QWs, concerning the effects of other substances, such as H₂O, Cd(Ac)₂ (aq.) or AgNO₃ (aq.), reflected some findings that were already reported for CdSe NCs. For gaseous *n*-propylamine, the evolution of the spectra suggests that electron injection by this L-type ligand leads to the emission of charged multiexcitons, similar to the emission in inert gas atmospheres at high excitation powers.

For the effect of oxygen on the PL of QDs contradicting reports are found in the literature, as both reversible quenching and enhancement of the PL intensity was observed.^{18,20} To clarify this topic, CdSe/CdS QDs with varying shell diameters (3.2 – 9.6 nm) were examined. By conducting ensemble measurements with changing gas-atmospheres PL enhancement was observed in oxygen in all samples. However, this only applied after overcoming an excitation-power threshold. For QDs with large shells, no effect occurred at low excitation power, while the opposite, a PL quenching effect in oxygen, was observed for QDs with thin shells. Single-particle measurements indicate that for the "big-shell QDs" multiexcitons have to be produced, in order to observe an effect of oxygen on the PL. In this case, oxygen acts as an electron acceptor, inhibiting the formation of charged particles. For the "small-shell QDs" the PL blinking was analyzed and while no features of Auger-blinking were found, the intensity fluctuations were assigned to bandedge-carrier and hot-carrier blinking events. Further, the data suggest that the presence of oxygen suppresses hot-carrier blinking events, but enables bandedge-carrier blinking. The results of both ensemble and single-particle measurements can be explained by a model in which oxygen, adsorbed at the QD surface, can act as center for non-radiative recombination, but also as passivating agent. In order to confirm the analysis, the experimental data were compared to data obtained by Monte-Carlo simulations. First results confirm the original evaluation and highlight the potential of this strategy to solve complex problems. In summary, the seemingly contradicting reports in the literature,^{18,20} were both confirmed and clarified. The ambivalent effects of oxygen on the PL properties result in a high dependence of the observations on the excitation power and on the particle system itself.

6 Experimental Procedures

6.1 Chemicals

The chemicals used for the experiments of this thesis, if applicable with purity and manufacturer or supplier are summarized in Table 6.1. All chemicals were used without further purification.

Table 6.1: List of the chemicals used for the experiments in this work.

Chemical	Molecular Formular	Supplier
Acetone	C_3H_6O	Own house (99.8%)
Argon	Ar	Westfalen (5.0)
Cadmium acetate	$C_4H_6CdO_4$	Th. Geyer (99.999%)
Di- <i>n</i> -octylphosphinic acid	$C_{16}H_{35}O_2P$	–
Hexane	C_6H_{14}	Own House (99%)
Hydrochloric acid (37%)	HCl	FischerScientific
Isopropanol	C_3H_8O	Own house (99.7%)
Methyl viologen dichloride hydrate	$C_{12}H_{14}Cl_2N_2$	Sigma Aldrich (100%)
Nitric acid	HNO_3	Fluka (99%)
Nitrogen	N_2	Linde (5.0)
Octadecene	$C_{18}H_{36}$	Sigma Aldrich (90%)
Oxygen	O_2	Westfalen (99.5%)
<i>n</i> -Propylamine	C_3H_9N	Acros Organics (99%)
Selen	Se	Thermofischer (99.5%)
Silver nitrate	$AgNO_3$	Sigma Aldrich (100%)
SYLGARD 184 silicone elastomer kit	–	Sigma-Aldrich
Toluene	C_7H_8	Grüssing (99.5%)
Tri- <i>n</i> -octylphosphine	$C_{24}H_{51}P$	Sigma-Aldrich (90%)
Tri- <i>n</i> -octylphosphine oxide	$C_{24}H_{51}OP$	Sigma-Aldrich (99%)

6.2 Synthesis of CdSe QWs

CdSe QWs were prepared according to the SLS method. The precursors used in the synthesis were prepared as follows.

Bi NPs were prepared according to the procedures described in ref. [115, 178]. The particles were prepared by Ann-Kathrin Sassnau. The precursor $\text{Cd}(\text{DOPT})_2$ was prepared according to a synthesis described in ref. [113]. For the preparation of the second precursor TOP:Se, Se was dissolved in TOP while stirring under nitrogen atmosphere for 24 h.

For the synthesis of the CdSe QWs, 32 mg (0.044 mmol) $\text{Cd}(\text{DOPT})_2$ were heated with 4 g TOPO under nitrogen to 100 °C. At this temperature, the mixture is dried for 1 h by applying vacuum and then heated to 300 °C under nitrogen while stirring. A mixture of 1.2 mL (0.030 mmol) TOP:Se (0.025 M) with 20 μL of the Bi-NP stock solution was injected at once, after which the colorless solution turned brown immediately. After three minutes, the reaction mixture was cooled down by removing the heat and 6 mL toluene were added once the temperature reached 100 °C. The reaction products were purified by repeatedly centrifugating at 11000 rpm for 20 min and redispersing in 3 mL toluene for three times.

6.3 Confocal Measurements

6.3.1 Setup

Throughout the thesis different confocal setups were used. The principle setup, however, is similar. Figure 6.1 depicts a sketch of the setup that was used most frequently. Differences in the other confocal setups used are noted in the next paragraph.

Depending on the experimental requirements, different excitation sources were chosen. For typical Raman, but also for PL measurements of CdSe QWs, a He-Ne gas laser (Meiling-Laser GmbH, $\lambda = 633 \text{ nm}$) was used. QD PL measurements were conducted using a pulsed laser-diode (ALS Germany, $\lambda = 405 \text{ nm}$). The laser light is directed with mirrors to the sample. A 50:50 beam splitter is used to direct half of the light on a photodiode to measure the excitation power, while the other half is directed to the objective. For measurements in ambient air typically an air objective (Zeiss, NA = 0.95, Epiplan-Apochromat 150x) was used, focusing the light directly on the sample, which is mounted on a piezo stage (Physik Instrumente, (x,y,z) range: 200x200x20 μm). Measurements in flowchannels were conducted using an oil objective (Zeiss, NA = 1.4, 100x) to excite CdSe QWs through the glass substrate. For measurements in the gas-flow setup an air objective with coverslip correction (Zeiss, NA = 0.75, 63 \times) was used. Reflected excita-

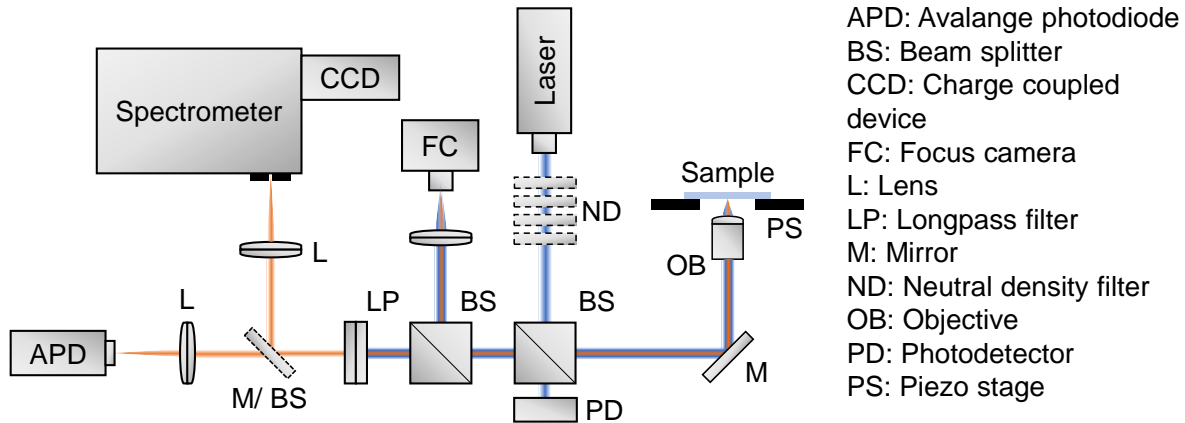


Figure 6.1: Sketch of the setup of a confocal laser scanning microscope. The laser power can be adjusted by neutral density filters. Part of the light is transmitted to a photodetector to measure the excitation power. The rest is directed to the objective, which focuses the light on the sample. Reflected excitation light and the emission are collected by the same objective and are directed to a second beamsplitter. A part of the reflection and emission is focused on a camera which is used to adjust the laser spot on the sample. The other part is filtered with a longpass filter to block the reflected excitation light. With either a mobile mirror or a beam splitter the emission is directed and focused on an APD and/or on a spectrometer with a CCD camera.

tion light and the emission are collected by the same objective and pass the first beam splitter before a second beam splitter directs 2% of the light on a camera, which gives feedback for adjusting the laser spot on the sample. The remaining part of reflection and emission is then filtered by a suitable longpass filter (633 nm or 430 nm), which blocks the reflected excitation light. The emission that passes the longpass filter can either be focused on an APD (PerkinElmer SPCM-14 for wires and ensemble-dot measurements; MPD (100 μm detector, PDM series) for single-dot measurements) for PL intensity and time-resolved measurements or on the entrance slit of a grating spectrometer mounted with a charge-coupled device (CCD) camera (Princeton Instruments PIXIS 400 B) for the detection of spectra. The emission was either directed on one of the detectors by a mobile mirror or on both simultaneously by a beam splitter, which directed 80% of the emission on the spectrometer and 20% on the APD. Single photon counting measurements were conducted using a time-correlated single photon counting (TCSPC) system (PicoQuant, PicoHarp 300) in the time-tagged time-resolved (TTTR) mode. The piezo scanner and photon counting are controlled by a real-time computer module (Jäger Messtechnik, ADwin gold).

Other Setups For the experiments with flow channels, a different setup was used with slight variations of the optical components and different devices. The setup was equipped with a laser diode (PICOQUANT PDL 800-D, $\lambda = 470$ nm), a micro photonics APD (MPD, PDM series) and a grating spectrometer (Princeton Instruments, Acton Research, SpectraPro 300i) with a CCD camera (Lavision, Imager QE).

For investigating the short lifetimes of CdSe QWs, a setup was used with a Ti:Sa laser system (Coherent Mira 900F; Pump laser: Finesse Pure, Laser Quantum, $\lambda = 532$ nm; Second harmonic generation: APE Harmonixx) and a streak camera (Hamamatsu).

6.3.2 Sample Preparation

Different types of sample preparation were used for the different types of measurements carried out in this thesis. The respective procedures are described in the following.

Cleaning of Substrates

For confocal measurements cover slides and Si substrates were used. Before use, both were cleaned according to the following procedure. Cover slides or Si substrates were successively treated with ultrasound in an acetone, isopropanol and (deionized) water bath, for each 20 min. The cover slides were placed in a Teflon holder for this procedure. Subsequently, the coverslides or substrates were dried at 80 °C.

CdSe Quantum Wires

Samples for ensemble measurements were prepared by dropcasting 5–10 μL of a undiluted or slightly diluted (1:10) suspension of CdSe QWs in toluene on a clean cover slide. Experiments were started once the solvent was evaporated. Samples for single particle measurements were prepared by diluting the suspension with toluene (1:50 – 1:100) and dropcasting 5 μL on a cover slide or on a Si substrate with lithographically produced markers for subsequent identification via SEM.

CdSe/CdS Quantum Dots

CdSe/CdS QDs were examined in thin films and as single particles. Thin films were prepared by slightly diluting the native suspension of QDs in hexane (1:20) and dropcasting 10 μL onto a cover slip mounted on a spin coater. Subsequently, the cover slip was rotated at 3000 rpm. For single-particle measurements, the native samples were strongly diluted (1:500,000–1:1,000,000) and 10 μL were dropcasted onto a rotating cover slip (3000 rpm) mounted on a spin coater.

6.3.3 Classic Confocal Measurement

In a typical experiment, at first large (100x100 μm) and then smaller PL scans (5x5–20x20 μm) were recorded to locate emitting nanostructures. Alternatively, especially for CdSe QWs, scans were recorded at low excitation powers without a longpass filter to locate wires by using the image of the reflected light while applying less excitation light to prevent photoinduced processes. The acquisition of data for a certain amount of time was gained by positioning the laser spot on a chosen spot in the respective scan.

6.3.4 Measurements with Varying Environments

Preparation of Flow Channels

For confocal measurements of nanostructures in controlled chemical surroundings, in particular in different aqueous solutions, PDMS flow-channels were prepared. A negative template that determines the dimensions of the flow channel was produced by using a 3D printer. The template was glued on a glass plate and a Teflon ring was used as vessel. PDMS was prepared with the Sylgard 184 silicone elastomer kit. For each flow-channel 4 g of the base material was mixed with 0.4 g of the linker material. After pouring the PDMS mixture over the template, air bubbles were removed by applying indirect vacuum. To accelerate the polymerization, the mixture was heated to 80 °C for 2 h in an oven. The hardened polymer was detached from the glass plate and a PDMS chip with the imprint of the template was obtained. To allow the attachment of tubes in the end, holes were drilled through the PDMS chip at the ends of the flow-channel imprint. To seal the channel with a cleaned cover slide (glass, diameter: 30 mm, thickness: No. 1 (0.13–0.16 mm), see Section 6.3.2 for cleaning procedure) oxygen plasma was applied for 1 min on both the cover glass and the PDMS chip, before pressing the PDMS chip on the glass slide. To allow an easy injection of the CdSe QW solution, a cannula was pierced through the PDMS chip in the channel. After attaching the tubes, 1.1 g of the PDMS mixture was poured on top of the flow channel and the chip was heated again to 80 °C for 2 h to seal the openings. An image of the 3D printed template and a sketch to show its dimensions are shown in Figure 6.2, together with images of a prepared PDMS chip and the experimental setup.

Measurements in Flow Channels

To conduct confocal measurements of CdSe QWs in flow channels, the CdSe QW solution (diluted or as prepared) was injected through the implemented cannula inside the flow channel until the glass surface was covered with solution. The PDMS chip was then stored overnight in a nitrogen atmosphere to allow the toluene to evaporate, before mounting

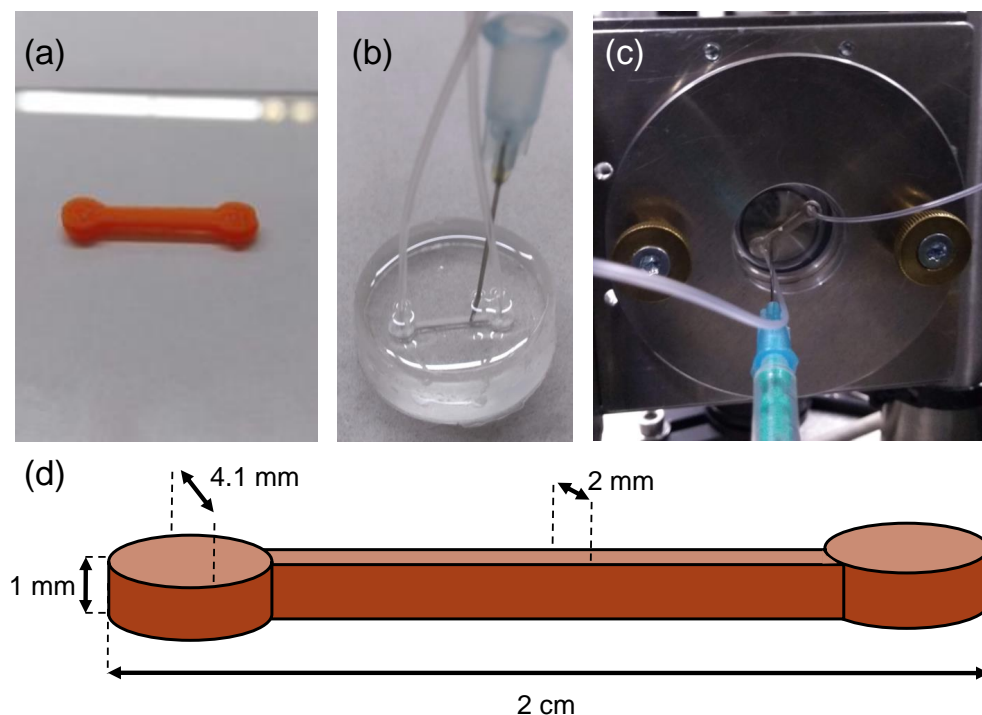


Figure 6.2: Flow channel preparation. (a) 3D printed template on a glass plate. (b) PDMS chip with integrated flow channel. The cannula is implemented for the injection of the CdSe QW solution. (c) Sample holder with a PDMS chip in a confocal setup with a horizontally aligned objective. (d) Sketch of the template to show the dimensions.

the chip on the sample stage. The sample was excited through the glass cover-slip at the bottom of the flow channel, as sketched in Figure 6.3(a).

In flow-channel experiments, the gas or aqueous solution was injected by using a syringe pump (Döring, Combimat 2000).

Measurements in the "Bottle Setup"

For experiments in which the gaseous surroundings of the sample had to be exchanged completely within a few minutes, the flow channel setup reached its limits. The most crucial part for all experiments with changing surroundings is the necessity of a completely stabilized system in order to avoid drifts of the sample during a measurement. In order to be able to illuminate a single structure while changing between oxygen and inert gas within a short time, a dedicated gas-flow setup ("bottle setup") was built. A sketch of the setup is shown in Figure 6.3(b). The respective gases were obtained from gas bottles or the in-house nitrogen gas line and the gas pressure was adjusted by standard pressure regulators. A three-way valve enabled rapid switching between the two gases. At the bottom the bottle was open, allowing the gas to pass the sample and objective while

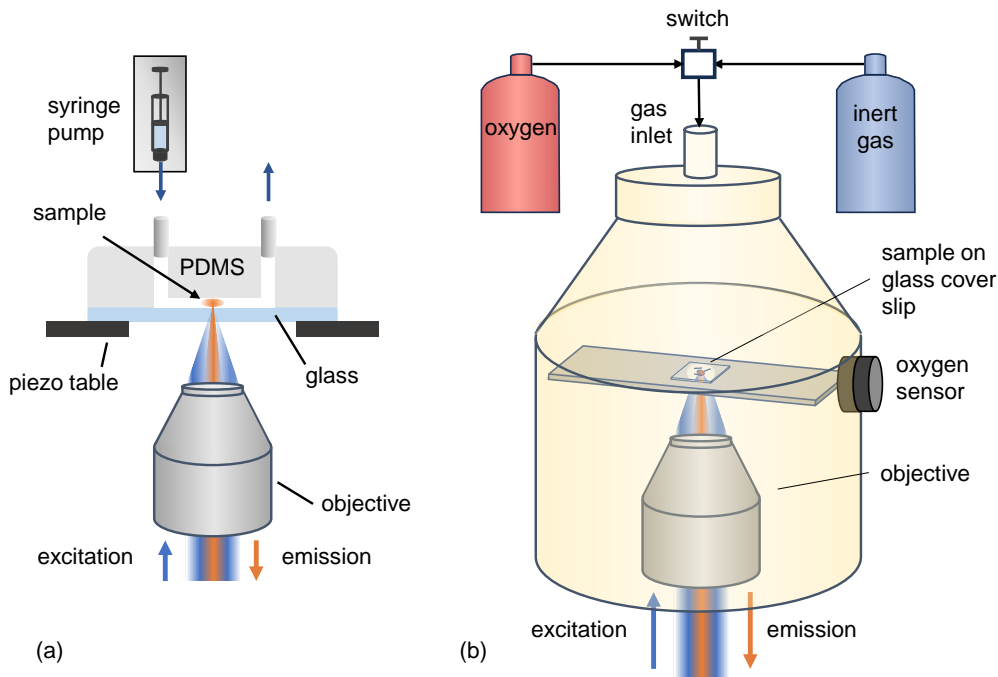


Figure 6.3: Sketched setups for measurements in different chemical environments. (a) Experiments with CdSe QWs in a controlled gaseous environment or in aqueous solutions were conducted in flow channels. The respective surrounding medium is controlled and changed by a syringe pump while the wires stick to the glass substrate, through which they are excited by laser light. (b) Experiments with controlled gaseous surroundings, in particular, if the gaseous surroundings needed to be exchanged quickly, were conducted in a "bottle setup". The respective gas is directed to the inlet of the 3D printed bottle, where it flows around the sample and exits at the open lower end. The oxygen content is measured with a sensor that is integrated in the bottle wall. Similar to the flow channel measurements, the QWs or QDs are excited through the glass substrate.

minimizing the mechanical stress on the glass cover-slip at the gas change. In contrast to the flow-channel setup which was only suitable for measurements with quite static conditions, such as a continuous flow, this setup enabled a fast exchange of gases with only minimal changes of the position of the focused laser spot on the sample. Small remaining shifts in the z -direction, induced by the brief reduction of the gas pressure when switching the gases were compensated via an automatic correction of the focus height.

The automatic correction, was controlled by a MATLAB skript. During the execution, the piezo stage was moved step-wise in z -direction while detecting the PL with an APD. The intensity curve obtained during the vertical movement was fitted with a Gaussian and the piezo stage was positioned according to the maximum of the intensity distribution.

6.4 Other Characterization Methods

TEM For the characterization of CdSe QWs via TEM, samples were prepared by drop-casting 5 μL of a diluted solution (1:1000) on a copper grid, covered with graphene. TEM images were recorded by Jannik Rebmann, Thomas Tsangas and Stefan Werner with a JEOL JEM 1011 microscope operating at 100 kV.

SEM SEM was used to identify single CdSe NWs after confocal experiments. For the sample preparation see Section 6.3.2. The SEM images were recorded by Charlotte Ruhmlied, using a Quanta 3D FEG microscope (FEI) operating at 20 kV.

EDX measurements For EDX measurements of CdSe QWs, 5 μL of the undiluted suspension were repeatedly dropcasted on a Cu substrate. The measurements were performed by Charlotte Ruhmlied with an EVO MA 10 microscope (Zeiss) at 22 kV and a scanning time of 180 s for each measurement, while conducting five measurements per spot on the sample.

FTIR spectroscopy FTIR measurements were performed by Jannik Rebmann using an Equinox 55 spectrometer (Bruker Optik) equipped with a Golden ATR system. The respective target substance was applied on the crystal without further preparation. For CdSe QWs, 5 μL of the suspension were repeatedly dropcasted on the crystal.

TGA-FTIR spectroscopy The TGA-FTIR measurements were performed by Uta Sazama in the Institute for Anorganic Chemistry in the group of Prof. Michael Fröba at the University of Hamburg. For all measurements the substances were loaded in a Al_2O_3 crucible mounted in the TGA instrument (Netzsch STA 409C/CD) and heated with a rate of 10 K/min to 650 $^\circ\text{C}$, while a nitrogen gas flow transported the evaporation products to a FTIR spectrometer (Bruker). For the analysis of the substances $\text{Cd}(\text{DOPT})_2$ and TOPO, 20 mg were loaded in the Al_2O_3 crucible. For the analysis of CdSe QWs ten batches of samples, produced in an identical way, were combined (to prevent possible alterations of the QW surface by a scale-up of the synthesis). In contrast to the usual procedure, the QWs were redispersed in hexane instead of toluene after the final purification step, to facilitate solvent evaporation. The unified suspension was dropcasted in the crucible, which was heated to 60 $^\circ\text{C}$ in a nitrogen gas flow. The TGA-IR measurement was performed with 31 mg CdSe QWs.

ICP-MS ICP-MS measurements of CdSe QWs were performed by Jili Han in the group of Prof. Wolfgang Parak at the University of Hamburg (Agilent Technologies series 7700).

For the sample preparation, 7 μL of the undiluted CdSe QW suspension were dried. The dried CdSe QWs were dissolved in 200 μL aqua regia overnight before 1.8 mL HNO_3 were added.

7 Bibliography

- (1) Ekimov, A. I.; Efros, A.; Onushchenko, A. A. *Solid State Communications* **1985**, *56*, 921–924.
- (2) Brus, L. E. *The Journal of chemical physics* **1984**, *80*, 4403–4409.
- (3) Brus, L. *The Journal of Physical Chemistry* **1986**, *90*, 2555–2560.
- (4) Murray, C. B.; Norris, D. J.; Bawendi, M. G. *Journal of the American Chemical Society* **1993**, *115*, 8706–8715.
- (5) NobelPrize.org The Nobel Prize in Chemistry 2023., 23.10.2023.
- (6) Pietryga, J. M.; Park, Y.-S.; Lim, J.; Fidler, A. F.; Bae, W. K.; Brovelli, S.; Klimov, V. I. *Chemical Reviews* **2016**, *116*, 10513–10622.
- (7) Sun, Y.; Jiang, Y.; Sun, X. W.; Zhang, S.; Chen, S. *Chemical record (New York, N.Y.)* **2019**, *19*, 1729–1752.
- (8) Peng, X.; Manna, L.; Yang, W.; Wickham, J.; Scher, E.; Kadavanich, A.; Alivisatos, A. P. *Nature* **2000**, *404*, 59–61.
- (9) Wang, F.; Dong, A.; Buhro, W. E. *Chemical Reviews* **2016**, *116*, 10888–10933.
- (10) Xu, H.; Akbari, M. K.; Zhuiykov, S. *Nanoscale Research Letters* **2021**, *16*, 94.
- (11) Jia, C.; Lin, Z.; Huang, Y.; Duan, X. *Chemical Reviews* **2019**, *119*, 9074–9135.
- (12) Cui, Y.; Zhong, Z.; Wang, D.; Wang, W. U.; Lieber, C. M. *Nano Letters* **2003**, *3*, 149–152.
- (13) Chan, C. K.; Patel, R. N.; O’Connell, M. J.; Korgel, B. A.; Cui, Y. *ACS nano* **2010**, *4*, 1443–1450.
- (14) Littig, A.; Lehmann, H.; Klinke, C.; Kipp, T.; Mews, A. *ACS applied materials & interfaces* **2015**, *7*, 12184–12192.
- (15) Steinhagen, C.; Akhavan, V. A.; Goodfellow, B. W.; Panthani, M. G.; Harris, J. T.; Holmberg, V. C.; Korgel, B. A. *ACS applied materials & interfaces* **2011**, *3*, 1781–1785.
- (16) Andrei, V.; Roh, I.; Yang, P. *Science Advances* **2023**, *9*, eade9044.

- (17) Lee, S. F.; Osborne, M. A. *Chemphyschem : a European journal of chemical physics and physical chemistry* **2009**, *10*, 2174–2191.
- (18) Koberling, F.; Mews, A.; Basché, T. *Advanced Materials* **2001**, *13*, 672–676.
- (19) Müller, J.; Lupton, J. M.; Rogach, A. L.; Feldmann, J.; Talapin, D. V.; Weller, H. *Applied Physics Letters* **2004**, *85*, 381–383.
- (20) Hu, Z.; Liu, S.; Qin, H.; Zhou, J.; Peng, X. *Journal of the American Chemical Society* **2020**, *142*, 4254–4264.
- (21) Nirmal, M.; Dabbousi, B. O.; Bawendi, M. G.; Macklin, J. J.; Trautman, J. K.; Harris, T. D.; Brus, L. E. *Nature* **1996**, *383*, 802–804.
- (22) Sun, Y.; Zhu, H.; Jin, N.; Chen, O.; Zhao, J. *The Journal of Physical Chemistry C* **2021**, *125*, 15433–15440.
- (23) Xie, M.; Tao, C.-L.; Zhang, Z.; Liu, H.; Wan, S.; Nie, Y.; Yang, W.; Wang, X.; Wu, X.-J.; Tian, Y. *The journal of physical chemistry letters* **2022**, *13*, 2371–2378.
- (24) Erwin Riedel, C. J., *Anorganische Chemie*, 8th ed.; De Gruyter: Berlin/New York, 2011.
- (25) European Chemicals Agency [https://echa.europa.eu/regulations/nanomaterials.](https://echa.europa.eu/regulations/nanomaterials), 13.04.2023.
- (26) Edvinsson, T. *Royal Society open science* **2018**, *5*, 180387.
- (27) Caruso, F., *Colloids and Colloid Assemblies: Synthesis, Modification, Organization and Utilization of Colloid Particles*, 1st ed.; Wiley-VCH: Weinheim, 2006.
- (28) Dmitri Talapin, *Experimental and theoretical studies on the formation of highly luminescent II-VI, III-V and core-shell semiconductor nanocrystals*, 2002.
- (29) Brus, L. *The Journal of Physical Chemistry* **1986**, *90*, 2555–2560.
- (30) Panfil, Y. E.; Shamalia, D.; Cui, J.; Koley, S.; Banin, U. *The Journal of chemical physics* **2019**, *151*, 224501.
- (31) Lohmann, S.-H.; Strelow, C.; Mews, A.; Kipp, T. *ACS nano* **2017**, *11*, 12185–12192.
- (32) Slachmuylders, A. F.; Partoens, B.; Magnus, W.; Peeters, F. M. *Physical Review B* **2006**, *74*, DOI: 10.1103/physrevb.74.235321.
- (33) Glennon, J. J.; Tang, R.; Buhro, W. E.; Loomis, R. A. *Nano letters* **2007**, *7*, 3290–3295.
- (34) *Principles of Fluorescence Spectroscopy*, 3rd ed.; Lakowicz, J., Ed.; Springer, Boston, MA: 2006.

-
- (35) Fox, M., *Optical properties of solids*, Second edition, reprinted (with corrections); Oxford master series in condensed matter physics, Vol. 3; Oxford University Press: Oxford and New York, NY, 2011.
- (36) Achermann, M.; Hollingsworth, J. A.; Klimov, V. I. *Physical Review B* **2003**, *68*, DOI: 10.1103/PhysRevB.68.245302.
- (37) Wang, C.; Wehrenberg, B. L.; Woo, C. Y.; Guyot-Sionnest, P. *The Journal of Physical Chemistry B* **2004**, *108*, 9027–9031.
- (38) Caruge, J.-M.; Chan, Y.; Sundar, V.; Eisler, H. J.; Bawendi, M. G. *Physical Review B* **2004**, *70*, DOI: 10.1103/PhysRevB.70.085316.
- (39) Fisher, B.; Caruge, J.-M.; Chan, Y.-T.; Halpert, J.; Bawendi, M. G. *Chemical Physics* **2005**, *318*, 71–81.
- (40) Bonati, C.; Mohamed, M. B.; Tonti, D.; Zgrablic, G.; Haacke, S.; van Mourik, F.; Chergui, M. *Physical Review B* **2005**, *71*, DOI: 10.1103/PhysRevB.71.205317.
- (41) Troparevsky, M. C.; Franceschetti, A. *Applied Physics Letters* **2005**, *87*, 263115.
- (42) Oron, D.; Kazes, M.; Shweky, I.; Banin, U. *Physical Review B* **2006**, *74*, DOI: 10.1103/PhysRevB.74.115333.
- (43) Franceschetti, A.; Troparevsky *The Journal of Physical Chemistry C* **2007**, *111*, 6154–6157.
- (44) Franceschetti, A.; Zunger, A. *Physical Review B* **2000**, *62*, R16287–R16290.
- (45) Ibuki, H.; Ihara, T.; Kanemitsu, Y. *The Journal of Physical Chemistry C* **2016**, *120*, 23772–23779.
- (46) Vong, A. F.; Irgen-Gioro, S.; Wu, Y.; Weiss, E. A. *Nano letters* **2021**, *21*, 10040–10046.
- (47) Empedocles; Bawendi *Science (New York, N.Y.)* **1997**, *278*, 2114–2117.
- (48) Oda, M.; Hasegawa, A.; Iwami, N.; Nishiura, K.; Ando, N.; Nishiyama, A.; Horiuchi, H.; Tani, T. *Colloids and surfaces. B, Biointerfaces* **2007**, *56*, 241–245.
- (49) Owen, J. *Science (New York, N.Y.)* **2015**, *347*, 615–616.
- (50) Boles, M. A.; Ling, D.; Hyeon, T.; Talapin, D. V. *Nature Materials* **2016**, *15*, 141–153.
- (51) De Roo, J.; Justo, Y.; de Keukeleere, K.; van den Broeck, F.; Martins, J. C.; van Driessche, I.; Hens, Z. *Angewandte Chemie (International ed. in English)* **2015**, *54*, 6488–6491.

- (52) Kalyuzhny, G.; Murray, R. W. *The journal of physical chemistry. B* **2005**, *109*, 7012–7021.
- (53) Jasieniak, J.; Mulvaney, P. *Journal of the American Chemical Society* **2007**, *129*, 2841–2848.
- (54) Ott, F. D.; Spiegel, L. L.; Norris, D. J.; Erwin, S. C. *Physical Review Letters* **2014**, *113*, 156803.
- (55) Schwarz, M.; Mews, A.; Dorn, A. *Nanoscale* **2021**, *13*, 8017–8023.
- (56) Routzahn, A. L.; Jain, P. K. *Nano Letters* **2015**, *15*, 2504–2509.
- (57) Sahu, A.; Kang, M. S.; Kompch, A.; Notthoff, C.; Wills, A. W.; Deng, D.; Winterer, M.; Frisbie, C. D.; Norris, D. J. *Nano Letters* **2012**, *12*, 2587–2594.
- (58) Sercel, P. C.; Shabaev, A.; Efros, A. L. *Nano Letters* **2017**, *17*, 4820–4830.
- (59) Manna, L.; Scher, E. C.; Li, L.-S.; Alivisatos, A. P. *Journal of the American Chemical Society* **2002**, *124*, 7136–7145.
- (60) Jones, M.; Nedeljkovic, J.; Ellingson, R. J.; Nozik, A. J.; Rumbles, G. *The Journal of Physical Chemistry B* **2003**, *107*, 11346–11352.
- (61) Korsunskaya, N. E.; Dybiec, M.; Zhukov, L.; Ostapenko, S.; Zhukov, T. *Semiconductor Science and Technology* **2005**, *20*, 876–881.
- (62) Tice, D. B.; Frederick, M. T.; Chang, R. P. H.; Weiss, E. A. *The Journal of Physical Chemistry C* **2011**, *115*, 3654–3662.
- (63) Asami, H.; Abe, Y.; Ohtsu, T.; Kamiya, I.; Hara, M. *The Journal of Physical Chemistry B* **2003**, *107*, 12566–12568.
- (64) Chen, R. S.; Lu, C. Y.; Chen, K. H.; Chen, L. C. *Applied Physics Letters* **2009**, *95*, 233119.
- (65) Krivenkov, V.; Tretyachenko, A.; Samokhvalov, P. S.; Chistyakov, A. A.; Nabiev, I. In *Nanophotonics VI*, ed. by Andrews, D. L.; Nunzi, J.-M.; Ostendorf, A., SPIE: 2016, p 98843L.
- (66) Uematsu, T.; Kimura, J.; Yamaguchi, Y. *Nanotechnology* **2004**, *15*, 822–827.
- (67) Šimurda, M.; Němec, P.; Trojánek, F.; Malý, P. *Thin Solid Films* **2004**, *453-454*, 300–303.
- (68) Nazzal, A. Y.; Qu, L.; Peng, X.; Xiao, M. *Nano Letters* **2003**, *3*, 819–822.
- (69) Derfus, A. M.; Chan, W. C. W.; Bhatia, S. N. *Nano letters* **2004**, *4*, 11–18.
- (70) Hines, D. A.; Becker, M. A.; Kamat, P. V. *The Journal of Physical Chemistry C* **2012**, *116*, 13452–13457.

-
- (71) Pechstedt, K.; Whittle, T.; Baumberg, J.; Melvin, T. *The Journal of Physical Chemistry C* **2010**, *114*, 12069–12077.
- (72) Wen, X.; Sitt, A.; Yu, P.; Ko, H.-c.; Toh, Y.-R.; Tang, J. *Journal of Nanoparticle Research* **2012**, *14*, 1–13.
- (73) Emara, M. M.; van Patten, P. G. *Materials Chemistry and Physics* **2020**, *256*, 123652.
- (74) van Sark, W. G. J. H. M.; Frederix, P. L. T. M.; van den Heuvel, D. J.; Gerritsen, H. C.; Bol, A. A.; van Lingen, J. N. J.; de Mello Donegá, C.; Meijerink, A. *The Journal of Physical Chemistry B* **2001**, *105*, 8281–8284.
- (75) van Sark, W. G. J. H. M.; Frederix, P. L. T. M.; Bol, A. A.; Gerritsen, H. C.; Meijerink, A. *ChemPhysChem* **2002**, *3*, 871–879.
- (76) Wang, X.; Zhang, J.; Nazzal, A.; Xiao, M. *Applied Physics Letters* **2003**, *83*, 162–164.
- (77) Zhang, Y.; He, J.; Wang, P.-N.; Chen, J.-Y.; Lu, Z.-J.; Lu, D.-R.; Guo, J.; Wang, C.-C.; Yang, W.-L. *Journal of the American Chemical Society* **2006**, *128*, 13396–13401.
- (78) Manner, V. W.; Kuposov, A. Y.; Szymanski, P.; Klimov, V. I.; Sykora, M. *ACS nano* **2012**, *6*, 2371–2377.
- (79) Samia, A. C. S.; Chen, X.; Burda, C. *Journal of the American Chemical Society* **2003**, *125*, 15736–15737.
- (80) J. E. Bowen Katari/V. L. Colvin/A. P. Alivisatos.
- (81) Sohel, M. A.; Pan, L.; Tamargo, M. C. *physica status solidi c* **2012**, *9*, 1776–1778.
- (82) Wang, Y.; Tang, Z.; Correa-Duarte, M. A.; Pastoriza-Santos, I.; Giersig, M.; Kotov, N. A.; Liz-Marzán, L. M. *The Journal of Physical Chemistry B* **2004**, *108*, 15461–15469.
- (83) Sato, K.; Kojima, S.; Hattori, S.; Chiba, T.; Ueda-Sarson, K.; Torimoto, T.; Tachibana, Y.; Kuwabata, S. *Nanotechnology* **2007**, *18*, 465702.
- (84) Myung, N.; Bae, Y.; Bard, A. J. *Nano Letters* **2003**, *3*, 747–749.
- (85) Cooper, D. R.; Suffern, D.; Carlini, L.; Clarke, S. J.; Parbhoo, R.; Bradforth, S. E.; Nadeau, J. L. *Physical chemistry chemical physics : PCCP* **2009**, *11*, 4298–4310.
- (86) Maenosono, S.; Ozaki, E.; Yoshie, K.; Yamaguchi, Y. *Japanese Journal of Applied Physics* **2001**, *40*, L638.
- (87) Kimura, J.; Maenosono, S.; Yamaguchi, Y. *Nanotechnology* **2003**, *14*, 69–72.

- (88) Javier, A.; Strouse, G. F. *Chemical Physics Letters* **2004**, *391*, 60–63.
- (89) Uematsu, T.; Maenosono, S.; Yamaguchi, Y. *Applied Physics Letters* **2006**, *89*, 031910.
- (90) Lau, P. C.; Norwood, R. A.; Mansuripur, M.; Peyghambarian, N. *Nanotechnology* **2013**, *24*, 015501.
- (91) Lorenzon, M.; Christodoulou, S.; Vaccaro, G.; Pedrini, J.; Meinardi, F.; Moreels, I.; Brovelli, S. *Nature communications* **2015**, *6*, 6434.
- (92) Toporski, J.; Dieing, T.; Hollricher, O., *Confocal Raman Microscopy*, 2. 2nd ed. 2018; Springer Series in Surface Sciences, Vol. 66; Springer International Publishing: Cham, 2018.
- (93) Empedocles, S. A.; Neuhauser, R.; Shimizu, K.; Bawendi, M. G. *Advanced Materials* **1999**, *11*, 1243–1256.
- (94) Kelley, A. M. *The Journal of chemical physics* **2019**, *151*, 140901.
- (95) Gross, R., *Festkörperphysik: Aufgaben und Lösungen*, 2nd ed.; De Gruyter Studium Ser; Walter de Gruyter GmbH: Berlin/Boston, 2018.
- (96) Comas, F.; Studart, N.; Marques, G. E. *Solid State Communications* **2004**, *130*, 477–480.
- (97) Lange, H.; Machón, M.; Artemyev, M.; Woggon, U.; Thomsen, C. *physica status solidi (RRL) – Rapid Research Letters* **2007**, *1*, 274–276.
- (98) Wu, Y.; Jin, S.; Ye, Y.; Wang, S.; Feng, Z.; Li, C. *The Journal of Physical Chemistry C* **2014**, *118*, 30269–30273.
- (99) Lin, C.; Kelley, D. F.; Rico, M.; Kelley, A. M. *ACS nano* **2014**, *8*, 3928–3938.
- (100) Dzhagan, V. M.; Valakh, M. Y.; Himcinschi, C.; Milekhin, A. G.; Solonenko, D.; Yeryukov, N. A.; Raevskaya, O. E.; Stroyuk, O. L.; Zahn, D. R. T. *The Journal of Physical Chemistry C* **2014**, *118*, 19492–19497.
- (101) Dzhagan, V.; Valakh, M. Y.; Kolny-Olesiak, J.; Lokteva, I.; Zahn, D. R. T. *Applied Physics Letters* **2009**, *94*, 243101.
- (102) Dzhagan, V. M.; Azhniuk, Y. M.; Milekhin, A. G.; Zahn, D. R. T. *Journal of Applied Physics D: Applied Physics* **2018**, *51*, 503001.
- (103) Rolo, A. G.; Vasilevskiy, M. I. *Journal of Raman Spectroscopy* **2007**, *38*, 618–633.
- (104) Dzhagan, V. M.; Lokteva, I.; Himcinschi, C.; Kolny-Olesiak, J.; Valakh, M. Y.; Schulze, S.; Zahn, D. R. T. *Journal of Applied Physics* **2011**, *109*, 084334.

-
- (105) Zhang, B.; Chang, R.; Wang, K.; Lü, J.-T.; Wang, S. *The journal of physical chemistry letters* **2018**, *9*, 5055–5062.
- (106) Nobile, C.; Kudera, S.; Fiore, A.; Carbone, L.; Chilla, G.; Kipp, T.; Heitmann, D.; Cingolani, R.; Manna, L.; Krahn, R. *physica status solidi (a)* **2007**, *204*, 483–486.
- (107) Adu, K. W.; Xiong, Q.; Gutierrez, H. R.; Chen, G.; Eklund, P. C. *Applied Physics A* **2006**, *85*, 287–297.
- (108) Liu, H. F.; Tripathy, S.; Hu, G. X.; Gong, H. *Journal of Applied Physics* **2009**, *105*, 053507.
- (109) Olson, E. A.; Efremov, M. Y.; Zhang, M.; Zhang, Z.; Allen, L. H. *Journal of Applied Physics* **2005**, *97*, DOI: 10.1063/1.1832741.
- (110) Wang, Z.; Li, Z.; Kornowski, A.; Ma, X.; Myalitsin, A.; Mews, A. *Small (Weinheim an der Bergstrasse, Germany)* **2011**, *7*, 2464–2468.
- (111) Wang, F.; Buhro, W. E. *Nano Letters* **2016**, *16*, 889–894.
- (112) Wang, F.; Buhro, W. E. *ACS nano* **2017**, *11*, 12526–12535.
- (113) Wang, F.; Buhro, W. E. *Chemistry of Materials* **2018**, *30*, 1316–1323.
- (114) Li, Z.; Kurtulus, A.; Fu, N.; Wang, Z.; Kornowski, A.; Pietsch, U.; Mews, A. *Advanced Functional Materials* **2009**, *19*, 3650–3661.
- (115) Wang, F.; Buhro, W. E. *Small* **2010**, *6*, 573–581.
- (116) Myalitsin, A.; Strelow, C.; Wang, Z.; Li, Z.; Kipp, T.; Mews, A. *ACS nano* **2011**, *5*, 7920–7927.
- (117) Giblin, J.; Vietmeyer, F.; McDonald, M. P.; Kuno, M. *Nano Letters* **2011**, *11*, 3307–3311.
- (118) Protasenko, V. V.; Hull, K. L.; Kuno, M. *Advanced Materials* **2005**, *17*, 2942–2949.
- (119) Franz, D.; Reich, A.; Strelow, C.; Wang, Z.; Kornowski, A.; Kipp, T.; Mews, A. *Nano letters* **2014**, *14*, 6655–6659.
- (120) Glennon, J. J.; Buhro, W. E.; Loomis, R. A. *The Journal of Physical Chemistry C* **2008**, *112*, 4813–4817.
- (121) Wayman, V. L.; Morrison, P. J.; Wang, F.; Tang, R.; Buhro, W. E.; Loomis, R. A. *The journal of physical chemistry letters* **2012**, *3*, 2627–2632.
- (122) Achtstein, A. W.; Schliwa, A.; Prudnikau, A.; Hardzei, M.; Artemyev, M. V.; Thomsen, C.; Woggon, U. *Nano Letters* **2012**, *12*, 3151–3157.

- (123) Protasenko, V.; Gordeyev, S.; Kuno, M. *Journal of the American Chemical Society* **2007**, *129*, 13160–13171.
- (124) Schäfer, S.; Wang, Z.; Zierold, R.; Kipp, T.; Mews, A. *Nano Letters* **2011**, *11*, 2672–2677.
- (125) Schäfer, S.; Reich, A.; Wang, Z.; Kipp, T.; Mews, A. *Applied Physics Letters* **2012**, *100*, DOI: 10.1063/1.3676278.
- (126) Schäfer, S.; Wang, Z.; Kipp, T.; Mews, A. *Physical review letters* **2011**, *107*, 137403.
- (127) Qu, L.; Peng, X. *Journal of the American Chemical Society* **2002**, *124*, 2049–2055.
- (128) Liu, Y.-H.; Wang, F.; Hoy, J.; Wayman, V. L.; Steinberg, L. K.; Loomis, R. A.; Buhro, W. E. *Journal of the American Chemical Society* **2012**, *134*, 18797–18803.
- (129) Goebel, J. A.; Black, R. W.; Puthussery, J.; Giblin, J.; Kosel, T. H.; Kuno, M. *Journal of the American Chemical Society* **2008**, *130*, 14822–14833.
- (130) Li, Z.; Ma, X.; Sun, Q.; Wang, Z.; Liu, J.; Zhu, Z.; Qiao, S. Z.; Smith, S. C.; Lu, G.; Mews, A. *European Journal of Inorganic Chemistry* **2010**, *2010*, 4325–4331.
- (131) Liu, S.; Zhang, W.-H.; Li, C. *Journal of Crystal Growth* **2011**, *336*, 94–100.
- (132) Jiang, F.; Liu, J.; Li, Y.; Fan, L.; Ding, Y.; Li, Y. *Advanced Functional Materials* **2012**, *22*, 2402–2411.
- (133) Kortan, A. R.; Hull, R.; Opila, R. L.; Bawendi, M. G.; Steigerwald, M. L.; Carroll, P. J.; Brus, L. E. *Journal of the American Chemical Society* **1990**, *112*, 1327–1332.
- (134) Eychmüller, A.; Mews, A.; Weller, H. *Chemical Physics Letters* **1993**, *208*, 59–62.
- (135) Hines, M. A.; Guyot-Sionnest, P. *The Journal of Physical Chemistry* **1996**, *100*, 468–471.
- (136) Peng, X.; Schlamp, M. C.; Kadavanich, A. V.; Alivisatos, A. P. *Journal of the American Chemical Society* **1997**, *119*, 7019–7029.
- (137) Kim, S.; Fisher, B.; Eisler, H.-J.; Bawendi, M. *Journal of the American Chemical Society* **2003**, *125*, 11466–11467.
- (138) Sitt, A.; Della Sala, F.; Menagen, G.; Banin, U. *Nano Letters* **2009**, *9*, 3470–3476.
- (139) Dong, L.; Sugunan, A.; Hu, J.; Zhou, S.; Li, S.; Popov, S.; Toprak, M. S.; Friberg, A. T.; Muhammed, M. *Applied Optics* **2013**, *52*, 105–109.
- (140) Kong, D.; Jia, Y.; Ren, Y.; Xie, Z.; Wu, K.; Lian, T. *The Journal of Physical Chemistry C* **2018**, *122*, 14091–14098.

- (141) Hoffman, M. P.; Lee, A. Y.; Nagelj, N.; Lee, Y. V.; Olshansky, J. H. *RSC advances* **2021**, *11*, 35887–35892.
- (142) Bae, W. K.; Padilha, L. A.; Park, Y.-S.; McDaniel, H.; Robel, I.; Pietryga, J. M.; Klimov, V. I. *ACS nano* **2013**, *7*, 3411–3419.
- (143) Chen, Y.; Vela, J.; Htoon, H.; Casson, J. L.; Werder, D. J.; Bussian, D. A.; Klimov, V. I.; Hollingsworth, J. A. *Journal of the American Chemical Society* **2008**, *130*, 5026–5027.
- (144) Basché, T.; Moerner, W. E.; Orrit, M.; Talon, H. *Physical review letters* **1992**, *69*, 1516.
- (145) Efros, A. L.; Nesbitt, D. J. *Nature nanotechnology* **2016**, *11*, 661–671.
- (146) Galland, C.; Ghosh, Y.; Steinbrück, A.; Sykora, M.; Hollingsworth, J. A.; Klimov, V. I.; Htoon, H. *Nature* **2011**, *479*, 203–207.
- (147) Kim, T.; Jung, S. I.; Ham, S.; Chung, H.; Kim, D. *Small (Weinheim an der Bergstrasse, Germany)* **2019**, *15*, e1900355.
- (148) Yuan, G.; Gómez, D. E.; Kirkwood, N.; Boldt, K.; Mulvaney, P. *ACS nano* **2018**, *12*, 3397–3405.
- (149) Spinicelli, P.; Buil, S.; Quélin, X.; Mahler, B.; Dubertret, B.; Hermier, J.-P. *Physical review letters* **2009**, *102*, 136801.
- (150) Kuno, M.; Fromm, D. P.; Hamann, H. F.; Gallagher, A.; Nesbitt, D. J. *The Journal of chemical physics* **2001**, *115*, 1028–1040.
- (151) Yuan, G.; Gómez, D. E.; Kirkwood, N.; Boldt, K.; Mulvaney, P. *ACS nano* **2018**, *12*, 3397–3405.
- (152) Kuno, M.; Fromm, D. P.; Hamann, H. F.; Gallagher, A.; Nesbitt, D. J. *The Journal of chemical physics* **2000**, *112*, 3117–3120.
- (153) Frantsuzov, P.; Kuno, M.; Jankó, B.; Marcus, R. A. *Nature Physics* **2008**, *4*, 519–522.
- (154) Verberk, R.; van Oijen, A. M.; Orrit, M. *Physical Review B* **2002**, *66*, DOI: 10.1103/PhysRevB.66.233202.
- (155) Shimizu, K. T.; Neuhauser, R. G.; Leatherdale, C. A.; Empedocles, S. A.; Woo, W. K.; Bawendi, M. G. *Physical Review B* **2001**, *63*, DOI: 10.1103/PhysRevB.63.205316.
- (156) Frantsuzov, P. A.; Marcus, R. A. *Physical Review B* **2005**, *72*, DOI: 10.1103/PhysRevB.72.155321.

- (157) Houel, J.; Doan, Q. T.; Cajgfinger, T.; Ledoux, G.; Amans, D.; Aubret, A.; Dominjon, A.; Ferriol, S.; Barbier, R.; Nasilowski, M.; Lhuillier, E.; Dubertret, B.; Dujardin, C.; Kulzer, F. *ACS nano* **2015**, *9*, 886–893.
- (158) Manceau, M.; Vezzoli, S.; Glorieux, Q.; Giacobino, E.; Carbone, L.; de Vittorio, M.; Hermier, J.-P.; Bramati, A. *Chemphyschem : a European journal of chemical physics and physical chemistry* **2018**, DOI: 10.1002/cphc.201800694.
- (159) Verdaasdonk, J. S.; Stephens, A. D.; Haase, J.; Bloom, K. *Journal of cellular physiology* **2014**, *229*, 132–138.
- (160) Engelhardt, J.; Knebel, W. *Physik in unserer Zeit* **1993**, *24*, 70–78.
- (161) Iffländer, R., *Solid-state lasers for materials processing: Fundamental relations and technical realizations ; with 73 tables and numerous examples*; Physics and astronomy online library, Vol. 77; Springer: Berlin and Heidelberg, 2001.
- (162) Achtstein, A. W.; Hennig, J.; Prudnikau, A.; Artemyev, M. V.; Woggon, U. *The Journal of Physical Chemistry C* **2013**, *117*, 25756–25760.
- (163) Egerton, R. F. and others, *Physical principles of electron microscopy*, 2nd ed.; Springer: New York, 2005; Vol. 56.
- (164) Houtepen, A. J.; Hens, Z.; Owen, J. S.; Infante, I. *Chemistry of Materials* **2017**, *29*, 752–761.
- (165) Margoshes, M.; Fassel, V. A. *Spectrochimica Acta* **1955**, *7*, 14–24.
- (166) Kusterer, R.; Ruhmlieb, C.; Strelow, C.; Kipp, T.; Mews, A. *The Journal of Physical Chemistry C* **2022**, *126*, 19240–19249.
- (167) Von Holt, B.; Kudera, S.; Weiss, A.; Schrader, T. E.; Manna, L.; Parak, W. J.; Braun, M. *Journal of Materials Chemistry* **2008**, *18*, 2728.
- (168) Shakeri, B.; Meulenberg, R. W. *Langmuir : the ACS journal of surfaces and colloids* **2015**, *31*, 13433–13440.
- (169) Son, J. G.; Choi, E.; Piao, Y.; Han, S. W.; Lee, T. G. *Nanoscale* **2016**, *8*, 4573–4578.
- (170) Alexandratos, S. D.; Zhu, X.; Marianski, M. R. *Solvent Extraction and Ion Exchange* **2021**, *39*, 152–165.
- (171) Raman, A.; Quiñones, R.; Barriger, L.; Eastman, R.; Parsi, A.; Gawalt, E. S. *Langmuir : the ACS journal of surfaces and colloids* **2010**, *26*, 1747–1754.
- (172) Morris-Cohen, A. J.; Donakowski, M. D.; Knowles, K. E.; Weiss, E. A. *The Journal of Physical Chemistry C* **2010**, *114*, 897–906.

-
- (173) Kendix, E. L.; Prati, S.; Joseph, E.; Sciutto, G.; Mazzeo, R. *Analytical and Bio-analytical Chemistry* **2009**, *394*, 1023–1032.
- (174) Jiang; Krauss, T. D.; Brus, L. E. *The Journal of Physical Chemistry B* **2000**, *104*, 11936–11941.
- (175) Panfil, Y. E.; Cui, J.; Koley, S.; Banin, U. *ACS nano* **2022**, *16*, 5566–5576.
- (176) Yoffe, A. D. *Advances in Physics* **1993**, *42*, 173–262.
- (177) Vietmeyer, F.; Frantsuzov, P. A.; Janko, B.; Kuno, M. *Physical Review B* **2011**, *83*, DOI: 10.1103/physrevb.83.115319.
- (178) Harder, P.; Nielsen, A.; Sassnau, A.-K.; Bonatz, D.; Perbandt, M.; Kipp, T.; Mews, A. *Chemistry of Materials* **2021**, *33*, 1061–1069.
- (179) Cordero, S. R.; Carson, P. J.; Estabrook, R. A.; Strouse, G. F.; Buratto, S. K. *The Journal of Physical Chemistry B* **2000**, *104*, 12137–12142.
- (180) Emara, M. M.; van Patten, P. G. *Materials Chemistry and Physics* **2020**, *256*, 123652.
- (181) Matylitsky, V. V.; Shavel, A.; Gaponik, N.; Eychmüller, A.; Wachtveitl, J. *The Journal of Physical Chemistry C* **2008**, *112*, 2703–2710.
- (182) Scholz, F.; Dworak, L.; Matylitsky, V. V.; Wachtveitl, J. *ChemPhysChem* **2011**, *12*, 2255–2259.
- (183) Peterson, M. D.; Jensen, S. C.; Weinberg, D. J.; Weiss, E. A. *ACS nano* **2014**, *8*, 2826–2837.
- (184) Hu, L.; Zhu, H.; Chen, G.; Ma, C. *Journal of Luminescence* **2023**, *255*, 119551.
- (185) Anderson, N. C.; Hendricks, M. P.; Choi, J. J.; Owen, J. S. *Journal of the American Chemical Society* **2013**, *135*, 18536–18548.
- (186) García-Santamaría, F.; Chen, Y.; Vela, J.; Schaller, R. D.; Hollingsworth, J. A.; Klimov, V. I. *Nano letters* **2009**, *9*, 3482–3488.
- (187) Chen, O.; Zhao, J.; Chauhan, V. P.; Cui, J.; Wong, C.; Harris, D. K.; Wei, H.; Han, H.-S.; Fukumura, D.; Jain, R. K.; Bawendi, M. G. *Nature materials* **2013**, *12*, 445–451.
- (188) Rabouw, F. T.; Lunnemann, P.; van Dijk-Moes, R. J. A.; Frimmer, M.; Pietra, F.; Koenderink, A. F.; Vanmaekelbergh, D. *Nano letters* **2013**, *13*, 4884–4892.
- (189) Liu, G.; Liang, W.; Xue, X.; Rosei, F.; Wang, Y. *Advanced science (Weinheim, Baden-Wuerttemberg, Germany)* **2021**, *8*, e2102784.

- (190) Gómez, D. E.; van Embden, J.; Mulvaney, P.; Fernée, M. J.; Rubinsztein-Dunlop, H. *ACS nano* **2009**, *3*, 2281–2287.
- (191) Ihara, T.; Kanemitsu, Y. *Physical Review B* **2014**, *90*, DOI: 10.1103/PhysRevB.90.195302.
- (192) Hou, X.; Kang, J.; Qin, H.; Chen, X.; Ma, J.; Zhou, J.; Chen, L.; Wang, L.; Wang, L.-W.; Peng, X. *Nature communications* **2019**, *10*, 1750.
- (193) Frantsuzov, P.; Kuno, M.; Jankó, B.; Marcus, R. A. *Nature Physics* **2008**, *4*, 519–522.
- (194) Kuno, M.; Fromm, D. P.; Johnson, S. T.; Gallagher, A.; Nesbitt, D. J. *Physical Review B* **2003**, *67*, DOI: 10.1103/physrevb.67.125304.
- (195) Material database <https://gestis.dguv.de/>, 10.12.2023.
- (196) Supplier <https://www.sigmaaldrich.com/DE/de.>, 10.12.2023.

8 Appendix

8.1 Supporting Information

Figure 8.1(a) shows the PL spectra of CdSe QWs at different stages of the purification process. Without any purification, the spectrum is broad and the maximum of the PL intensity lies at 650 nm. Already after the first cycle of precipitation and re-dispersion, the spectrum has the shape that does not change with further (at least up to seven) cycles of purification. Figure 8.1(b) shows results of measurements in which the CdSe QWs that were purified with different numbers of steps are each illuminated continuously in an oxygen atmosphere. The observed increase of the PL intensity is not noticeably dependent on the degree of purification.

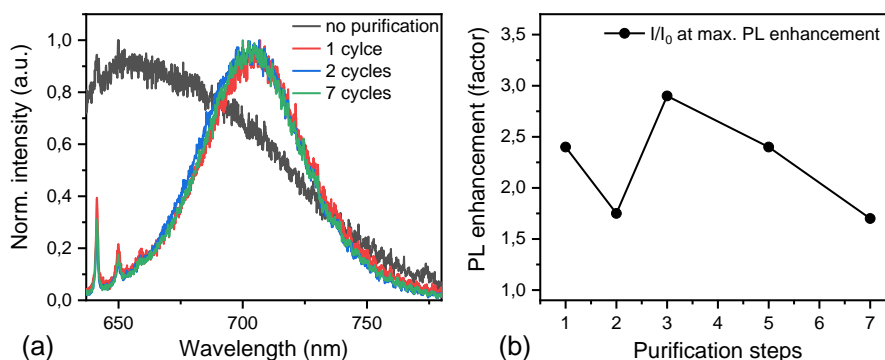


Figure 8.1: Effect of purification on PL properties of CdSe QWs. (a) PL spectra of CdSe QWs without and with up to seven cycles of purification. (b) PL enhancement of the CdSe QWs at different degrees of purification. The PL enhancement experiments were conducted in an oxygen atmosphere with $P = 0.2\text{--}0.4 \text{ kW/cm}^2$, $\lambda = 633 \text{ nm}$, cw.

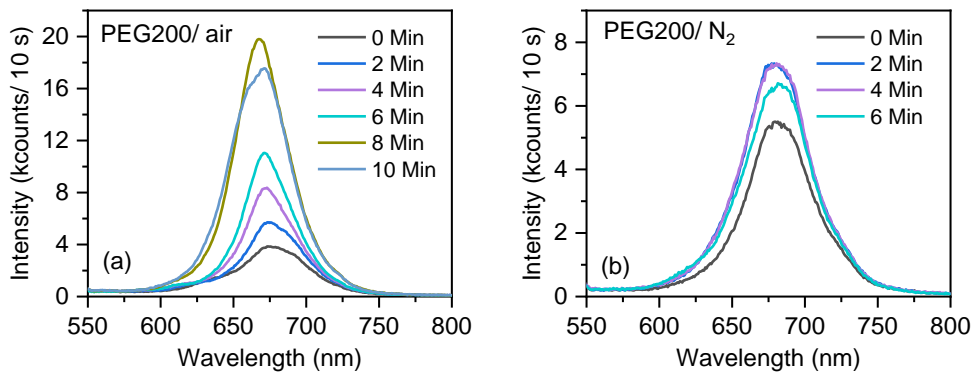


Figure 8.2: Evolution of spectra of CdSe QWs covered with PEG200. (a) Evolution in untreated PEG200. (b) Evolution in PEG200 degassed with N₂. $P = 0.2 \text{ kW/cm}^2$, $\lambda = 470 \text{ nm}$, cw. These data were obtained in preceding studies.

Figure 8.2 shows two measurements of CdSe QWs that are covered with PEG200. The data shown in Figure 8.2(a) was obtained with untreated PEG200, while the data shown in Figure 8.2(b) was obtained with PEG200 that was degassed by injection of nitrogen prior to the measurement. While the CdSe QWs examined in PEG200/air show extensive photobrightening, only small changes are observed for the spectra of the CdSe QWs examined in PEG200/N₂.

8.2 Hazard Information

The safety and disposal instructions for the chemicals used in this work are listed in Table 8.1.

Table 8.1: Safety and disposal instructions for the chemicals used.^{195,196}










Substance	GHS symbol	H-phrases	P-phrases	Disposal
Argon		280	403	–
Acetone		225, 319, 336	210, 233, 240, 241, 242, 305+351+338	(1)
Bismut		228	210, 370+378	(2)
Cadmium acetate		302, 312, 332, 350, 400, 410	201, 261, 280, 302+352, 304+340, 312	(2)
Cadmium selenide		301+331, 312, 350, 373, 410	201, 261, 273, 301+310+330, 308+313, 403+223	(2)
Cadmium sulfide		302, 341, 350, 361, 372, 410	201, 273, 301+310+330, 308+313, 501	(2)
Di- <i>n</i> -octylphosphinic acid		319	305+351+338	(1)
Hexane		225, 304, 315, 336, 361f, 373, 411	201, 273, 301+330+331, 302+352, 308+313	(3)
Hydrochloric acid		290, 314, 334	280, 303+361+353, 305+351+353	(4)

Table 8.1: Safety and disposal instructions for the chemicals used.^{195,196}
























Substance	GHS symbol	H-phrases	P-phrases	Disposal
Isopropanol	 	225, 319, 336	210, 240, 305+351+338, 403+233	(1)
Methylviologen dichloride hydrate	  	301, 310+330, 315, 319, 335, 372, 410	262, 273, 280, 302+353+310, 304+340+310, 314	(2)
Nitric acid	  	272, 290, 330, 314	210, 220, 280, 303+361+353, 304+340+310, 305+351+338	(4)
Nitrogen		280	403	–
Octadecene		304, 413	273, 301+310, 331	(3)
Oxygen	 	270, 280	220, 244, 370+376, 403	–
PDMS	Not a dangerous substance according to GHS			(2)
<i>n</i> -Propylamine	  	225, 290, 302, 311, 331, 314	201, 280, 305+351+338, 310, 301+330+331, 303+361+353	(3)
Selen	 	301, 331, 373, 413	260, 264, 273, 301+310, 304+340+311	(2)
Silver nitrate	  	272, 290, 314, 410	210, 260, 273, 280, 303+361+353, 305+351+338, 308+310	(2)

Table 8.1: Safety and disposal instructions for the chemicals used.^{195,196}

Substance	GHS symbol	H-phrases	P-phrases	Disposal
Toluene		225, 304, 315, 336, 361d, 373	210, 240, 301+310+330, 302+352, 314, 403+233	(3)
Tri- <i>n</i> - octylphosphine		314	280, 305+351+338	(1)
Tri- <i>n</i> - octylphosphine oxide		319, 411	262, 273, 305+351+338	(2)

Disposal instructions:

- (1) If necessary, dissolve in suitable solvent and discard into container for halogen-free organic solvents.
- (2) Discard into container for contaminated solid waste.
- (3) If necessary, dissolve in suitable solvent and discard into container for halogenated and/or toxic organic solvents.
- (4) Dilute and discard in container for inorganic acids.

8.3 Publications

Article

Kusterer, R.; Ruhmlieb, C.; Strelow, C.; Kipp, T.; Mews, A. *The Journal of Physical Chemistry C* **2022**, 126, 19240–19249.

Conference Contributions

- 07/2022 Gordon Resaearch Conference, Les Diablerets Switzerland.
Poster: Reversible and Irreversible Effects of Oxygen on the Photoluminescence of CdSe Quantum Wires
- 02/2020 WE-Heraeus-Seminar, Bad Honnef Germany.
Poster: Real-Time Monitoring of Photoinduced Processes on Semiconducting Nanowires in Various Chemical Environments
- 09/2019 NaNaX 9, Hamburg Germany.
Poster: Fluorescence Spectroscopy of CdSe Nanowires in Flow Channels
- 07/2019 DPG Physics School, Bad Honnef Germany.
Poster: Photoinduced Modifications of CdSe Nanowires in Flow Channels
- 05/2019 Bunsentagung, Jena Germany.
Poster: Photoinduced Modifications of CdSe Nanowires in Flow Channels

8.4 Acknowledgments

At this point I want to thank the people without whom this work would not have been possible. My thanks go to

- Prof. Dr. Alf Mews for guiding me through this thesis, giving me the freedom to develop myself, and of course for the assessment of this dissertation.
- Prof. Dr. Gabriel Bester for providing the second assessment for this dissertation.
- Prof. Dr. Dorota Koziej and PD Dr. Tobias Vossmeier for joining the disputation of this thesis as part of the examination board.
- PD Dr. Tobias Kipp for the discussions and lectures on science and so many other things. Also for editing the monthly reports and most importantly the essential support in writing and editing publications.
- Dr. Christian Strelow for providing constant support in performing spectroscopic experiments, great ideas and especially for editing this thesis.
- Dipl.-Ing. Jan Flügge for the constant technical support in the spectroscopy labs as well as for answering all my IT questions.
- Dr. Charlotte Ruhmlieb for performing SEM measurements and for the assistance in writing publications and monthlies, for inspiring me with new ideas and working together to finally describe the photobrightening effect of nanowires.
- Uta Sazama for performing the TGA-IR measurements.
- Jili Han for performing the ICP-MS measurements.
- Dr. Jannik Rebmann for the support with the IR measurements.
- Stefan Werner and Dr. Thomas Tsangas for the TEM measurements.
- Dr. Sonja Zeller for providing the QDs.
- Florian Johst for the support with the Comsol simulations.
- Dr. Maria Taplick for lending us the plasma chamber to grill the samples.
- Sebastian Hentschel for the support with the TGA measurements.
- Martina Krasa for the support with the administration.
- Hans Werners for taking over half of the physics seminar for the MLS kids.

- Florian Johst, Julian Schattschneider, Theresa Hettinger and Moritz Wehrmeister for contributing essentially to this work as part of their lab courses and theses.
- my office roommates Marcel Dohrmann, Sara Grunewald and Cora Frost for the dart breaks and the in-between Schnack.
- Dr. Marina Mutas and Dr. Philip Harder for introducing me to the Mews group and the world of nanoscience. In addition, Dr. Svenja Patjens for helping me gaining a foothold in spectroscopy.
- my grand editorial team for this thesis: Christian, Jannik, Thomas, Hans, Vincent, Basti, Natalie, Mama, Papa, Paula and Caro.
- the whole Mews group for the unforgettable time, the school trips, the mensa trains and much more.

Finally, my very personal thanks go to my friends and family and especially Caro for the companionship and the mental support throughout the years. You helped me keeping my spirits up at all times!

8.5 Eidesstattliche Erklärung

Hiermit versichere ich an Eides statt, die vorliegende Dissertationsschrift selbst verfasst und keine anderen als die angegebenen Quellen und Hilfsmittel benutzt zu haben. Sofern im Zuge der Erstellung der vorliegenden Dissertationsschrift generative Künstliche Intelligenz (gKI) basierte elektronische Hilfsmittel verwendet wurden, versichere ich, dass meine eigene Leistung im Vordergrund stand und dass eine vollständige Dokumentation aller verwendeten Hilfsmittel gemäß der Guten wissenschaftlichen Praxis vorliegt. Ich trage die Verantwortung für eventuell durch die gKI generierte fehlerhafte oder verzerrte Inhalte, fehlerhafte Referenzen, Verstöße gegen das Datenschutz- und Urheberrecht oder Plagiate.

Hamburg, 12.05.2024

Ort, Datum

R. Kusterer

Roman Kusterer